CaP COATING OF POROUS SINTERED Ti6Al4V POWDER COMPACTS USING BIOMIMETIC AND SOL-GEL METHODS

A Thesis submitted to
the Graduate School of Engineering and Science of
Izmir Institute of Technology
in Partial Fulfillment of the Requirements for the Degree of

MASTER OF SCIENCE

in Materials Science and Engineering

By
Mustafa ALTINDİŞ

August 2006

İzmir, Turkey

We approve the thesis of **Mustafa ALTINDİŞ**

Date of signature

..... **17.08.2006**
Assoc.Prof.Dr. Mustafa GÜDEN
Supervisor
Department of Mechanical Engineering
Izmir Institute of Technology

..... **17.08.2006**
Prof.Dr. Orhan ÖZTÜRK
Department or Physics
Izmir Institute of Technology

..... **17.08.2006**
Assoc.Prof.Dr. Selahattin YILMAZ
Departmant of Chemical Engineering
Izmir Institute of Technology

..... **17.08.2006**
Assoc.Prof.Dr. Sedat AKKURT
Department of Mechanical Engineering
Izmir Institute of Technology

..... **17.08.2006**
Assoc.Prof.Dr. Funda TIHMINLIOĞLU
Departmant of Chemical Engineering
Izmir Institute of Technology

..... **17.08.2006**
Prof Dr. Muhsin ÇİFTÇİOĞLU
Head of Department
Izmir Institute of Technology

……
Assoc. Prof. Dr. Semahat Özdemir
Head of the Graduate School

ACKNOWLEDGEMENTS

First and foremost I would like to thank my advisor Assoc. Prof. Dr. Mustafa Güden for giving me the opportunity to work on what I have found to be an interesting and challenging project. His guidance, knowledge, and stimulation of critical thinking and independent ideas have contributed to my success and development. I would also like to thank my co-advisor Prof. Dr. Muhsin Çiftçioğlu, for his valuable time, help and guidance throughout this project.

I am very greatful to specialist Rukiye Çiftçioğlu and Selçuk Özcan for their instructions, valuable suggestions, and enthusiastic helping. I would also thank to İYTE-MAM staff for their helps.

A special thanks also goes to my family for their endless support during my thesis and all my life.

This list would not be complete without showing my appreciation to Alpay Hızal, Özlem Çağlar Duvarcı, Ali Emrah Çetin for putting up with me in the lab and for making my stay there an enjoyable one.

ABSTRACT

CaP COATING OF POROUS SINTERED Ti6Al4V POWDER COMPACTS USING BIOMIMETIC AND SOL-GEL METHODS

In this study, two methods of CaP coating, dip coating and biomimetic, on porous Ti6Al4V powder compacts to be used in novel spinal cages were experimentally investigated. The powder compacts produced by sintering of compacted green powders contained 37% open porosity with an average pore size of 63 micrometers. Dip-coating solutions were prepared using sol-derived and commercially available HA powders. Biomimetic CaP coatings were performed in 1(at 37°C, Ph = 7.4) °, 5 (at 37°C, pH = 6.0) and 10x (at room temperature, pH = 5.8) simulated body fluid (SBF).

The porous Ti6Al4V powder compacts were successfully coated using HA dip coating solutions. The optimum soaking times were 3 and 1-minute for sol-derived and milled and unmilled comercial HA powders, respectively. Increasing soaking times further started to fill the originally open pores. The thicker deposit and cracks were observed at the sintering necks of the particles was believed to be due to capillary effects drawing the coating solution into this concave region. Milling of HA powder induced more homogenous coating layer on the Ti6Al4V particles.

Increasing Ca and P concentrations in SBF increased the rate of CaP nucleation. Alkaline (NaOH) and heat-treatment (600^{o}C for 1 hour) further accelerated CaP formation. The complete coating of treated and untreated compacts was 14 and 21 days using 1xSBF, 24 and 36 hours using 5xSBF and 4 and 6 hours using 10xSBF, respectively. When considered crack free and homegenous coating layer, dip coating using milled commercial HA powder was found to be the most appropriate method for the coating present powder compacts.

ÖZET

SİNTERLENMİŞ GÖZENEKLİ Ti6Al4V TABLETLERİN SOL-JEL VE BİYOMİMETİK METODLARIYLA CaP KAPLANMASI

Bu çalışmada, spinal kafes olarak kullanılmak üzere gözenekli Ti6Al4V toz tabletlerin, daldırma ve biyomimetik kaplama yöntemleri kullanılarak CaP ile kaplanması incelenmiştir. Toz tabletler işlenmemiş tozun basıldıktan sonra sinterlenmesiyle elde edilmişlerdir; %37 açık gözenekliliğe sahip olup, tabletlerin ortalama gözenek boyutu 63 mikrometredir. Daldırma kaplama solüsyonları kimyasal yolla sentezlenen ve endüstriyel HA tozu kullanılarak hazırlanmıştır. Biyomimetik CaP kaplama için değişik konsantrasyonlarda (1, 5, 10xYVS) yapay vücut sıvısı hazırlanmıştır

Tüm daldırma kaplama solüsyonlarıyla gözenekli Ti6Al4V toz tabletler başarıyla kaplanmıştır. Öğütülmüş ve öğütülmemiş endüstriyel HA tozundan elde edilen daldırma kaplama solüsyonu için uygun bekletme süresi 1 dakika: kimyasal sentezleme sonucu elde edilen HA tozuyla hazırlanan daldırma kaplama solüsyonu için bekletme süresi 3 dakika olarak belirlenmiştir. Tabletlerin yapısında bulunan gözenekler bekletme süresinin arttırılması halinde kapanmaya başlamıştır. Kaplama kalınlıklarının boyun bölgelerinde daha fazla olduğu gözlemlenmiştir. Bu oluşumun sebebi olarak kaplama solüsyonunun kılcal hareketin yönlendirmesi sonucu konkav-konveks yapıya sahip bu bölgelere hücum etmesi öngörülmüştür. Daldırma kaplama yöntemleri ile kaplanan tüm tabletlerin boyun bölgelerinde yoğunlukta olmak üzere kaplama yüzeylerinde çatlaklar gözlenmiştir. Ancak HA tozlarının öğütülmesi kaplamanın homojenliğini arttırmıştır.

Yapay vücut sıvısı içerisindeki Ca ve P oranlarının arttırılması, CaP çekirdeklenme oranını arttırmıştır. Yapılan alkali ve ısıl işlemler CaP oluşumunu hızlandırmıştır. Numune yüzeyinin tamamıyla CaP ile kaplanması için 21 gün süre ile 1xYVS içerisinde bekletilmesi gerektiği, bu sürenin işlem uygulanan numune de ise 14 güne indiği belirlenmiştir. 5xYVS için bu süreler sırasıyla 24 ve 36 saat ; 10xYVS için ise 4ve6 saat olarak belirlenmiştir. Endüstriyel HA tozunun öğütülmesi ile hazırlanan daldarma kaplama metodu gözenekli tabletlerin kaplanması için en uygun yöntem olarak belrlenmiştir, çünkü çatlaksız ve homojen kaplama bu yöntemle sağlanmıştır.

TABLE OF CONTENTS

LIST OF FIGURES

LIST OF TABLES

CHAPTER 1

INTRODUCTION

At the beginning of the 21st century, there have been significant advances in the "biomaterials" science and biotechnology have expanded for the last couple of decades through the wide range of applications in medicine and dentistry. The main purpose of the use of biomaterials is to assist or replace the human organ and improve the patient's quality of life. Materials options for biomedical applications include a wide range of choices of materials that fall into four different groups: metals, ceramics, polymers and their composites. Since most of the currently used biomaterials were developed for general use; not specifically developed for biological applications and hence their effectiveness is questionable. There has been continuing improvements in biomaterials selection and treatment. Interactions between biomaterial and natural tissue have paramount importance in the acceptance of the material by human body and the healing processes. The knowledge of the interactions between the materials and body is essential to aid the designing of the currently applied and new biocompatible biomaterials.

It is known that biomaterials for synthetic bone substitutes have two major requirements: 1) adequate mechanical strength to sustain physiological loads and 2) biological, chemical and physical properties to facilitate tissue attachment, regeneration and/or healing. For example, the use of synthetic bone graft substitutes has been hindered by the difficulty of matching the mechanical properties of bone tissue to a synthetic material that is biocompatible and bioactive. Therefore, recent trend in desigb of orthopedic implants has focused on combinations of strong metallic and bioactive CaP materials, which would satisfy both mechanical and bioactive requirements.

Commercially pure titanium and some titanium alloys including Ti6Al4V are extensively used in biomedical applications especially for bone-anchoring systems including dental and orthopedic implants and osteosynthesis applications. Although bulk properties of these alloys dictate the mechanical properties of biomaterials such as a relatively high strength-to weight ratio, passive surface properties i.e. excellent corrosion resistance and low rates of ion release as well as a high degree of

biocompatibility, bone response and implant success depend on the chemical and physical properties of the surface and they are governed by surface properties.

The elastic moduli of Ti and its alloys are far greater than those of the cortical and spongy bones, leading to the mechanical incompatibility with the bone. Mainly driven by this reason, porous titanium and its alloys have been used in dental and orthopedic applications since the end of the 1960's. Recent studies have shown that the use of porous Ti implants solve the modulus mismatch problem through a higher degree of body fluid transport through three-dimensional interconnected array of pores, providing better interaction with bone and improved implant fixation (Gan and Pilliar 2004). Furthermore, because of low elastic modulus of porous metals as compared with those of bulk metals, implant loosening decreases and implant life-time increases. Although the bioactivity of titanium surface allows the direct growth of the bone tissue, the bone fixation takes several months (Karachalios 2004). Hydroxyapatite (HA) and other Calcium Phosphate (CaP) materials have been known to exhibit excellent bioactive and osteo inductive properties because of their similarity to natural bone mineral. The phenomenon of living bone integration to the implant materials, known as osteo-integration, originally described by Branemark et al. in 1977 and later it was defined literally by Albrektsson et al. in 1981. Due to excellent osteo-integration property, HA is one of the first materials used to coat implant materials. Coating with a CaP material promotes a direct physiochemical bond with human bone, leading to rapid implant fixation and the development of a stable interface between bone and biomaterial surface. HA coatings on metallic implants combine the strength of the metals with the bioactivity of the ceramics. Based on the potential advantages of CaP surface coating for promoting osteoconductivity, a number of alternative techniques have been developed for the coating including ion sputtering, laser deposition, thermal spray, sol-gel, electro deposition and biomimetic techniques (Bigi et al. 2005).

The bone ingrowths into porous material to provide cementless fixation have been described in several different studies (Galante et al. 1971; Cameron, Macnap and Pilliar 1978; Bobyn et al. 1980; Pilliar 1983). Apatite coating is also available for obtaining reliable fixation at relatively short durations of implantation by means of chemical bonding (Hench et al.1971; Jarcho et al. 1977; Ducheyne et al. 1980; Oonishi et al. 1986). The objective of this study is to explore potentially applicable CaP coating processes to a porous Ti6Al4V compact developed for spinal cage applications. Since widely used plasma spray coating is not applicable for coating porous surfaces,

alternative two methods, dip-coating and biomimetic methods as being simple, low cost and applicable to the coating of porous structures, have been selected and investigated for the optimum process parameters that would produce homogenous coating layer on the porous surface while keeping the cells open.

CHAPTER 2

BIOMATERIALS AND THEIR APPLICATIONS

Biomaterial is defined as any substance (other than a drug) or combination of substances synthetic or of natural origin, which can be used for any period of time, as a part of a system which treats, augments or replaces any tissue, organ, or function of the body (Ratner 2004). There are four groups of solid biomaterials: metals, polymers, ceramics, and composites. Since the structures of these materials differ, they have different properties and, therefore, different uses in the body.

Metallic biomaterials are classified as nearly inert materials. Because of their mechanical strength (high tensile and fatigue strength) and biocompatibility, metals have been used superior in clinical orthopedics such as, hip and knee prostheses and fracture fixation wires, pins, screws, and plates since the early 1900s. Although pure metals are sometimes used, alloys (metals containing two or more elements) frequently provide improvement in material properties, such as strength and corrosion resistance. (David 1998). The main considerations in selecting metals and alloys for biomedical applications are biocompatibility, appropriate mechanical properties, corrosion resistance, and reasonable cost. The physiological environment is typically modeled as 37ºC aqueous solution, at pH 7.3, with dissolved gases (such as oxygen), electrolytes, cells, and proteins. Immersion of metals in this environment can lead to corrosion that reduces the biocompatibility of materials. The electrochemical reactions leading to corrosion must be reduced or prevented. In fact, the stability of the oxides present in different metals determines their overall corrosion resistance.

Ti and its alloys, stainless steel, and Co-based alloys are the three main metallic biomaterials used in load–bearing applications. In Table 2.1. important mechanical properties of these metallic implant materials are tabulated. The elastic moduli of stainless steel and Co-Cr alloys are about 10 times higher than that of natural bone (~17 GPa), which gives complications of mechanical incompatibility. Nowadays, titanium and its alloys especially Ti6Al4V are widely used for orthopedic applications as well as dental implants. These materials are biocompatible, highly corrosion resistant, exhibiting a modulus of elasticity of 110 GPa, 5 times grater than that of natural bone.

Ti6Al4V also shows the highest fatigue strength among the other metallic implants as tabulated in Table 2.1.

Table 2.1. Mechanical properties of important metallic biomaterials.
(Source:Murugan and Ramakrishna 2005)

Bimetals	**Young's modulus (GPa)**	**Tensile strength (MPa)**	**Compressive strength (MPa)**	**Hardness (Vickers, kg/mm^2)**	**Fatigue strength (MPa)**
Ti	110	300–740	550	120–200	240
Ti–6Al–4V alloy	120	860–1140	860	310	280–600
Stainless steel	190	500–950	600	130–180	260–280
Co–Cr alloy	210	665–1277	655	300–400	200–300

Typical stress-strain behavior of various kinds of biomaterials used in orthopedics and natural bone are schematically illustrated in Figure 2.1. For cortical bone replacement, metals, ceramics and bioactive ceramics satisfy strength requirements, while others satisfy the strength requirement for the cancellous bone replacement. According to Wolff's law, if a stiffer implant material is placed into bone, the bone will be subjected to reduced mechanical stress that gradually leads to bone resorption. This phenomenon is known as stress-shielding. Although metals are the suitable choice for hard tissue implantation, they are not suitable when stress-shielding phenomenon is considered. It has been recognized that matching the stiffness of the implant with that of the host tissue limits the stress-shielding effect.

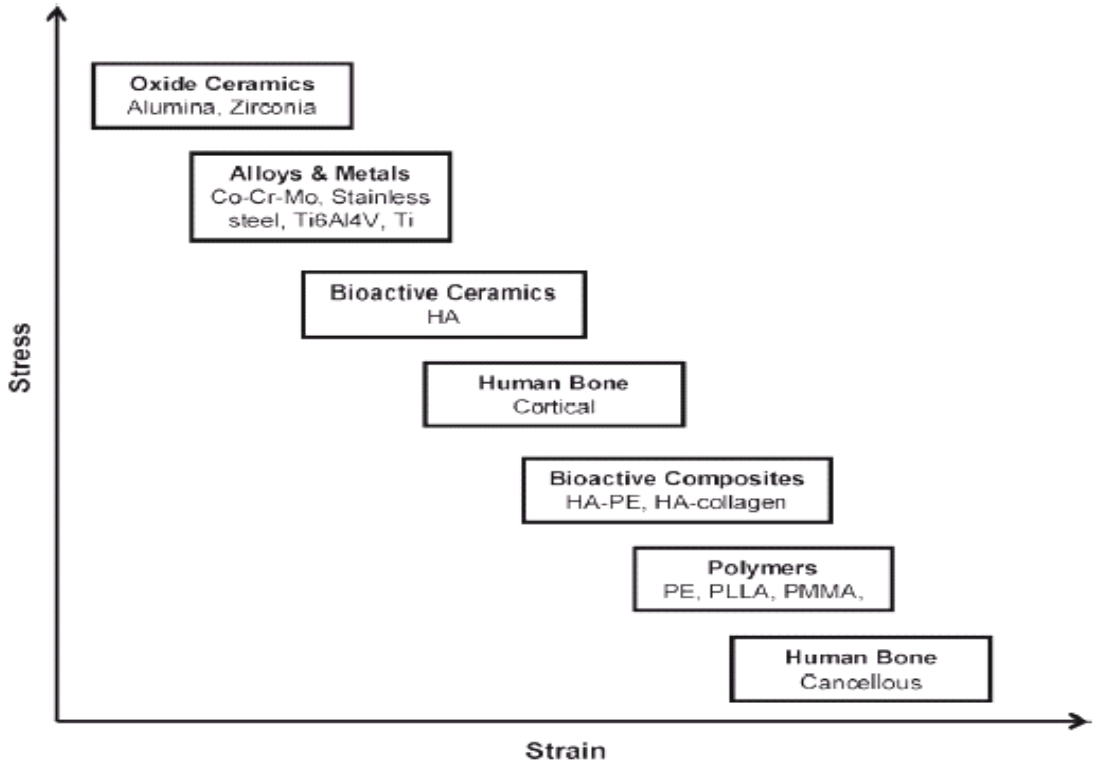

Figure 2.1. Typical stress–strain relationships of a variety of bone implants.
(Source: Murugan and Ramakrishna 2005)

Ceramics are the materials composed of metallic and non-metallic elements held together by ionic and/or covalent bonds. As with metals, the interatomic bonds in ceramics result in long-range three-dimensional crystalline structures. The strong ionic and covalent bonds also make ceramics hard and brittle. They are also highly biocompatible and tissue responsive. The ionic and covalent nature of ceramics also influences their chemical behaviour. Although they do not undergo corrosion, ceramics are susceptible to other forms of degradation when exposed to the physiological environment. Bioceramics are classified into two groups; bioinert and bioactive. Bioactive refers to materials that form bonds with living tissue. Bioactive ceramics do not only undergo slow or rapid dissolution but because of the similarity of calcium phosphates to the mineral component of bone, they may also be resorbed by osteoclasts (the cells that break down bone). The important mechanical properties of widely used ceramic bioceramics are listed in Table 2.2. As tabulated in this table, the major drawbacks to the use of ceramics are their brittleness and poor tensile properties, although they can have outstanding strength when loaded in compression. Bioactive ceramics include synthetic HA, tricalcium phosphate and bioactive glass-ceramics and

are used for artificial bone. Bioinert refers to a material that retains its structure in the body after implantation and does not induce any immunologic host reactions. The clinical use of bioinert bioceramic started in 1970 with alumina owing to its excellent biocompotibility, hardness, strength to resist fatigue, and corrosion resistance. Since 1985, the pure form or partially yittria-stabilized form of zirconia, exhibiting fracture toughness greater than alumina, has been in use in orthopedics. Bioactive ceramic coatings of metals have been developed to overcome the disadvantage of both metal and bioactive ceramic.

Table 2.2. Mechanical properties of bioceramics.
(Source:Murugan and Ramakrishna 2005)

Bioceramics	**Young's modulus (GPa)**	**Tensile strength (GPa)**	**Compressive strength (GPa)**	**Fracture Toughness (MPa $m^{1/2}$)**	**Hardness (HV)**	**Flexural strength (MPa)**	**Density (g/cm^3)**	**Bond strength (GPa)**
Alumina	390	0.31	3.9	5.2	2000	390	3.9	300–400
Zirconia	205	0.42	3	12	1150	1300	6	200–500
HA	80–110	0.05	0.4–0.9	0.7–1.2	600	37	3.16	120

Polymers are the most widely used materials in biomedical applications, including orthopedic, dental, soft tissue, and cardiovascular implants due to their biocompatibility, design, accessibility, functional groups availability, surface modifiability, light weight, ductile nature, and the biodegradation of certain polymers at body pH. Polymers can be categorized into two groups which are biodegradable polymers (polyglycoloic acid, polylactic acid and chitosan) and non-biodegradable polymers (polyethylene and polyethyleneterepthalate). Polyglycolic acid (PGA) is an FDA approved polymer for resorbable sutures. Polylactic acid (PLA) is a similar polymer that is used for screws and plates in bone repair devices. However, combining both of these polymers to create a copolymer, polylactic-co-glycolide (PLGA) creates a strong resorbable implant for bone replacements with controllable properties. The crystallinity, strength and degradation are controlled by the ratio of LA to GA (Jones 2001). It is also possible to modify the end of each polymer chain in order to change the polymer properties through function groups present on polymers (Jones 2001).

Polymers either natural or synthetic are long chain molecules that consist of a large number of small repeating units. Acrylic, nylon, silicone, polyurethane, ultrahigh

molecular weight polyethylene and polypropylene are the commonly used polymers for orthopedic applications. The mechanical and thermal behavior of polymers are influenced by several factors, including the composition of the backbone and side groups, the structure of the chains and the molecular weight of the molecules. The rate of biodegradation can be controlled by manipulating crystallinity of polymer. The mechanical properties of the typical polymers used in biomedical applications are listed in Table 2.3. They all have low elastic moduli and tensile strength, hindering their use in hard tissue replacement.

Composite materials contain two or more distinct constituent materials or phases, on a microscopic or macroscopic size scale. The term composite is usually used for the materials in which the distinct phases are separated on a scale larger than the atomic and in which the properties such as the elastic modulus are significantly altered in comparison with those of a homogeneous material. The properties of the composite materials depend very much on the structure as they do in homogeneous materials. Composites differ from homogeneous materials because considerable control can be achieved over the larger scale structure to have the desired properties. In particular the properties of a composite material depend on the shape of the inhomogeneties, on the fraction of constituents, and on the interface among the constituents (Karageorgiou and Kaplan 2005).

Table 2.3. Mechanical properties of typical polymeric biomaterials.
(Source: Karageorgiou and Kaplan 2005)

Material	**Modulus (GPa)**	**Tensile Strength (MPa)**
Polyethylene	0.88	35
Polyurethane	0.02	35
Polytetrafluoroethylene	0.5	27.5
Polyacetal	2.1	67
Polymethylmethacrylate	2.55	59
Polyethylene terephtalate	2.85	61
Polyethereetherketone	8.3	139
Silicone rubber	0.008	7.6
Polysulfone	2.65	75

2.1. Ti and Ti Alloys

Ti and Ti alloys have been used in a variety of biomedical applications. These include such as implants for dental and orthopedic surgery; prosthesis devices such as total joint replacement, in particular for hip and knee joints; osteosynthesis devices such as bone fracture plates and screws and spinal surgery devices; prosthetic heart valves, artificial hearts, pacemakers, and vascular stent components in cardiac and cardiovascular applications; and bone-anchored hearing aids in audiological applications. The wide use of Ti and its alloys in biomedical applications lies in their high strength, low weight, outstanding corrosion resistance. More than 1000 tonnes of titanium devices of every description and function are implanted in patients worldwide every year (Ratner 2004). Requirements for joint replacement continue to grow as people live longer or damage themselves more by hard sports play or jogging, or are seriously injured in road traffic and other accidents. All forms of titanium forms a thin oxide layer on the surface (primarily TiO_2). For this reason, from the point of view of allergy problems, Ti and its alloys are also advantageous for biomedical applications (Hobkirk and Watson 1995).

The natural selection of titanium for implantation is determined by a combination of most favorable characteristics including immunity to corrosion, bio-compatibility, strength, low modulus and density and the capacity for joining with bone and other tissue-osseointegration. The mechanical and physical properties of Ti alloys combine to provide implants which are highly damage tolerant. The human anatomy naturally limits the shape and allowable volume of implants. The lower modulus of Ti alloys compared to stainless steel is a positive factor in reducing bone resorbtion. Two further parameters define the usefulness of the implantable alloy, the notch sensitivity, - the ratio of tensile strength in the notched vs. un-notched condition, and the resistance to crack propagation, or fracture toughness. Titanium scores well in both cases. Typical NS/TS (the notch sensitivity, - the ratio of tensile strength) ratios for titanium and its alloys are 1.4 - 1.7 (1.1 is a minimum for an acceptable implant material). Fracture toughness of all high strength implantable alloys is above $50MPam^{-1/2}$ with critical crack lengths well above the minimum for detection by standard methods of non-destructive testing (Jones 2001). Commercial pure titanium (Cp-Ti), Ti6Al4V, and Ti6Al4V ELI have been basically developed for structural materials although they are

still widely used as representative Ti alloys for implant materials. Low modulus alloys are nowadays desired because the moduli of alloys are required to be more similar to that of bone. They are composed of nontoxic elements such as Nb, Ta, and Zr. Pure Ti and Ti6Al4V are also the main implant materials are the same as those for surgical implant materials.

Elemental titanium can exist in two forms: the hexagonal close packed (hcp) α and the body centered cubic (bcc) β phase. Ti6Al4V is α+β alloy in which the Al stabilizes α phase and V stabilizes the β phase. Ti6Al4V is usually preferred over α phase Cp-Ti in load bearing applications due to its higher strength and fatigue resistance.

CHAPTER 3

NATURAL BONE AND CALCIUM PHOSPHATE MINERALS

3.1. Natural Bone

3.1.1. Structure of Bone

Natural bone is a composite material made up collagen fiber matrix stiffened by crystallized or amorphous form of HA that account 69% of the weight of the bone. As tabulated in Table 3.1. collagen fibers make up about 20 wt% of bone and in a bundled array of cross-linked helical polypeptide strands, provide extra strength allowing bones to flex under stress. The diameter of the collagen micro fibers varies from 100 to 2000 nm. Additionally, water and other organic materials such as proteins, polysaccharides and lipids are also present in small quantities. There are other mineral ions in bone structure such as citrate ($C_6H_5O7^{4-}$), carbonate (CO_3^{2-}), fluoride (F^-) and hydroxyl ions (OH^-) which may produce some of the subtle differences in microstructural features of bone.

Table 3.1. The overall composition of the bone.
(Source:Murugan and Ramakrishna 2005)

Inorganic phase	**wt%**	**Organic phase**	**wt%**
Hydroxyapatite	60	Collagen	20
Carbonate	4	Water	9
Citrate	0.9	Non-collagenous proteins(osteocalcin, Osteonectin, osteopontin, etc.)	3
Sodium	0.7		
Magnesium	0.5		
Other traces: Cl^-, F^-,K^+, $Sr^{2+}Pb^{2+}$,Zn^{2+}.Cu^{2+}.		Other traces: Polysaccharides, lipids, cytokines Primary bone cells : osteoblast, osteocytes, osteoclasts	

As a living tissue, bone accomplishes its functions throughout its lifetime by continually adapting to changes in its biological environment. The hormonal changes and lifestyle determine the characteristics of bone's structural adaptation. Experimental studies and computational models have been developed to predict the response of bone to different changes in its environment. Apart from the mechanical function, bone is also known to serve physiological purposes as reservoir for nutrients such as calcium and a manufacturing facility for red blood cells.

The bone structure is classified according to its porosity: *cortical bone* (also referred to as compact or dense bone) and *trabecular bone* (also referred to as cancellous or spongy bone) (Figure 3.1.). Cortical bone has a porosity ranging between 5% and 10%, and it is usually found along the exterior shaft section of long bones. Trabecular bone has higher porosity levels, ranging between 75% and 95%. It is usually found in cubicoidal bones (e.g., vertebrae), flat bones (e.g., pelvis) and the end of long bones (e.g., femur). The non-mineralized spaces within trabecular bone contain bone marrow, which is a tissue composed of blood vessels, nerves and various types of cells. Cortical bone accounts for about 80% of the total skeletal mass while trabecular bone constitutes some 70% of the skeletal volume.

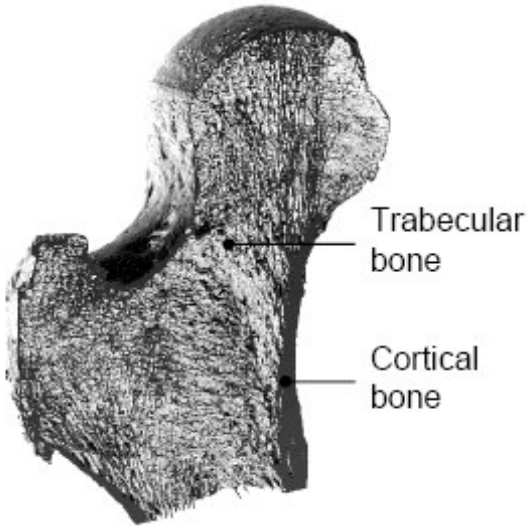

Figure 3.1. Bone classification according to the porosity level.
(Source: Murugan and Ramakrishna 2005)

At the tissue level, the scale of 100 μm to 1 mm, major differences can be identified within the cortical and trabecular structures. Cortical bone is composed of repeating units called *osteons* or Haversian systems (Figure 3.2.). The osteons are cylindrical at about 200-250 μm in diameter running roughly parallel to the centerline axis of the bone. The central cavity inside an osteon is known as the *Haversian canal*. Haversian canals are typically 40 to 50 μm in diameter and run along the long axis of a bone. Haversian system or osteons have concentric layers of the mineralized collagen fibers called lamellae, which deposited around a central called Haversian canal, containing blood vessels and nerves that service the bone. Normally a blood vessel (15 μm in diameter) as well as nerve terminations is found inside Haversian canals. *Volkmann's canals* are short transverse channels connecting the Haversian canals. These canals also contain blood vessels and nerves (Martin et al. 1998).

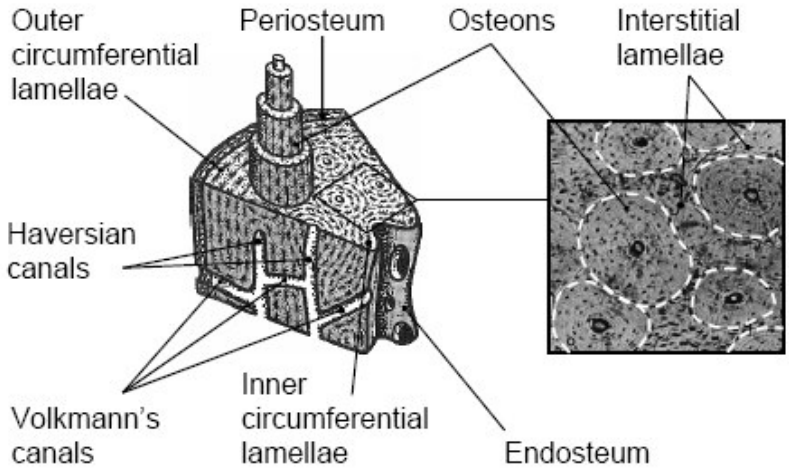

Figure 3.2. Cortical bone mesostructure
(Source: Murugan and Ramakrishna 2005)

The mesostructure of trabecular bone is composed of plates and struts called *trabeculae*. Sometimes trabeculae appear organized into orthogonal arrays, but they are often more randomly arranged. Each trabecula is about 200 μm thick (Figure 3.3.). Thick trabeculae contain a blood vessel and some osteon-like structure. In a trabecula, *trabecular packets*, which are the product of new tissue formed after remodeling, can be found. A typical trabecular packet is about 50 μm thick and 1 mm long.

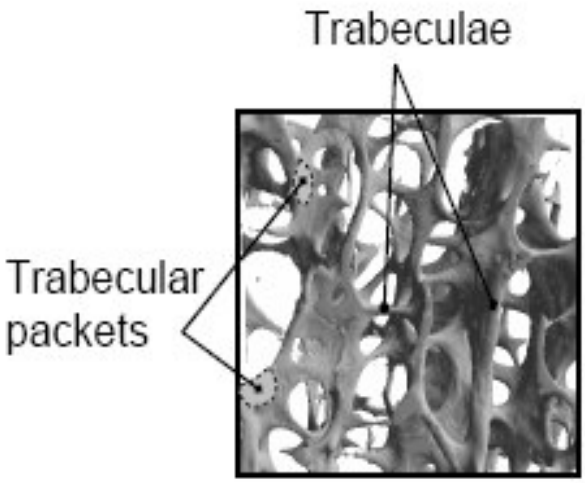

Figure 3.3. Trabecular bone mesostructure.
(Source: Murugan and Ramakrishna 2005)

The compact cortical bone has higher mineral content mainly composing of hydroxyapatite, and little soft tissue. It can therefore withstand the forces applied on the skeletal during function. The soft trabecular bone on the other hand has lower content of minerals and comparatively more soft tissue. There are three types of bone cells: the osteoblasts are responsible for the formation of new bone, the osteoclasts resorb bone and the osteocytes, sometimes considered mature osteoblasts, are surrounded by bone tissue exerting regulatory functions on bone metabolism.

3.1.2. Mechanical Properties of Bone

Organic components of bone behave as a compliant material with high toughness, and low modulus. Inorganic components provide appropriate stiffness to the bone. As a ceramic organic composite, bone exhibits poor impact resistance and fracture easily. Representative stress-strain curve of bone shows a linear elastic region, followed by a flat plastic region at about 0.8% strain as shown in Figure 3.4. Failure occurs at strains up 2%. An important point is that bone is a tough material at low strain rates but fractures more like a brittle material at high strain rates as seen in Figure 3.4.

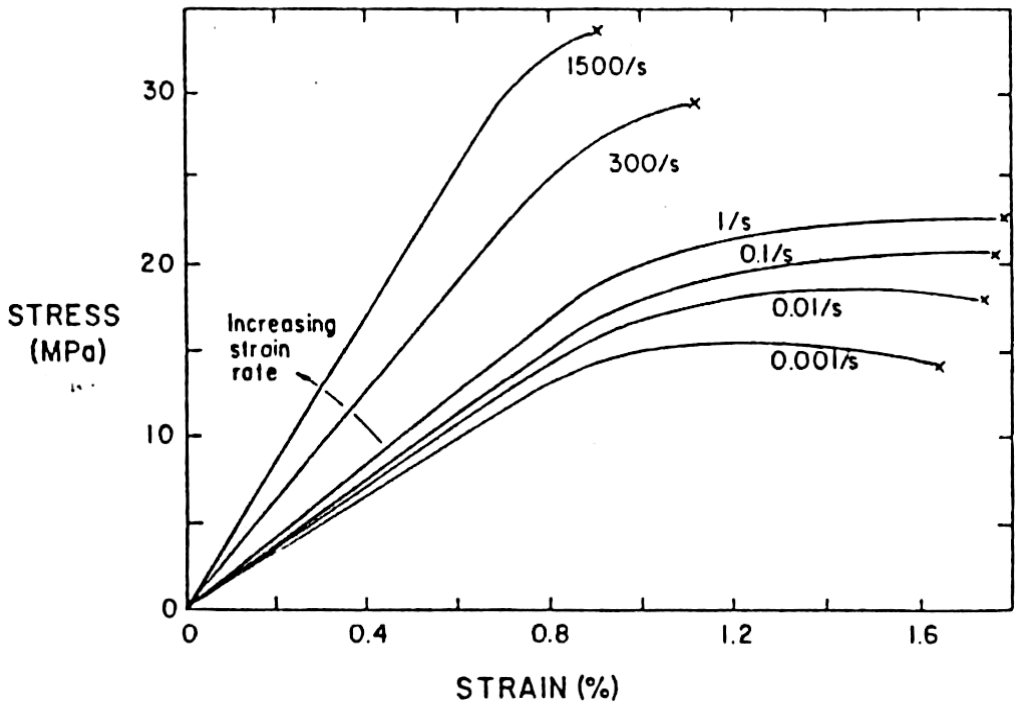

Figure 3.4. Stress as a function of strain and strain rate for human compact bone. (Source: Rho 1998)

Mechanical properties of the cortical and cancellous bone are quite different as tabulated in Table 3.2. Cortical bone is stiffer than cancellous bone and can sustain greater stress but less strain before failure. Cancellous bone can sustain strains of 75% before failing in-vivo, but cortical bone will fracture if the strain exceeds 2%. Cancellous bone has a greater capacity to store energy compared to cortical bone. Elastic modulus and compressive strength of cancellous bone are lower than those of cortical bone. The mechanical properties of bone depend on the humidity, bone density, porosity, orientation of the collagen fibers, and kind of bone, and direction of the applied load. The strength and the modulus of elasticity of the human bone are further affected by ageing and decrease dramatically with age.

Table 3.2. The mechanical properties of human cortical and cancellous bone (Source:Murugan and Ramakrishna 2005)

Proporties	Measurements	
	Cortical Bone	Cancellous Bone
Young's modulus (GPa)	14–20	0.05–0.5
Tensile strength (MPa)	50–150	10–20
Compressive strength (MPa)	170–193	7–10
Fracture toughness (MPa $m^{1/2}$)	2–12	0.1
Strain to failure	1–3	5–7
Density (g/cm^3)	18–22	0.1–1.0
Apparent density (g/cm^3)	1.8–2.0	0.1–1.0
Surface/bone volume (mm^2/mm^3)	2.5	20
Total bone volume (mm^3)	$1.4 \cdot 10^6$	$0.35 \cdot 10^6$
Total internal surface	$3.5 \cdot 10^6$	$7.0 \cdot 10^6$

3.2. Calcium Phosphate Minerals

Calcium Phosphates are the main mineral constituent of teeth and bones. The inorganic constituent of bone is made up biological apatites. These apatites, along with fluorapatite (FAp, $Ca_5(PO_4)_3$), monetite (M, $CaHPO_4$), tricalcium phosphate (TCP, $Ca_3(PO_4)_2$), tetracalcium phospate (TTCP, $Ca_4(PO_4)_2$), and octacalcium phosphate (OCP, $Ca_8H_2(PO_4)_{6.5}H_2O$) belong to a family of minerals known as apatites. These materials demonstrate similar structural formula as $X_3Y_2(TO_4)Z$. In nature, apatite compositions include X and Y = Ca, Sr, Ba, Re, Pb, U or Mn; T = P, As, V, Si, S, or C; and Z = F, Cl,OH, or O. In biomedical application, apatites of interest possess X = Y = Ca, T = P, and Z = F or OH. For example, the apatite is called hydroxyapatite (HA) when T = P and Z = OH. The mineral HA ($Ca_{10}(PO_4)_6OH_2$) and brushite ($CaHPO_4.2H_2O$) are structurally similar to biological apatites. Only these two forms of

calcium phosphates are stable at the body temperature and in body fluid. At pH<4.2 the stable calcium phosphate phase is brushite. At pH> 4.2 the stable phase is HA.

The atomic ratio of Ca/P in calcium phosphates can be varied between 1.5 and 2 to produce compounds ranged from TTCP, HA to TCP. Table 3.3. summarizes the mineral names, chemical names and composition of various phases of calcium phosphates. Their solubility and speed of hydrolysis increase with decreasing Ca/P ratio, for this reason only certain compounds are useful for implantation in the body. Driessens (1983) stated compounds with a Ca/P ratio less than 1:1 are not suitable for biological implantation. Tooth enamel has a Ca/P ratio of 1.59-1.63, and underlying dentin has a Ca/P ratio of 1.61. Bone has been reported to have a Ca/P ratio of 1.65-1.71 (Chen 2005, Leamy 1998, LeGeros 1991).

Table 3.3. The mineral names, chemical names and composition of various phases of calcium phosphates. (Source: Ratner 2004)

Ca : P	**Mineral name**	**Formula**	**Chemical name**
1.0	Monetite	$CaHPO_4$	Dicalcium phosphate (DCP)
1.0	Brushite	$CaHP0_4.2H_2O$	Dicalcium phosphate dhiydrate (DCPD)
1.33	—	$Ca_8(HPO_4)_2(PO_4)_4.5H_2O$	Octacalcium phosphate (OCP)
1.43	Whitlockite	$Ca_{10}(HPO_4)(PO_4)_6$	
1.5	—	$Ca_3(PO_4)_2$	Tricalcium phosphate (TCP)
1.67	Hydroxyapatite	$Ca_{10}(PO_4)_6OH_2$	
2.0	—	$Ca_4P_2O_9$	Tetracalcium phosphate

Each of the calcium phosphate phases has a different rate of dissolution in aqueous environments and different degree of bioactivity. The rates of dissolution decrease in the following order: amorphous HA>>TTCP>α-TCP>OHA>>β-TCP>>HA. Crystalline HA is the most stable phase within the body while amorphous HA dissolves the fastest. For this reason, crystalline HA is one of the main phases of CaP that have been studied extensively and used clinically.

3.2.1. Hydroxyapatite

HA is recognized as a good bone graft material because it forms a strong chemical bond with host bone tissue. Pure HA has the theoretical composition of 39.68 wt% Ca, 18.45 wt% P, 38.22 wt% O and 3.38 wt% OH, with Ca/P ratio of 1.67. Hydroxyapatite forms a hexagonal rhombic crystal structure with a space a six-fold c-axis perpendicular to three equivalent a-axis (a1, a2, a3) at angles 120° to each other. Figure 3.5. shows the crystal structure of HA. Unit cell consists of Ca, PO_4 and OH groups closely packed together. The dimensions of the unit cell of HA are a-axis = 0.9422nm, c-axis = 0.6880nm (Hench et al, 1998). Hydroxyl ions (OH^-) sit at the corners of the basal plane. These ions are positioned at every 3.44Å (one half the unit cell), parallel to the c-axis and perpendicular to the basal plane. Thus 60% of calcium ions in the unit cell are associated with the hydroxyl ions. The hydroxyapatite lattice contains two kinds of calcium positions columnar and hexagonal. Four "columnar calcium" ions that occupy the [1/3, 2/3, 0] and [1/3, 2/3, 1/2] lattice points. Six "hexagonal calcium" ions are located on planes parallel to the basal plane at c = 1/4 and c = 3/4 and the six PO_4^{3-} tetrahedra are also located on these plane. The density of this material is 3.219 g/cm^3. In Table 3.4. physicochemical, mechanical, and biological properties of crystalline HA are tabulated.

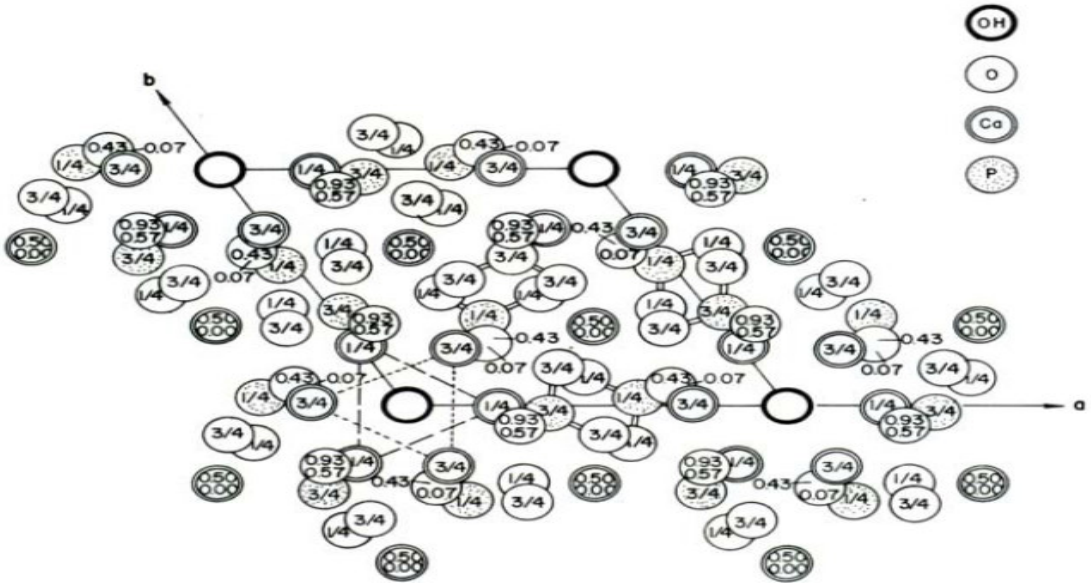

Figure 3.5. Crystal structure of HA

(Source: Ratner 2004)

The excellent biocompatibility of HA has been substantiated by both in vivo and in vitro studies. HA is not only bioactive but also osteoconductive and non-toxic. The bonding of bone to HA occurs by physicochemical bonding as bone cell proteins interact with HA to form direct ionic, electrostatic, hydrogen, and van der Waal bonds. The osteoconductive nature of HA coatings results in the formation of strong bonds with bone. The fracture toughness of HA is reported to be approximately 1.0 MPa $m^{1/2,}$ which is very low compared to natural bone (2-12 MPa $m^{1/2}$). It behaves as a typical brittle material.

Table 3.4. Physicochemical, mechanical, and biological properties of HA. (Source: Suchanek and Yoshimura 2002)

Properties	**Experimental data**
Chemical composition	$Ca_{10}(PO_4)_6(OH)_2$
Ca/P molar ratio	1.67
Crystal system	Hexagonal
Space group	$P6_3/m$
Cell dimensions (Å)	a = b = 9.42,c = 6.88
Young's modulus (GPa)	80-110
Elastic modulus (GPa)	114
Compressive strength (MPa)	400-900
Bending strength (MPa)	115-200
Density(g/cm^3)	3.16
Relative density (%)	95-99.5
Fracture toughness ($MPam^{1/2}$)	0.7-1.2
Hardness (HV)	600
Decomposition temperature ($^{\circ}C$)	> 1000
Melting point ($^{\circ}C$)	1614
Dielectric constant	7.4-10.47
Thermal conductivity (W/cm K)	0.013
Biocompatibility	High
Bioactivity	High
Biodegradation	Low
Cellular-compatibility	High
Osteoinduction	Nil
Osteoconduction	High

There are many techniques that have been used for hydroxyapatite coatings on metallic implant materials. Dip coating, electrophoretic deposition, hot isotatic pressing, pulsed laser deposition, sol-gel processing, thermal spraying, biomimetic process and sputter coating have been used to deposit hydroxyapatite coatings.

CHAPTER4

HA COATING METHODS

4.1. Sol-Gel Method

The sol-gel method is a wet-chemical synthesis technique for the preparation of oxide gels, glasses, and ceramics at relatively low temperatures. Sol-gel reactions occur in a series of metal alkoxides (MA) hydrolysis and condensation reactions. As early as the mid-1800s, interest in the sol-gel processing of inorganic ceramic and glass materials has begun with Ebelman and Graham's studies on silica gels (Kim et al. 2004, Jillavenkatesa and Condrate 1998). In the 1950s, Roy and co-workers synthesized a variety of novel ceramic oxides with relatively high levels of chemical homogeneity using sol-gel method. It is possible to fabricate, using sol-gel method, ceramic or glass materials in a variety of forms including ultra-fine powders, fibers, thin films, porous aerogel materials or monolithic bulky glasses and ceramics (Maviş and Taş 2000, Lopatin et al. 2001).

The sol-gel process is based on the transition from a liquid 'sol' (colloidal solution) into a 'gel' phase. Metal alkoxide are usually used as precursors due to their ability to readily react with water. A metal alkoxide has the generic structure $M\text{-}(OR)_x$, and is a molecule consisting of a central metallic ion (M) bound to functional organic groups (-R) through an oxygen linkage (O). Tetramethoxysilane (TMOS) and tetraethoxysilane (TEOS) are common metal alkoxide precursors.

Generally three reactions are used to describe the sol-gel process: hydrolysis, alcohol condensation and water condensation. These reactions are as follows:

$$\begin{array}{c} | \\ \text{—Si —} \\ | \end{array} \text{OH} + \begin{array}{c} | \\ \text{— Si—} \\ | \end{array} \text{OH} \underset{\textit{Hydrolysis}}{\overset{\textit{Water Condensation}}{\rightleftharpoons}} \begin{array}{c} | \\ \text{—Si —} \\ | \end{array} \text{O} \begin{array}{c} | \\ \text{— Si—} \\ | \end{array} + \text{H— OH} \qquad (4.1.)$$

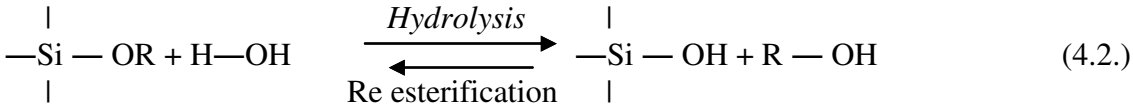

(4.2.)

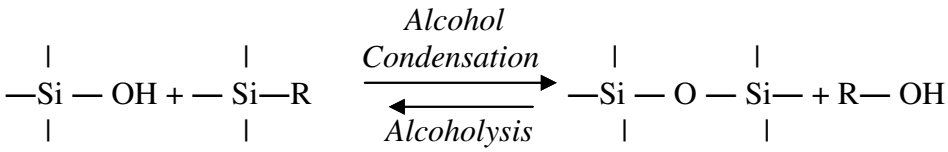

(4.3.)

Because water and alkoxides are immiscible, alcohol is commonly used as co-solvent. Due to the presence of a co-solvent, the sol-gel precursor, alkoxide, mixes well with water to facilitate the hydrolysis. During the hydrolysis reaction, the alkoxide groups (-OR) are replaced with hydroxyl group (-OH) through the addition of water. Although hydrolysis can occur without additional catalyst, the speed and extent of the hydrolysis reaction can be enhanced when they are employed. Under acidic conditions, the alkoxide group is protonated rapidly in a first step. As a result, electron density is withdrawn from the silicon atom, making it more electrophilic and thus more susceptible to attack from water. This results in the formation of a penta-coordinate transition state with significant SN2 type character. When the nucleophile attacks the center atom, Si, it's on the opposite side to the position of the leaving group, R-OH. Finally the transition state decays by breaking of the Si-OHR bond and ends up with an inversion of silicon configuration as shown in Equation 4.4. The acid-catalyzed mechanism can be described as following:

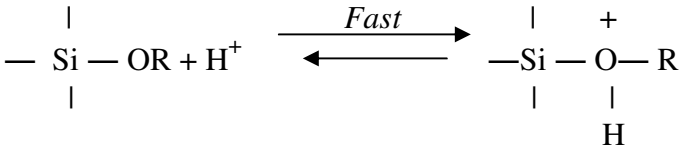

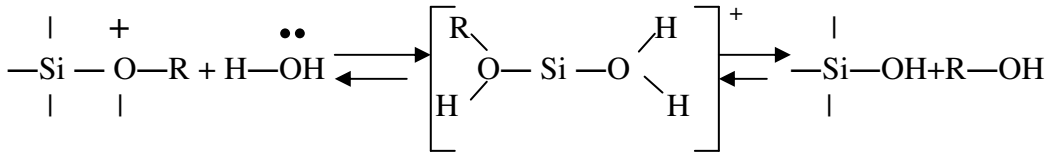

(4.4)

Under basic conditions, the hydroxyl anion works as nucleophile and attacks the silicon atom. Again, an SN-2 type mechanism has been proposed in which the -OH

displaces -OR with inversion of the silicon tetrahedron. (Equation 4.5.)The base-catalyzed mechanism can be described as following:

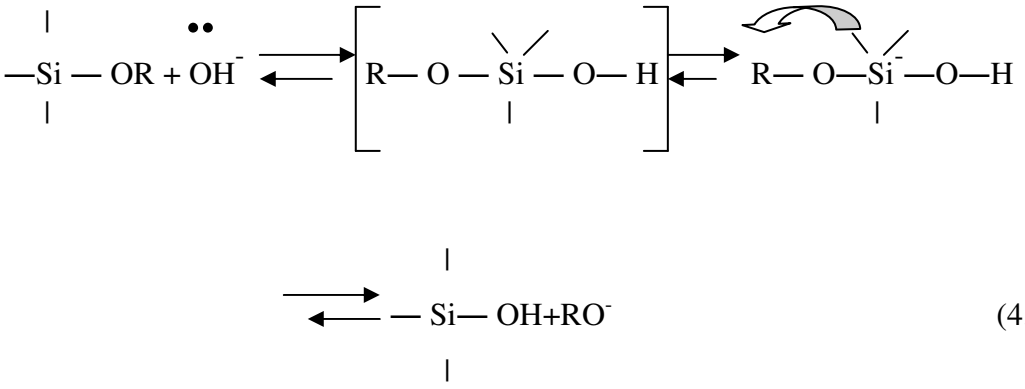

(4.5.)

In the gelation step, alkoxide gel precursor undergoes polymerization (condensation) reaction with by-product of water or alcohol. Condensation reaction involving silanol group (Si-OH) produces siloxane bonds (Si-O-Si) with by-product of water (water condensation) or alcohol (alcohol condensation). As the number of siloxane group increases, they bridge with each other and a silica network is formed. Similar to hydrolysis, the condensation reaction is also affected by the acid/base catalyst. With the existence of acid catalyst, weakly-crosslinked polymer is formed and can easily aggregate after drying yielding low-porosity microporous structure. On the contrary, if base catalyst is used, discrete highly branched clusters are formed and lead to a mesoporous structure after gelation. Very important chemical and physical changes continue during aging. During this process, further cross-links continue and the gel shrinks as the covalent links replace non-bonded contacts and the pore sizes and pore wall strengths change with the evolution of the gel's structure.

A high ratio of water and three dimensional inter-connected pores are inside the gel structure. To remove the liquid trapped in the interconnected pores before the pore is closed in the densification step, drying is necessary. On the other hand, removal of the liquid from the tiny pores causes significant stress resulting from inhomogeneous shrinkage. Therefore the main problem that has to be overcome is cracking due to the large stress in the structure. For small cross sections, such as powder, coating, or fiber, the drying stress is small and can be accommodated by the materials, so no special care is needed to avoid cracking of sol-gel structures. While for monolithic objects greater than 1 cm, drying stress developed in ambient atmosphere can introduce catastrophic

cracking; therefore, the control of the chemistry of each processing step is necessary to prevent cracking during drying.

With further heat treatment at high temperature, the organic residue in the structure is taken out, the interconnected pores collapse and a densified glass or ceramics is formed. The densification temperature may depend on the dimension of pores, the degree of interconnection of the pores and the surface area. For example, drying at around room temperature can be enough to produce functional organic or biological materials however; production of dense glass or ceramics materials requires heat treatment at high temperature.

Sol-gel processes have advantages such as, increasing homogeneity due to mixing on the molecular level, reducing heating rate due to much smaller particle sizes with high surface area, having ability to produce uniform fine grained structures by the use of different chemical routes and their easy of application to complex shape with range of coating techniques. Despite all the advantages, sol-gel method has limitations. Solvents, such as alcohol and water, used in the process may not be appropriate for the production of large quantities of materials considering for example the cost. Furthermore, solvent removal during drying generally causes stress which induces cracks upon drying. These cracks may not be healed after densification. Hence, careful attention is needed to avoid cracking.

Figure 4.1. schematically summarizes possible routes for materials having different microstructure starting from a sol. As seen in the figure, while dense materials can be obtained after gelation and drying stages, it is possible to produce dense thin film coated materials by using spray, dip or spin coating methods without gelation step. In this study, dip coating method was selected and investigated for the coating of sintered Ti6Al4V powder compacts.

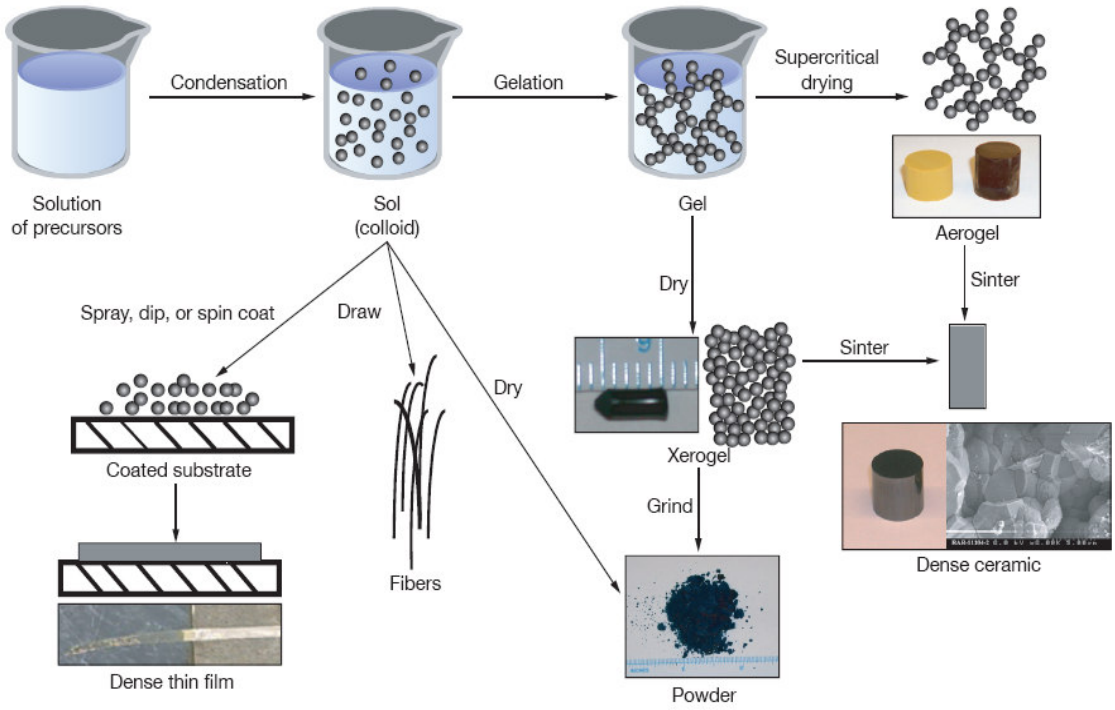

Figure 4.1. Routes for material processing having different microstructure starting from a sol. (Source: Brinker and Hurd 1994)

4.1.1. Dip-Coating and Application to Ti Bulk and Porous Implants

Thin films formed by a dip-coating process represent one of the oldest commercial applications of sol-gel technology. Fundamentals of sol-gel dip coating method were described by C. Jeffrey Brinker and Alan J. Hurd (Brinker and Hurd 1994). The dip-coating method composes of three stages as seen in Figure 4.2.(a), (b) and (c). These are start-up and immersion, deposition and drainage, and evaporation. Figure 4.2. (d) shows the continuous dip coating process schematically.

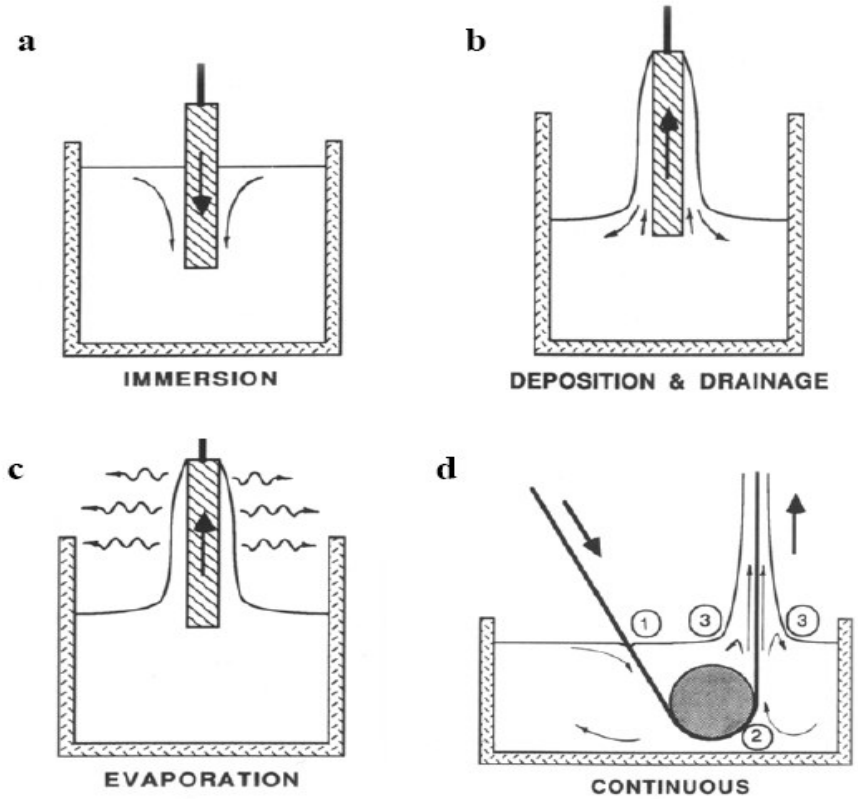

Figure 4.2. Stages of the dip-coating process.
(Source: Brinker and Hurd 1994)

In the dip-coating approach, there are six competing forces acting in the film deposition region that determine the position of the streamline which determines the film thickness (Brinker and Hurd 1994). Since the sol-gel coating with low viscosity is deposited at slow withdrawal speed, the viscous drag and gravity forces are not balanced by the applied film thickness. To properly balance the forces, a modification of the liquid-vapor surface tension, γ_{LV}, is imposed by the liquid-vapor interface, which leads to the following film thickness relationship (Brinker and Hurd 1994).

$$h = 0.94(\eta U_o)^{2/3} / \gamma_{LV}^{1/6} (\rho g)^{1/2} \qquad (4.6.)$$

where h is the coating thickness, η is the solution viscosity, U_0 is the withdrawal rate, ρ is the density of the sol, and g is the gravitational acceleration.

Figure 4.3. (a) shows the sequential stages of structural development that result from draining accompanied by solvent evaporation and continued condensation reactions where *h(x)* is the film thickness at position *x* measured from the drying line α_o,

h_o is the entrained film thickness just above the stagnation point S, P_o is the capillary pressure and θ is the wetting angle. Figure 4.3.(b) shows the details of the flow patterns (streamlines) during dip coating where δ is the boundary layer.

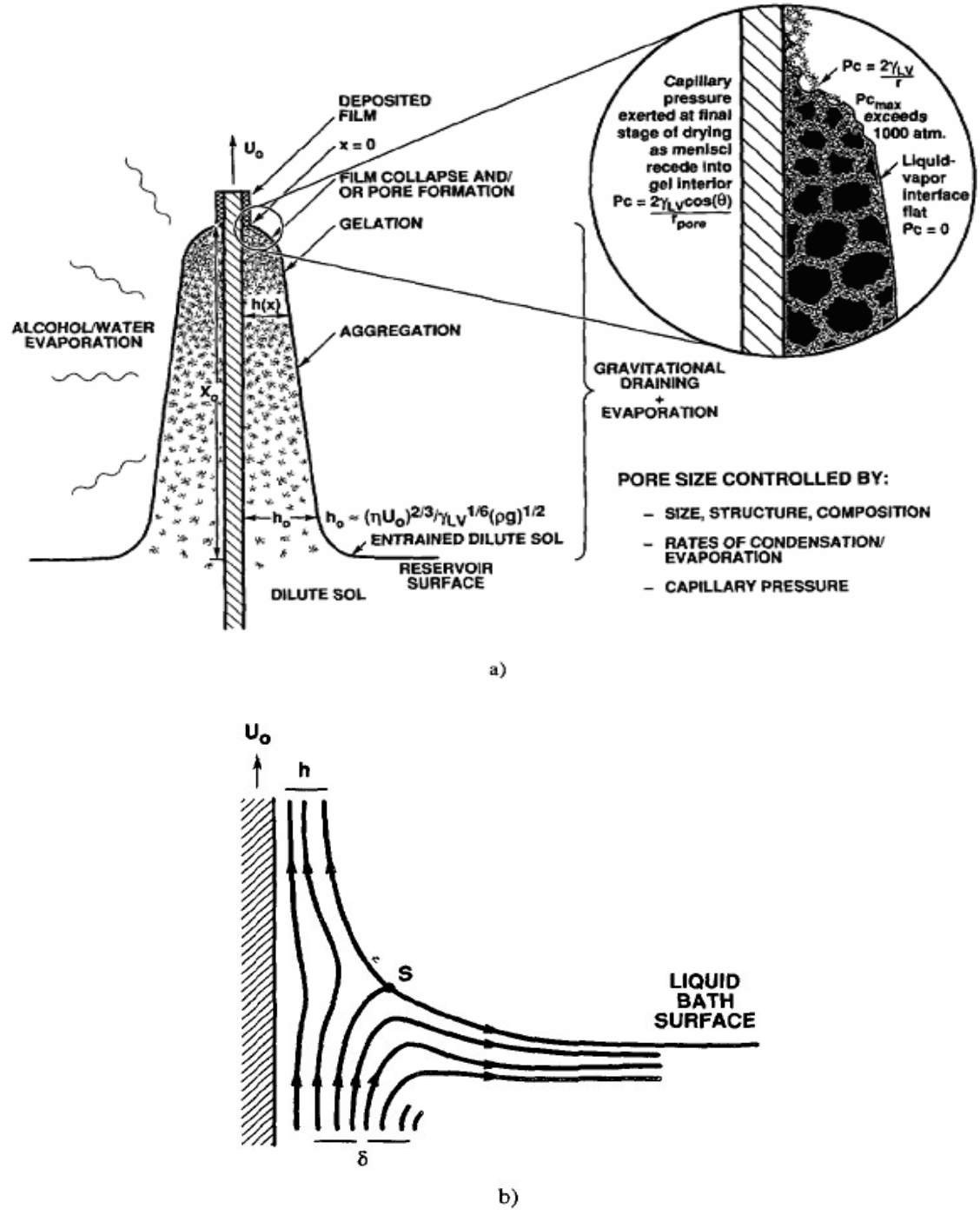

Figure 4.3. (a) Schematic of the steady-state dip-coating process and (b) detail of the flow patterns (streamlines) during dip coating (Source: Brinker and Hurd 1994)

Brinker et al. suggested that film formation in sol-gel coating is also governed by the competing processes of gravitational draining and solvent evaporation. When the polymeric species are concentrated on the substrate surface, the processes are accompanied by condensation reactions. Since the drying stage overlaps with the aggregation-gelation stage, there is only a brief time for condensation. Furthermore, there is an added competition between solvent evaporation (which compacts the structure) and condensation (which stiffens the structure). Eventually, compliant structure is collapsed by the capillary pressure created by the liquid-vapor meniscus given by the equation

$$P=2\gamma_{LV}\cos(\theta) / r \qquad (4.7.)$$

where r is the pore radius. Equations 4.6. and 4.7. demonstrate that the properties of the dip-coating film are controlled by the withdrawal rate, the viscosity of the sol, the precursor structure in the sol, and the capillarity of the sol. These conditions permit rearrangement of the species upon drying, so that cracking and poor adhesion between the film and the substrate can be avoided.

Thin film formation by sol-gel process followed by dip coating method can be used in wide variety applications when controlling chemical, physical and structural properties of thin film is crucial. Moreover, various materials can be used as coating materials onto numerous different materials. For example, CaP/HA coatings have been obtained from both inorganic and organic sol-gel routes onto several different materials (Gan and Pilliar, 2004).

Liu et al. in 2000 synthesized HA ceramics through a sol-gel route using triethyl phosphite and calcium nitrate as phosphorus and calcium precursors, respectively. It was confirmed that the types of initially diluted media (i.e., water vs. anhydrous ethanol) were not effective in microstructural evolution and crystallinity of the resulting HA ceramics. The crystal size and HA content in both ethanol and water based gels increased with increasing calcination temperature. A porous HA coating was deposited onto a Ti metal substrate using the sol-gel route. It was claimed that the open porosity in the coating enables the circulation of physiological fluids to provide nutrients when it is used for biomedical applications.

In another study, Nguyen et al. in 2004 investigated the bone ingrowths properties of a Ti6Al4V implant, which contained a sintered porous surface. The porous

implants were produced through sintering of Ti6Al4V powder and tested with or without the CaP coating. The coating was performed using a sol–gel coating technique procedure the same as with Liu et al. The implants were inserted transversely across the tibiae of 17 rabbits for two weeks. The presence of a sol–gel formed poorly crystallized HA film layer on the sintered porous surface layer of Ti6Al4V implants was found to significantly increase the rate of bone ingrowth into the porous region thereby resulting in faster implant fixation and osseointegration. The CaP film also promoted more complete bone fill of the pore regions. These findings suggested that such sol–gel formed CaP films over porous-surface structures were effective in enhancing osteoconductivity. Bone formation along the porous implant surface was also measured in relation with the medial and lateral cortices as an indication of implant surface osteoconductivity. The Absolute Contact Length measurements of endosteal bone growth along the porous zone were greater in the CaP-coated implants as compared with the non-CaP-coated implants. The CaP-coated implants also displayed a trend towards a significant increase in the area of bone ingrowth. Finally, it was shown in the same study that there was significantly greater bone-to-implant contact within the sinter neck regions of the CaP-coated implants.

In a parallel study by Gan et al. 2004, nanocrystalline or sub-micron crystalline carbonated HA films were formed by an inorganic coating route differentiated and displayed a more irregular surface texture. The resulting carbonated HA films had significantly different Ca/P ratios. Cross-sectional TEM studies revealed an interfacial reaction product phase of calcium titanium oxide in the film formed by inorganic route only. The two different coating surface topographies were suggested as good model systems for in-vivo studies to differentiate the effect of surface topography and surface chemistry on the osteoconductivity and osseointegration.

The necessity of controlling the aging time of the precursor sol as function of the sol temperature to obtain a monophasic HA coating was shown by Regi et al. 2000. For this purpose, aqueous solutions of calcium nitrate and triethyl phosphite were chosen due to the rapid hydrolyzation of alkyl phosphates and also because the presence of oxidant agents such as nitrate anions would favor the decomposition of ethyl groups during the synthesis process. HA films deposited by dip-coating using different precursor-sols with varying ethanol/water ratios were used to coat metallic surfaces in order to establish the optimum conditions for the technological development of the sol–gel technique. Nanocrystalline carbonate hydroxyapatite coatings onto metallic

substrates were prepared with different the ethanol/water content. It was shown that, a control of the aging time was necessary to avoid the formation of a mixed surface coating layer. All the investigated sols formed uniform and homogeneous film on the substrate while the presence of ethanol increased the uniformity of the coating. The HA coatings obtained showed good peeling strength, 20 MPa, and a bioactive behavior under in vitro conditions, inducing bone-like apatite formation on the surface when immersed in SBF.

Chin et al. 2001, studied the effect of rapid-heating on the coating of hydroxyapatite on Ti6Al4V alloy using a sol-gel method. The fast decomposition of the precursor deposited on the substrate during rapid-heating was shown to promote the ingrowth of living cells.

Hydroxyapatite (HA) was coated onto titanium (Ti) substrate with the insertion of a Titania (TiO_2) buffer layer using the sol–gel method (Kim et al. 2004). The bonding strength of the HA/TiO_2 double layer coating on Ti was markedly improved when compared to that of the HA single coating on Ti.

Maviş and Taş 2000, studied the development of recipes of appropriate solutions for the dip coating of HA on Ti6Al4V substrates, using chemically precipitated hydroxyapatite precursor powders. They developed calcium hydroxyapatite (HA) dip-coating-solution recipes to coat Ti-6Al-4V substrates. The organic additives used in the solutions consisted of poly (ethylene glycol), glycerol, and/or gelatin. The HA dip-coating solution recipes did not require the drying of the green, coated strips under controlled humidity conditions. Calcination of the HA dip-coated Ti6Al4V strips was performed in a nitrogen-gas atmosphere at a temperature of 840°C. The HA coatings obtained were highly porous with the bonding strengths of 30 MPa.

4.2. Thermal Spray Coating

Thermal sprayed coating methods have been used for at least 40 years. A wide range of materials can be thermal sprayed for a variety of applications, ranging from turbine technology to the biomedical industry. Different substrates can be coated using different coating materials for different applications. Zinc, aluminum, and zinc-aluminum alloy coatings are important anticorrosive coatings. For infrastructure

applications polymer or plastic coatings have also been developed. HA coatings have been used on medical prosthetic devices and implants such as joint replacement.

Thermal Spray allows to feed metallic, ceramic, and some polymeric materials in the form of powder, wire or rod into a torch or gun where they are heated to near or somewhat above their melting point (Garrett et al. 2006). Thermal spray coatings consist of many layers of thin, overlapping, essentially lamellar particles. As the material is introduced into the spray gun, the particles receive thermal energy from the high velocity gas and melt into droplets. The droplets receive kinetic energy from the high velocity gas and move towards the target where they impinge upon the surface like a "splat". On contact with the target surface, the droplets transfer thermal energy to the substrate through conduction and revert back to a solid. As they cool, they shrink, inducing a mechanical interlocking structure. Substrate surface is an important parameter to achieve coating process. For this reason, the substrate needs to be cleaned to remove any contaminants at surface. Thermal spray processes may be classified as either combustion or electric processes. Combustion processes include flame spraying, high-velocity oxyfuel (HVOF) spraying, and detonation flame spraying. Electric processes include arc spraying and plasma spraying.

4.2.1 Plasma Spray Coating

Low temperatures restrict early forms of thermal spray since they are produced by an oxyacetylene flame or an electric arc. Materials with melting points of 2700 °C and higher cannot be sprayed. Attempts to extend the temperature range of the heat source lead to the development of plasma spraying. Plasma is the highly ionized state of mass, consisting of molecules, atoms, ions, electrons, and light quantum (Xiao et al. 2005).

Plasma gases used for thermal spraying include Argon, Helium, Hydrogen, and Nitrogen. Plasma gases are selected on the basis of the desired temperature and the velocity of the plasma beam and the degree of inertness in the sprayed material and substrate generally uses argon as the plasma gas Argon plasma also achieves a high temperature when compared to other plasma gases. The use of gas containing 90% argon and 10% hydrogen results in significantly hotter plasma than the use of 100%

argon. A typical plasma spray system consists of a power supply, gas source, gun and powder feeding mechanism as shown in Figure 4.4.

During plasma spraying, an electric arc is generated between two water-cooled electrodes in a gun. The arc heats a gas to extremely high temperatures (up to 20,000 °C), partially ionizing it and forming a plasma jet. The gases are accelerated by the tremendous expansion in volume and pass through the jet-shaped anode at a high speed. The powder for the coating is injected into the plasma gas stream, using a carrier gas where they are accelerated to a high speed, melted and impacted onto the substrate with high kinetic energy. Whereas plasma spraying of metallic powders is performed in a vacuum or an inert atmosphere in order to minimize oxidation, plasma spraying of HA and CaP usually takes place under normal atmospheric conditions.

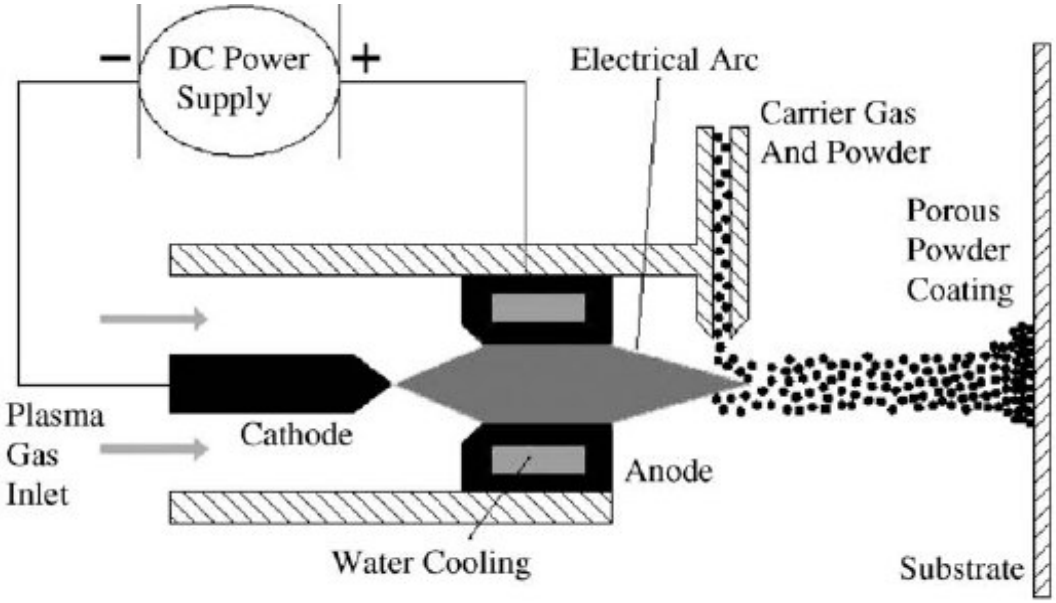

Figure 4.4. A typical plasma spray system.
(Source: Garrette et al. 2005)

Temperature is an important parameter to be considered since the coating material needs to be melted when it contacts the target. This allows the particle to conform to the deformations of the underlying surface maximizing surface contact and minimizing voids. This also leads to higher thermal conductivity. The requirements for the HA coating by plasma spraying are tabulated in Table 4.1. While the thickness of

the coating is not specified in the table, Ca/P ratio is very important as well as the crystallinity and density.

Table4.1. The requirements for the HA coating by plasma spraying
(Source: Garrett et al 2006)

Properties	**Specification**
Thickness	Not specific
Crystallinity	62% minimum
Phase purity	95% minimum
Ca/P molar ratio	1.67-1.76
Density	2.98 g/cm^3
Heavy metals	< 50 ppm
Tensile strength	> 50.8 MPa
Shear strength	> 22 MPa
Abrasion	Not specific

Advantages of plasma spraying include a rapid deposition rate and sufficiently low cost (Suchanek and Yoshimura 2002). However, there are problems associated with plasma-sprayed coatings, including poor adhesion and variation in bond strength between the coatings and metallic substrates (Schreurs et al. 1996) and the extremely high processing temperature. Moreover, plasma spraying cannot provide uniform coatings on the porous metal surface or porous coatings (Thomas et al. 1987; Duchyene et al. 1986). The nature of the substrate plays an important role in the adhesion between plasma-sprayed coatings and metallic substrates (Yang and Ong 2003).

4.3. Biomimetic Method

To provide the basic information allowing the suitability of a material for implanting into the human organism, the artificial materials improved for implants are tested by *in vivo* methods (in live animal organism) and by *in vitro* tests (in simulated

body fluid). In the *in vitro* tests, the material is exposed to the effects of aqueous solutions simulating the inorganic part of blood plasma in the presence or absence of cell cultures, and the interactions of the surface with the solution are examined. The biomimetic process, in the case of metallic materials, generally consists of a chemical treatment in an alkaline or an acid solution. This is followed by the immersion of the material in a simulated body fluid (SBF) which can be considered as a first-stage procedure for the bioactivity assessment of a biocompatible material. The process bases on the heterogeneous nucleation of calcium phosphate from SBF which is supersaturated towards HA at pH = 7.4 and temperature, 37^{o}C. SBF is prepared in accord with the chemical analysis of human body fluid, with ion concentrations nearly equal to those of the inorganic constituents of human blood plasma.

Kokubo et al. in 1991 proposed that the essential requirement for an artificial material to bond to a living bone is the formation of bonelike apatite on its surface when implanted in the living body. Hence, in vivo apatite formation can be reproduced in a SBF with ion concentrations nearly equal to those of human blood plasma (Kokubo 2005). Moreover, in vivo bone bioactivity of a material can be predicted from the apatite formation on its surface in SBF. Since then, in vivo bone bioactivities of various types of materials have been evaluated by apatite formation in SBF. However, the validity of this method has not been systematically assessed.

Cho et al. reported in 1995, a detailed recipe for the preparation of SBF (Lu and Leng 2005). The recipe involved a solution which was richer in Cl^- ion and poorer in HCO_3^- ion than human blood plasma. Later, in 2003, Oyane et al. prepared a revised SBF (r-SBF) in which the concentrations of Cl^- and HCO_3^- were adjusted to the levels of human blood plasma. However, calcium carbonate has a strong tendency to precipitate from this SBF because it is supersaturated with respect to not only apatite, but also calcite. Takadama et al. in 2004, proposed an improved SBF (n-SBF) in which only the Cl^- ion concentration decreased to the level of human blood plasma, leaving the HCO_3^- ion concentration equal to that of the corrected SBF (c-SBF). This improved SBF was compared with the corrected, i.e., conventional, c-SBF with respect to its stability and the reproducibility of apatite formation on synthetic materials. Both SBFs were subjected to round robin testing at ten research institutes. As a result, it was confirmed that the c-SBF does not differ from n-SBF in stability and reproducibility. Through this round robin testing, the method for preparing c-SBF was carefully checked and refined so that the SBF could be easily prepared. This refined recipe for preparing

SBF is tabulated in Table 4.2. Conventional SBF with the refined recipe was proposed to the Technical Committee ISO/TC150 of International Organization for Standardization as a solution for in vitro measurement of apatite-forming ability of implant materials in 2003.

Recently, many researchers have been interested in biomimetic preparation of coatings on the implanted material since this method has shown some advantages in comparison with the traditional methods. It can be applied to any temperature sensitive substrate because it is a low temperature process and can be deposited even on the porous substrates. Since the first formulation proposed by Kokubo et al. for the simulated body fluid calcifying solution (SBF), concentration of individual component in the model solution were also changed and various pre-treatments were applied. Not only bulk samples but also compact samples were tested. An immersion period of the classical biomimetic CaP coating is about 14-28 days. Researchers have been focused on making this process shorter (Ma et al. 2003, Habibovic et al. 2002, Basu et al. 2005, Barrere et al. 2004).

Table 4.2. Nominal ion concentrations of SBF in comparison with those in human blood plasma. (Source: Kokubo and Takadama, 2006)

Ion	**Ion concentration (Mm)**	
	Blood plasma	**SBF**
Na^+	142.0	142.0
K^+	5.0	5.0
Mg^{2+}	1.5	1.5
Ca^{2+}	2.5	2.5
Cl^-	103.0	147.8
HCO_3^-	27.0	4.2
HPO_4^{2-}	1.0	1.0
SO_4^{2-}	0.5	0.5
pH	7.2-7.4	7.4

Several studies have shown that the deposition apatite-like layer could enhance chemical treatment of Ti surface (Vanzillotta et al. 2005). Commercially pure titanium sheets were submitted to three different surface treatments by Vanzillotta et al. in 2005. All samples were etched with HCl/H_2SO_4 solution. A part of each etched sample was further submitted either to anodic oxidation by using an H_3PO_4 solution or to thermal oxidation. All these Ti samples employed behaved similarly after several experiments. After seven days of soaking time into SBF, small globules of the calcium phosphate layer precipitated on the titanium surfaces. The results obtained by using several techniques have shown that surface treatment seems to play a key role in the improvement of in vitro bioactivity of titanium.

Liang et al. in 2002 studied porous titanium compacts which was prepared by a powder metallurgical process with 250 μm in pore size and 40% in porosity in SBF solution. The compacts were alkali-treated using NaOH solution ranging in molarity between 1M and 10M. Following the alkali treatment at 60°C for 24 hours, the compacts were heat-treated at 600°C for one hour. Few samples were only subjected to alkali-treatment and others were subject to both alkali and heat treatment. It was found that alkali and heat treatment resulted in more uniform apatite nucleation at relatively shorter immersion times.

Concentrating the SBF solution is another possibility for shortening the coating process. The pH value of SBF solutions was adjusted to the physiological value of 7.4 by using organic buffers, such as Tris or Hepes, to mimic human plasma. These compounds are not present in human plasma. Barrere et al. have recently developed unique 5xSBF-like solution recipe (with pH values close to 5.8) without any buffering agent. The CO_2 gas was used to decrease the pH of the solution. Furthermore, a midly acid gas leads to increasing solubility of CaP phases. With these improvements in the SBF solution, the deposition of CaP coating on Ti6Al4V become possible in durations less than 24h. In another study, Barrere et al. showed that the formation and attachment of CaP coating in 5xSBF was a function of Mg^{2+} in content.

A novel acidic solution containing 10 times the calcium and phosphate ion concentrations of human blood plasma was reported by Taş and Bhaduri. Such a solution is expected to enhance the kinetics of coating formation even more. Furthermore, except surface treatment step, many intermediate steps were skipped. $NaHCO_3$ was added into the solution to increase the pH to around 6.5. It was reported that the addition of $NaHCO_3$ into the concentrated SBF solution with an ionic strength

of 1137.5 mM allowed the formation of a bonelike apatitic calcium phosphate layer on Ti6Al4V at room temperature within 2–6 h.

Gu et al. 2002 soaked HA/Ti6Al4V composite coating in SBF solution for up to 8 weeks in order to understand the biological behavior of plasma sprayed coating. It was found that that impurity phases such as CaO were dissoluted completely up to7 days and calcium ion concentration increased. Although, the mechanical properties of the coating decreased with soaking, the coatings showed superior mechanical stability than the pure HA coatings.

Xie et al. 2005, investigated the process and mechanism of calcium phosphate nucleation and growth on Ca-implanted titanium surfaces. After 7 days of incubation in SBF, OCP precipitated and HA appeared after 14 days of incubation. Based on the theoretical calculations it was shown that while HA is thermodynamically more stable than OCP while the nucleation rate of OCP is much higher than HA in SBF solution.

CHAPTER 5

MATERIALS AND TESTING METHODS

5.1. Materials and Powder compact preparation

The sintered powder compacts were prepared using atomized spherical Ti6Al4V alloy powders manufactured by Phelly Materials Company. The chemical composition of the powder was tabulated in Table 5.1. and was complied with ASTM 1580-1 standard (Güden et al. 2005). The particle size of the powder ranged between 100 and 200 μm with a mean particle size of 157 μm. The SEM image of the powder is shown in Figure 5.1. As-received powder particles are spherical and have nearly uniform particle size.

Table 5.1. ASTM standard for Ti6Al4V powder and chemical composition of powder (Source: Güden et al. 2005)

Element	Al	V	O	Fe	C	H	N	Cu	Sn	Ti
ASTM F1580-01	5.5~6.75	3.5~4.5	0.2	0.3	0.08	0.015	0.05	0.1	0.1	Balance
Testing Results	6.38	3.93	0.17	0.27	0.013	0.003	0.0072	0.091	<0.01	Balance

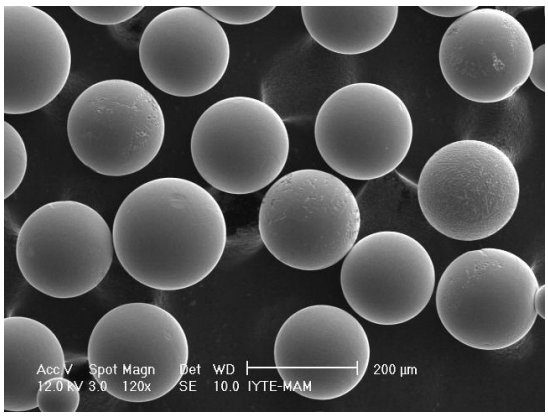

Figure 5.1. SEM view of Ti6Al4V spherical powder.

The powder compacts were prepared using a method which was previously investigated by Güden et al. 2005 In this process the green powder compacts were compacted at room temperature inside a steel die at 400 MPa using a displacement controlled SHIMADZU AG-I universal tension-compression test machine. It was previously shown by Çelik et al. that without using a binder the powder could not be shaped until about the pressures of 400 MPa; therefore, PVA solution 10% by volume was used as the binding material in an amount of 10% by weight. The sintering of the green compacts was performed in a tightly enclosed horizontal tube furnace under high purity (99.998%) Ar atmosphere at 1200°C for 2h (Figure 5.2.). The compacts were heated and cooled with a rate of 5°C per min. In the heating cycle, the compacts were kept at 450°C for 1/2h in order to allow the burning of the binder completely. The compacts were inserted into the furnace at room temperature inside an enclosed Ti box on a graphite plate which prevented the bonding between Ti box and compacts. The average porosity of compact was previously determined by the Archimedes' method to be 37±1%. The open and closed porosities of compacts were calculated by the differences between dry and wet weights (boiling in water). The compact was also determined to contain 100% three-dimensional interconnected pores ranging in size between 16 and 200 μm with a mean pore size of 63 μm, calculated using the linear intercept method on optical micrographs of polished surfaces (Güden et al. 2005).

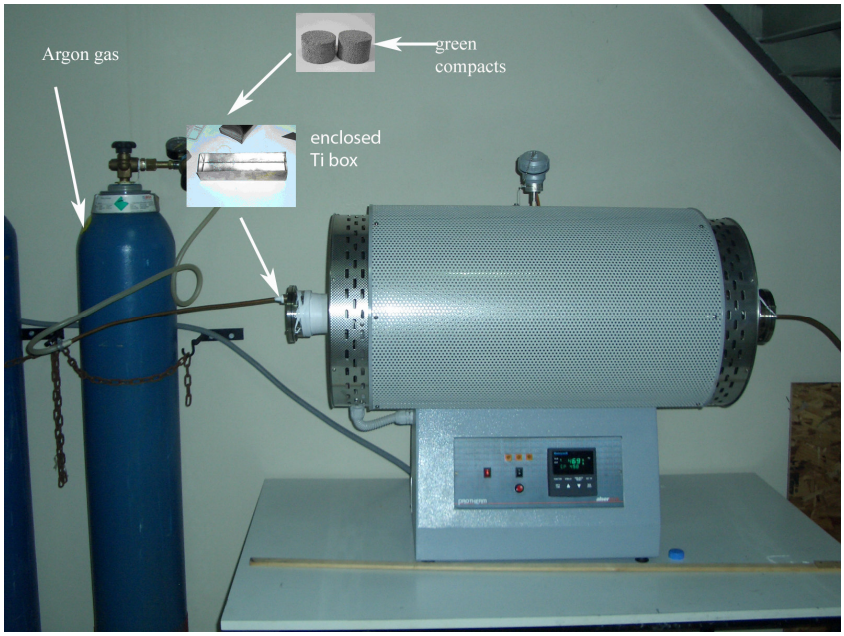

Figure 5.2. The tube furnace used in the sintering of powder compacts.

The optical microscope images of the etched cross-section of a particle before and after sintering process are shown in Figure 5.3.(a) and (b), respectively. As-received powder is composed of needle-like α-phase, referred as acicular alpha (α). Sintering at high temperature above the beta (β)–transition temperature (1050°C) and subsequent slow rate cooling in the furnace under Ar atmosphere however resulted in the development of the so-called Widmanstätten microstructure (Figure 5.3.(b)). In this structure, colonies of β lathes (bcc and rich in V) and α platelets (hcp and rich in Al) formed inside the prior β grains. The percentage and thickness of the β phase were measured previously and found to be 18-20% and 0.2-1 μm, respectively (Güden et al. 2005)

The quasi-static and high strain rate mechanical behavior of the prepared powder compacts were previously determined (Güden et al. 2005). The elastic modulus of the compacts varied between 4 and 6 GPa. The compressive yield and maximum strengths were found to be between 155 and 175 MPa and 229 and 245 MPa, respectively. The compacts showed comparable elastic modulus values with those of human bone (1-17 GPa) and higher compressive strength than that of the cortical bone (110 MPa). These properties potentially make powder compacts suitable materials for hard-tissue implant applications including spinal cages and joint implants.

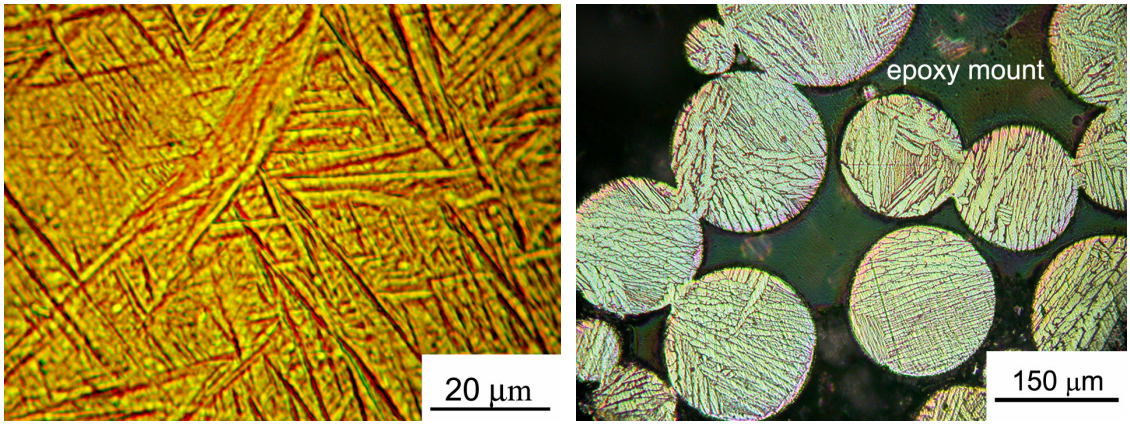

(a) (b)

Figure 5.3. Optical micrographs showing (a) fine needle-like α –phase (acicular alpha) microstructure of the powder and (b) Optical micrograph showing interparticle bonding and Widmanstätten microstructure of sintered compact. (Source Güden et al. 2005)

In the dip-coating process compacts having 16 mm diameter and 10 mm height were used, while in SBF solutions compact heights were reduced to 5 mm (Figure 5.4.). Some compact samples were also alkaline and heat treated before immersing into SBF solution to investigate the effects of pre-treatments on the CaP layer development.

Figure5.4. Cylindrical sintered powder compacts used in the experiments.

5.2. Dip Coating Solutions

In the dip-coating experiments, two different HA powder dip coating solutions were used, as tabulated in Table 5.2. In the first, HA powder was synthesized according to the protocol developed by Maviş and Taş 2000. A 3 ml aliquot of 0.1 g/l methyl cellulose solution (99% pure, Sigma, St. Louis, MO), acting as dispersant, was mixed with 1440 ml of deionized water. Thereafter, 0.152 mol of $Ca(NO_3)_2.4H_2O$ (99% pure, Merck, Darmstadt, Germany) and 0.090 mol of $(NH_4)2HPO_4$ (99% pure, Merck) were mixed with the solution. This mixing step resulted in the formation of an opaque solution mixture. Finally, 115 ml of 28-30 vol% NH_4OH (99% pure, Performans, Turkey) was added to the final opaque solution. Then the solution was heated to a temperature between 60 and 70°C on a hot plate for 90 min. The heating process resulted in the formation of HA precipitates with an average particle size of 200 nm.

The precipitates were vacuum filtered using Buchner funnel and recovered in the form of cream. The HA precipitate cream was dried in an oven at 90°C for 6 h.

Table5.2. Dip coated powder compact samples

Compact	Powder in Dip-Coating
1	Commercial HA
2	Milled Commercial HA
3	Sol-derived HA

The dip coating solution was prepared according to the procedure shown in Figure 5.5. The composition of the dip-coating solution in wt% is listed in Table 5.3. Poly(ethylene glycol) (PEG) (99.5% pure, molecular weight of 15 000, Merck), gelatin (hereafter called GEL) (99.9% pure, Merck, Darmstadt, Germany), and glycerol (hereafter called GLY) (98.5% pure, Performans) were blended with the mixture of ethanol (hereafter called EtOH) (99.9% pure) and water-HA suspension.

Table 5.3. Development of HA Dip-Coating-Solution Recipes (Composition (wt%)) (Source: Maviş and Taş 2000)

Reagent	HA	H_2O	EtOH	PEG	GEL	GLY
Composition (wt%)	7.3	13.8	66.2	2.2	0.3	10.2

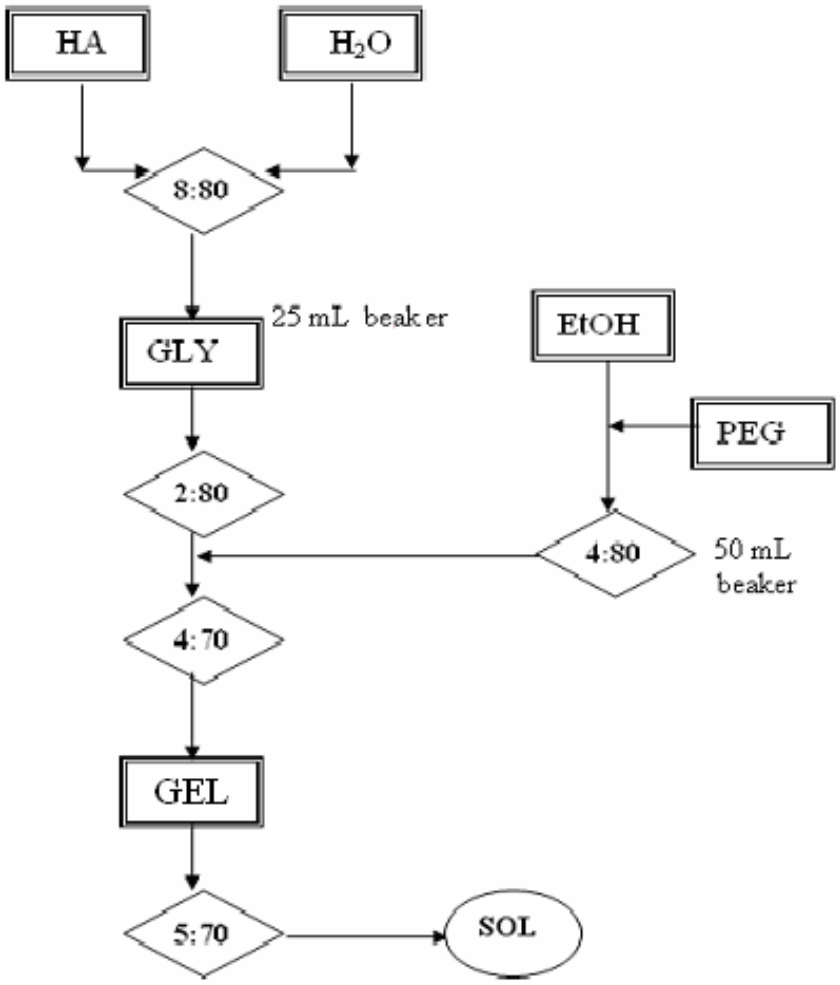

Figure 5.5. Process flowchart of the preparation of the HA dip-coating solution. (Source: Maviş and Taş 2000)

In the second dip coating solution, commercial HA powder, (Merck, Darmstadt, Germany), were used. As-received HA powder was either directly used to prepare the coating solution or ball-milled to form a finer and homogeneous particle size distribution before preparation of the solution. HA powder ball milling was conducted in a planetary ball mill, FRITSCH Planetary Mono Mill Pulverisette 6. The ball milling was performed inside a Tungsten carbide jar of 250 ml using 30 tungsten Carbide balls of 10 mm in diameter and 200g of powder in deionized water. The following milling parameters were applied: eccentric revolver rate: 260 rpm and milling duration: 2 hours. During milling, at every 15 minutes, the jar was taken out and the partially milled powder was mixed with a spatula to remove the powder adhesion to the jar walls. The dip-coating solution was prepared by mixing milled and unmilled HA powders with deionized water. Initially, dip-coating solution was prepared using 5 wt% HA powder.

These experiments showed that the coating rate was relatively low. Therefore, the wt% of HA powder was increased to 14.7%. The pH of the coating solution was measured to be 10. The suspension was again ball milled with zirconia balls in a glass jar for 30 minutes for further deflocculation.

Dip-coating of the compacts using sol-derived and commercial as-received and milled HA powders were performed using NEMA dip-coater device (Figure 5.6.). Before dip coating, the compacts were washed with distilled water. The rates of the dipping and removing of the compact were kept constant, 100 mm/min. Dip-coating was performed at different soaking times until the surfaces of the compacts were completely coated with HA. Following the coating process, the compacts were heated in a tightly enclosed horizontal tube furnace under high purity (99.98%) Ar atmosphere at a temperature of 840° ± 3°C (2 h of peak soaking time), with a heating and cooling rate of 2°C/min.

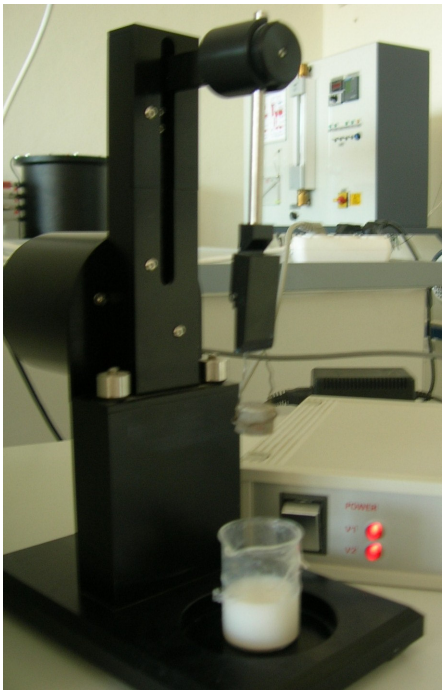

Figure 5.6. A view of dip-coater used in the coating experiments.

5.3. SBF Solutions

Three different SBF solutions, 1, 5 and 10x were prepared and used in the coating of compacts and alkali and heat treated compacts, as tabulated in Table 5.4. The

following chemicals were used in the preparation of SBF solutions: Merck-grades NaCl (99.5%), $NaHCO_3$ (99.5%), KCl (99.0%), Na_2HPO_4 (99.5%), $(MgCl_2).6H_2O$ (99.0%), Na_2SO_4, $(CH_2OH)_3CNH_2$ (99.5%), $CaCl_2.2H_2O$ (99.0%) and HCl (37 vol%, Carlo-Erba, Rome, Italy).

Table 5.4. SBF coated compact samples

Compact	Alkali and heat Treatment	SBF
1	-	1xSBF
2	+	1xSBF
3	-	5xSBF
4	+	5xSBF
5	-	10xSBF
6	+	10xSBF

The composition of 1XSBF is tabulated in Table 5.5. Appropriate amounts of reagents in accord with Table 5.5. were sequentially added and completely dissolved in 800 ml of de-ionized water. A total of 45-50 ml of 1 M HCl solution was then added to adjust the pH adjustments during the preparation of 1 L of SBF solutions. A 25 ml aliquot of this acid solution was added just before the addition of the sixth reagents, viz., $(CaCl_2).2H_2O$. Otherwise, the solution would display slight turbidity. The remaining part of the HCl solution was used during subsequent titration. Following the addition of the eighth reagent (*tris*(hydroxymethyl) aminomethane), the solution temperature was raised from ambient to 37 ^oC. This solution was then titrated with 1 M HCl to a pH of 7.4 at 37 ^oC. During titration process, the solution was also continuously diluted with consecutive additions of de-ionized water to make the final volume equal to 1 L 5xSBF solution with ion concentration of 5 times those of 1XSBF was prepared using the same reagents grade. The chemicals were dissolved in de-ionized water and the solution pH was maintained at 6 with the addition of 1M HCl.

Table 5.5.The composition of 1XSBF

(Source: Kokubo 1998)

Order	Reagent	Amount
1	NaCl	6.547g
2	$NaHCO_3$	2.268g
3	KCl	0.372g
4	Na_2HPO_4	0.142g
5	$MgCl_2.6H_2O$	0.305g
6	1M HCl	40ml
7	$CaCl_2.2H_2O$	0.368g
8	Na_2SO_4	0.071g
9	Tris	6.0570g

The composition of 2 l 10xSBF solution is given in Table 5.6. The chemicals given in Table 5.6. were added, in the order written, to 1900 ml of de-ionized water in a glass beaker of 3.5 L capacity. Before the addition of the next chemical, the previous one was completely dissolved in water. After all the reagents were dissolved at room temperature, the solution was made up to 2 L by adding the proper amount of water.

Table 5.6. The composition of 10XSBF

(Source: Tas and Bhaduri 2004)

Order	Reagent	Amount (g)	Concentration (mM)
1	NaCl	116.8860	1000
2	KCl	0.7456	5
3	$CaCl_2.2H_2O$	7.3508	25
4	$MgCl_2.6H_2O$	2.0330	5
5	NaH_2PO_4	2.3996	10

This stable stock solution of pH value of 4.20–4.30 was stored at room temperature in a capped glass bottle. Just prior to coating a Ti6Al4V powder compact , a 200ml portion of this stock solution was placed into a 250ml capacity shoot bottle, and a proper amount of $NaHCO_3$ powder was added to raise the hydrogen carbonate ion

(HCO_3^-) concentration to 10 mM, under vigorous stirring. Following the rapid dissolution of the $NaHCO_3$, the pH of the clear solution rose to 5.80 at room temperature. This solution (with an ionic strength of 1137.5 mM) was then transferred to a 250-ml capacity shoot bottle, which contained the Ti6Al4V compact inside, tightly capped and kept at room temperature for 2–6 h during coating.

All compact samples before being subjected to alkali-treatment and insertion into SBF solution were cleaned ultrasonically in acetone, ethanol and distilled water for 20 min, respectively. Compact samples to be alkali-treated were immersed in 10.0 M NaOH aqueous solution at 60°C for 24 h. The samples were then washed with distilled water and dried in air for 24 h. Finally the samples were heated in an electrical furnace at a heating rate of 5°C/min at 600°C for 1 h.

Cleaned compact samples with and without alkali-treatment were soaked in 30 ml SBF at 37 °C. SBF solution was refreshed every 2 days. After soaking for various periods, the samples were removed from the solution, gently rinsed with distilled water and dried at room temperature. Few of the compact samples in 5xSBF solution were also dried at 110 °C.

5.4 Microstructural and Chemical Characterization

The morphological and elemental analysis of the coating was studied using a Philips XL30-SFEG scanning electron microscope (SEM) with an Energy Dispersive X-ray (EDX) analyzer.

The phase composition of the deposited coatings on the substrates were analysed with a Phillips X-Pert Pro diffractometer. The XRD measurement was performed using a Cu K_α radiation with a wavelength of 0.154 nm and operated at the condition of 40 kVand 30 mA. The XRD patterns were recorded at a scan rate of 4°/min and a 2θ range of 20–70°.

FTIR analysis was conducted in a Perkin Elmer FTIR System Spectrum BX Fourier Transform Infrared Spectrometer. In the preparation of samples for the FTIR analysis, the powder scratched from the surface of the SBF-incubated plates was mixed with KBr powder. The mixture was then pressed to obtain disc specimens. The FTIR spectra were recorded in a spectral range of 4000–400 cm^{-1}.

CHAPTER 6

RESULTS

6.1. Dip-coating Using Commercial HA Powder

Figure 6.1. shows SEM micrograph of the commercially available HA powder which was used in this study for the coating of Ti6Al4V powder compacts. The HA particles seen in the same figure have angular shape and the average length of the particles in the long-axis is measured 200 nm on the average. Two types of dip coating solutions were used in the coating experiments: as-received and ball-milled powder. The results of the coating experiments using these powders will be sequentially given below.

Figure 6.2. shows the surface SEM micrograph of a coated compact sample after 1-minute soaking in the nano size HA dip-coating powder solution. The spherical Ti6Al4V particles seen in this figure are coated with a thin layer of HA. Figure 6.3. is the magnified view of Ti6Al4V particles shown in Figure 6.2. Complete coating of the particles with HA is clearly seen in this figure. The initial open porosities remain to be open after coating as marked with white arrows in Figure 6.3. The coating layer is relatively thin and macroscopically homogenous. The coating is; however, thicker at the particles sintering necks as marked with arrows in Figure 6.3. Figure 6.4 shows a partially coated Ti6Al4V particle; the coating starts from the particle sintering neck and proceeds through the uncoated regions of Ti6Al4V particle. The sintering necks are presumably acting as easy HA coating regions. The thermal etch marks on the surface of Ti6Al4V particle are also seen in Figure 6.4. The early HA coating of etch marks in the partially coated region is also noticed Figure 6.4. Relatively long and wide cracks are also seen on the relatively thick coating layer at the sintering neck (Figure 6.4.).

It is found that when the soaking time of the compact in the as-received powder dip-coating solution increases from 1 to 3 minutes, the initial open porosities are almost closed with a continuous HA layer as seen in Figure 6.5. The darker area on the top of each sphere seen in Figure 6.5. basically shows the uncoated region. While increasing the soaking time to 5 minutes increases the coating thickness further, the pores are completely closed and the extent of coating cracking increases (Figure 6.6.). Coating

cracking is particularly more pronounced in the coating on initial open pores as shown in Figure 6.6. The EDX analysis of a coated sample, from an area of 2 mm x 2 mm, shows that the molar ratio of Ca/P is nearly 1.67 (Figure 6.7.). This ratio is the same with that of HA in human bone.

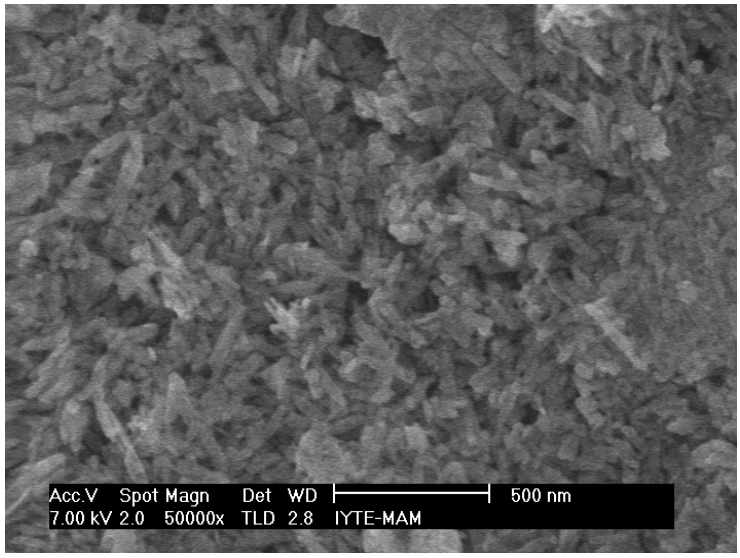

Figure 6.1. SEM micrograph of as-received HA powder.

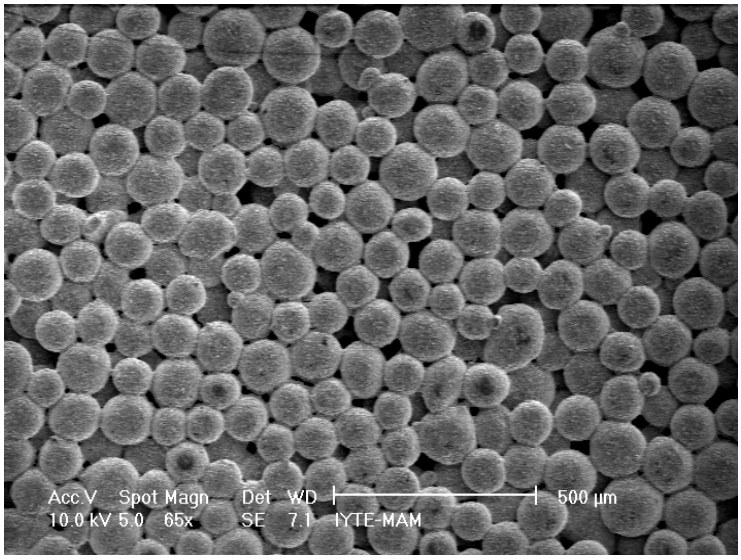

Figure 6.2. The surface SEM micrograph of a dip-coated compact sample after 1-minute soaking.

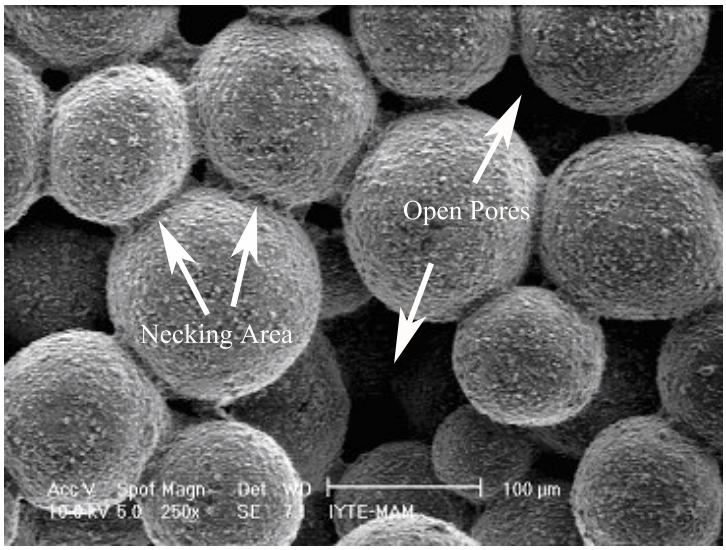

Figure 6.3. SEM magnified view of Ti6Al4V particles seen in Figure 6.2.

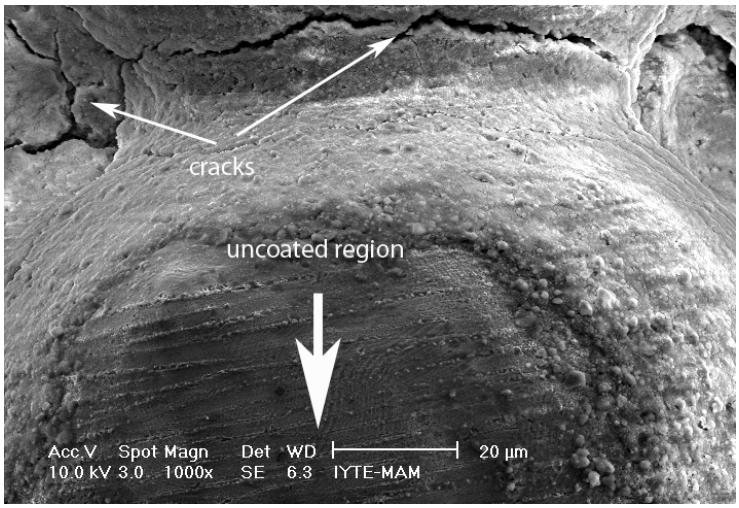

Figure 6.4. SEM micrograph showing HA coating in a region near a particle sintering -neck (1-minute soaking).

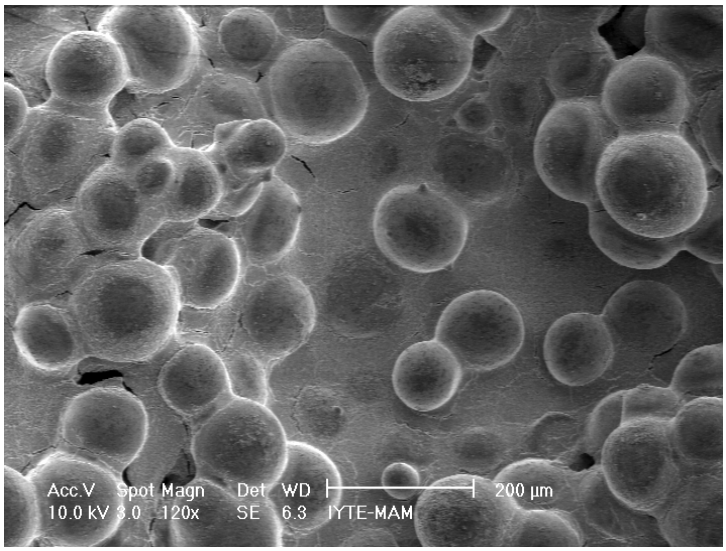

Figure 6.5. The surface SEM micrograph of dip-coated compact sample after 3-minute soaking.

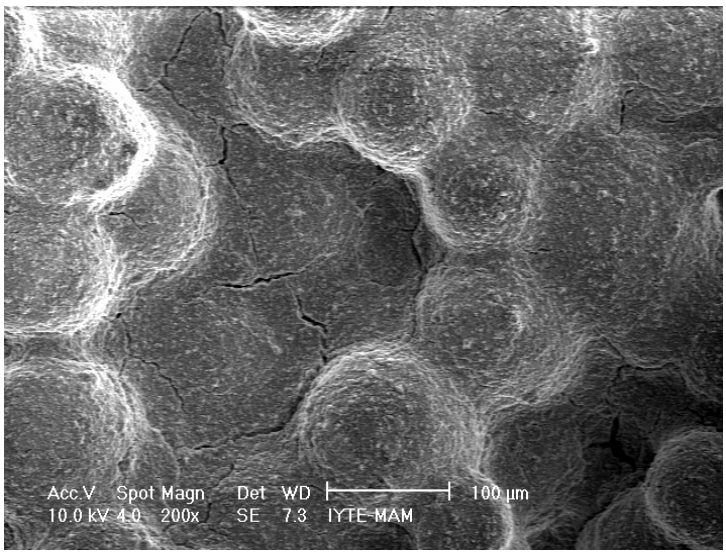

Figure 6.6. The surface SEM micrograph of dip-coated compact sample after 5-minute soaking.

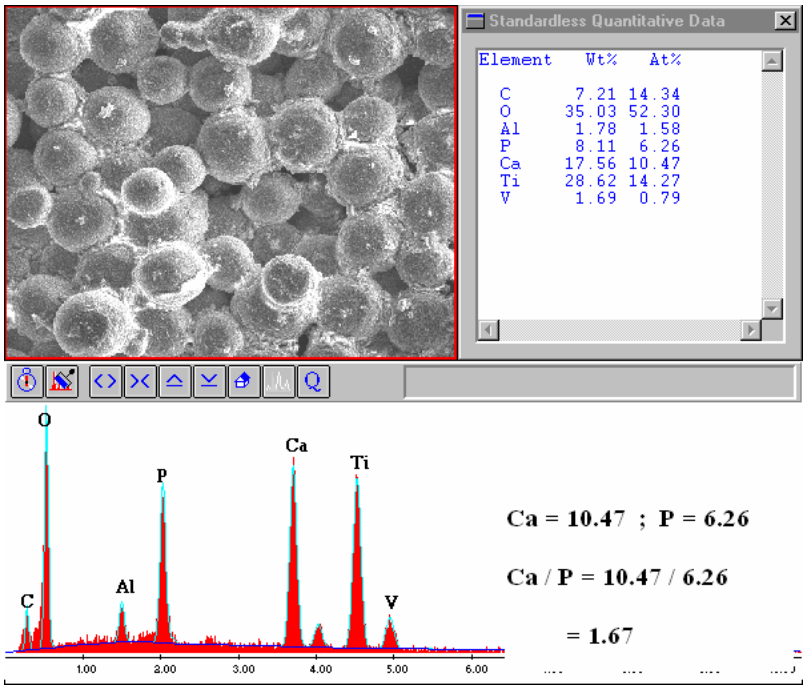

Figure 6.7. EDX analysis of a coated compact sample (5-minute soaking).

Coating experiments were continued with the use of milled as-received HA powder in the dip-coating solution. The SEM micrograph of milled HA powders is shown in Figure 6.8. The milling reduced the particle size from 200 nm to 50-75 nm on the average. It is also noted in Figure 6.1. and Figure 6.8. that the original angular particles were reverted into more spherical ones after milling.

Figure 6.9. shows SEM view of HA coating on a Ti6Al4V compact sample after 1-minute soaking using the milled powder dip-coating solution. It is noted in Figure 6.9. that all particles surfaces are almost completely coated after 1 minute soaking into the solution. In addition, the initial small open pores between Ti4Al4V particles remain to be open after the coating as depicted in Figure 6.10. SEM view of coated sintering necks seen in Figure 6.11. further suggests that the coating is continuous and relatively homogeneous. The small dark regions seen on the top of Ti6Al4V particle in the mid of the picture of Figure 6.11. are the regions that are not coated. The extent of these uncoated regions are however reduced with the use of the milled HA powders. Compared to the compacts coated with unmilled powder using the same coating parameters, the compacts coated with the milled HA powder solution

show; (a) a thinner coating layer at the sintering necks and (b) hence relatively more homogeneous coating layer thicknesses (Figure 6.12.).

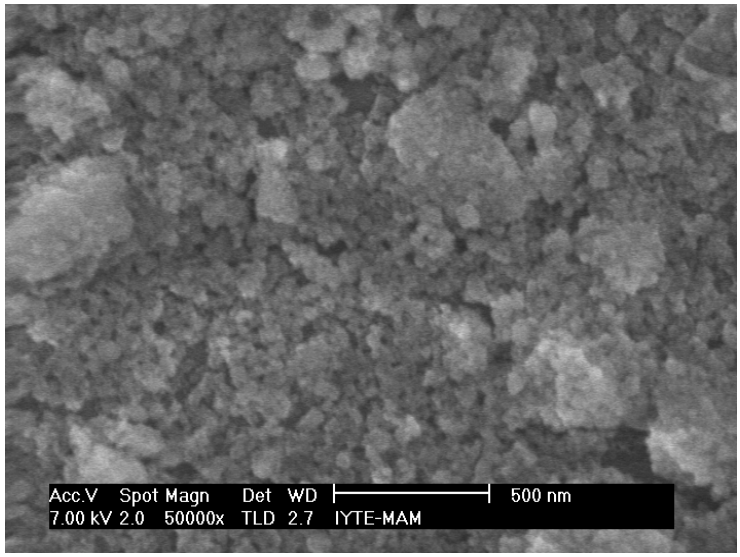

Figure 6.8. SEM micrograph of milled HA powders.

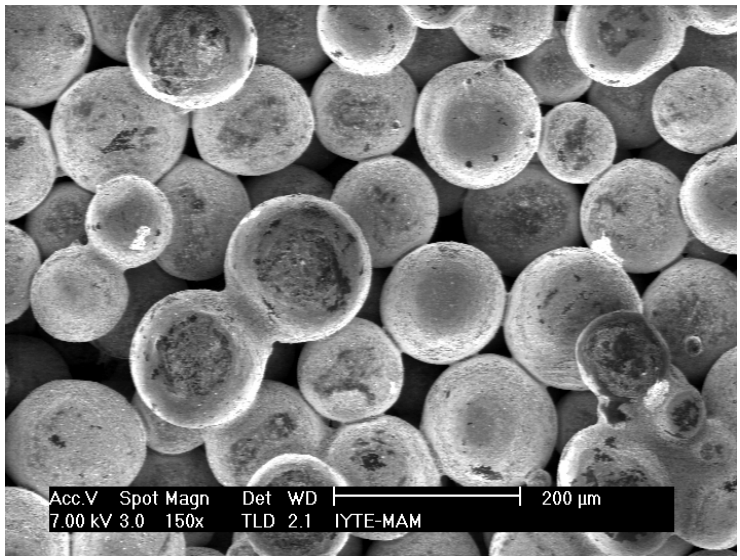

Figure 6.9. The surface SEM micrograph of milled HA powder coated compact sample after 1-minute soaking.

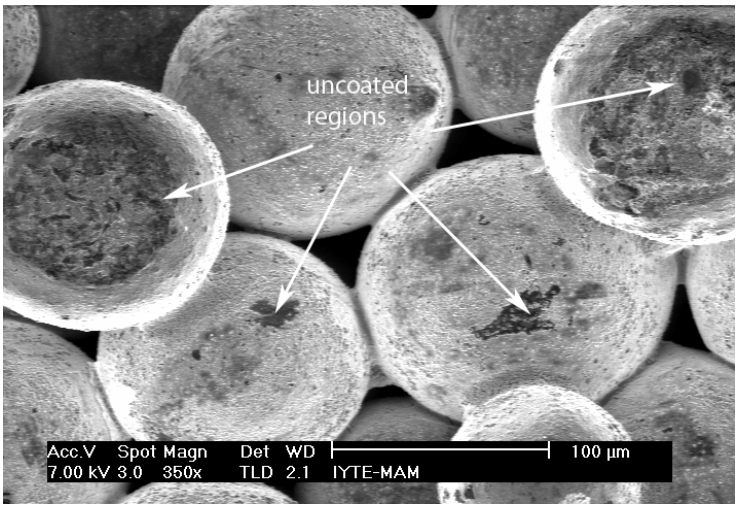

Figure 6.10. SEM micrograph showing open pores between the particles after 1-minute soaking.

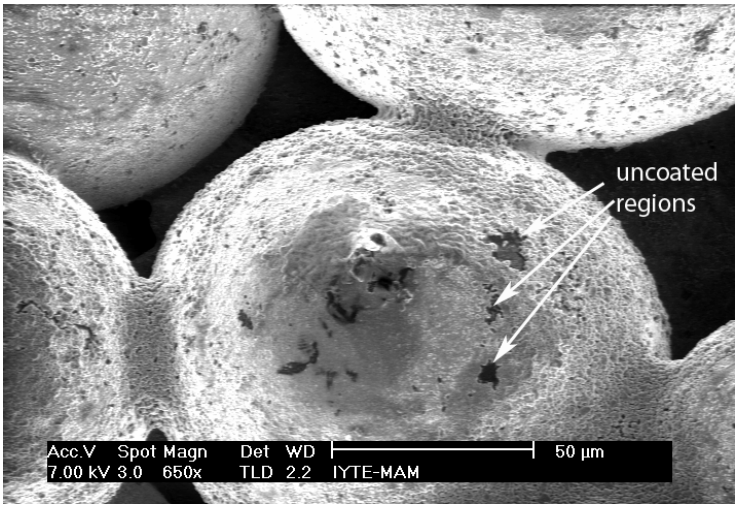

Figure 6.11. SEM micrograph showing coating at sintering necks between particles after 1-minute soaking.

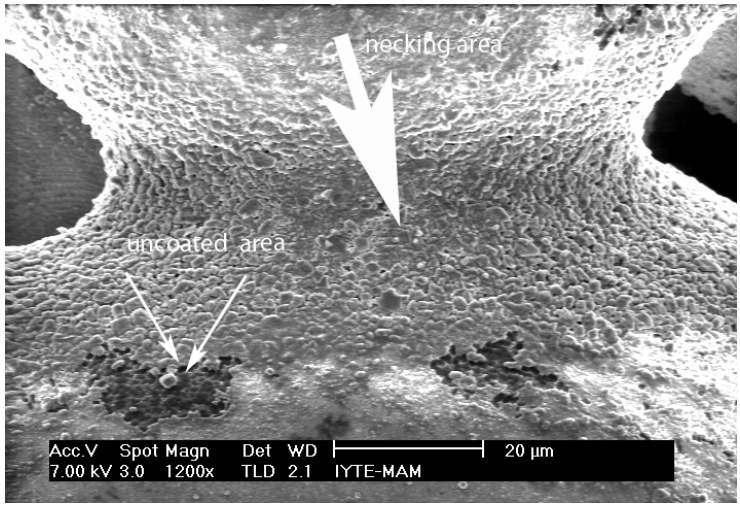

Figure 6.12. SEM micrograph showing coating at a sintering neck between two particles after 1-minute soaking.

Figure 6.13. shows SEM view of HA coating on a Ti6Al4V compact sample after 3-minute soaking using milled powder dip-coating solution. As seen in this figure in addition to increasing thickness of the coating, the pores smaller than 200 micrometers are completely closed with HA when the soaking time increases to 3 minutes. Cracks are seen on the coating layer particularly at the sintering necks (Figure 6.14.). Further increase in soaking time, 5 minutes, increases the thickness of the HA coating layer and fills completely the pores with HA as shown in Figure 6.15. In these samples, the coating cracking extends through the HA coating layer on the originally open pores in addition to the cracking of the coating layer at sintering necks (Figure 6.15.). Similar to the unmilled powder coated compact samples, the compact samples coated with milled HA powder show a Ca/P molar ratios of 1.67 as shown in Figure 6.16.

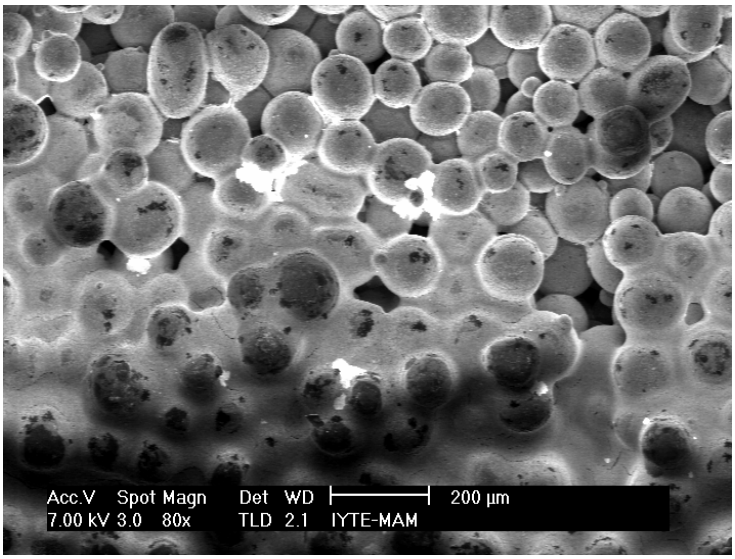

Figure 6.13. The surface SEM micrograph of milled HA powder coated compact sample after 3-minute soaking.

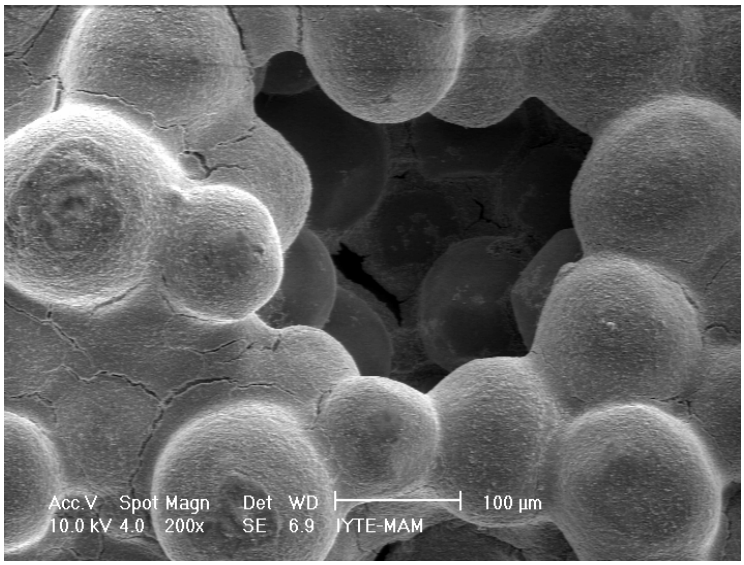

Figure 6.14. SEM micrograph showing closed pores and a large open pore between particles and the cracks on the coating layer after 3-minute soaking.

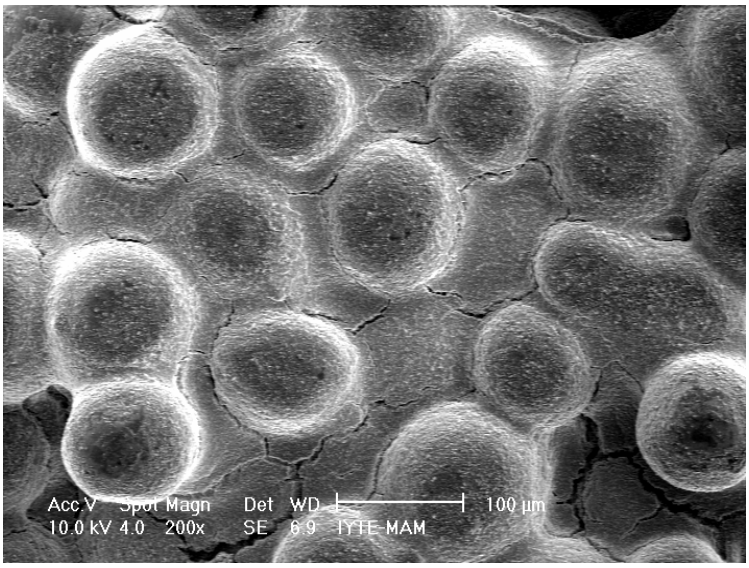

Figure 6.15. The surface SEM micrograph of milled HA powder coated compact sample after 5-minute soaking, showing long and wide cracks on the coating layer.

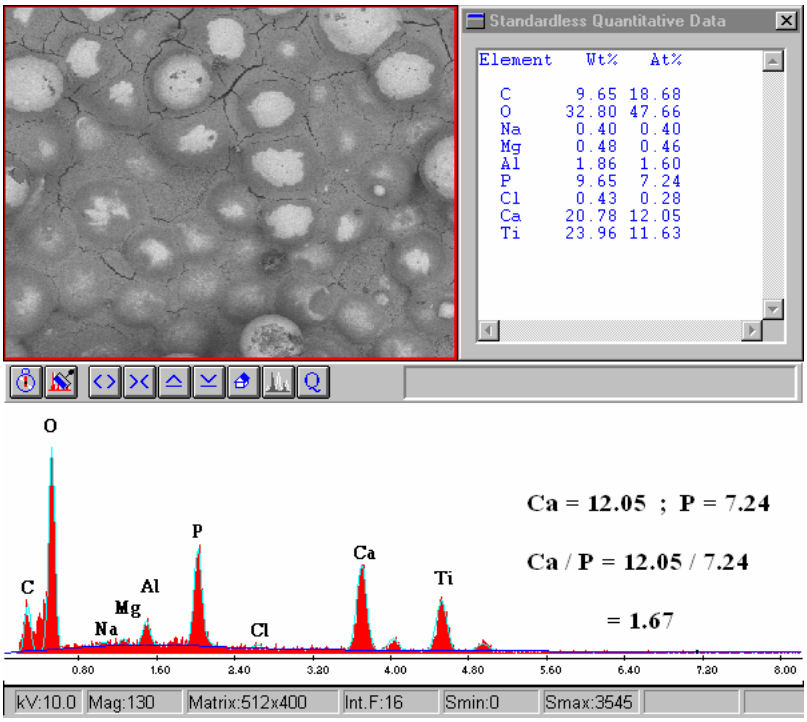

Figure 6.16. EDX analysis of milled powder coated compact sample (5-minute soaking).

Powder agglomeration was observed in all samples surfaces coated with and without milled powders (Figure 6.17.). It was also observed through extensive SEM

observations that compact samples coated with unmilled powder showed relatively more powder agglomeration as compared with compacts coated with milled powder. Figure 6.18.(a) and (b) show, for comparison, a single Ti6Al4V particle coated with milled and unmilled HA powder, respectively. The use of the milled powder results in (a) smoother coating surface, (b) relatively thin coating layer and (c) more homogenous HA coating of the particles of the sintered powder compacts.

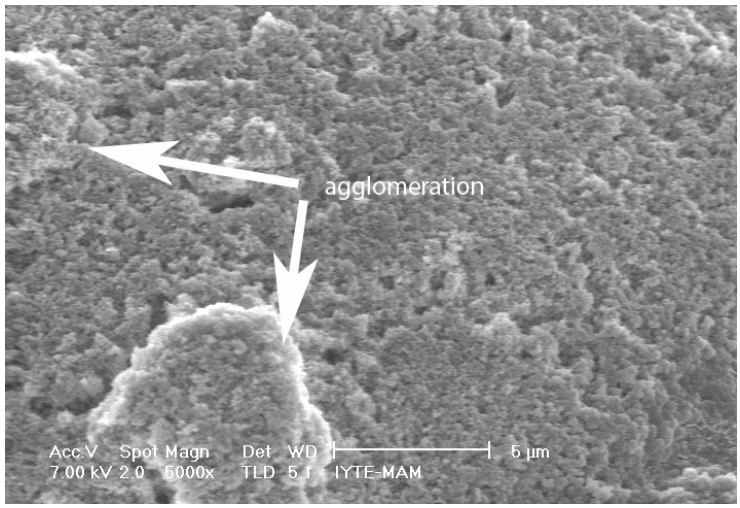

Figure 6.17. SEM micrograph showing powder agglomeration in the coating layer of the compacts coated with milled powder.

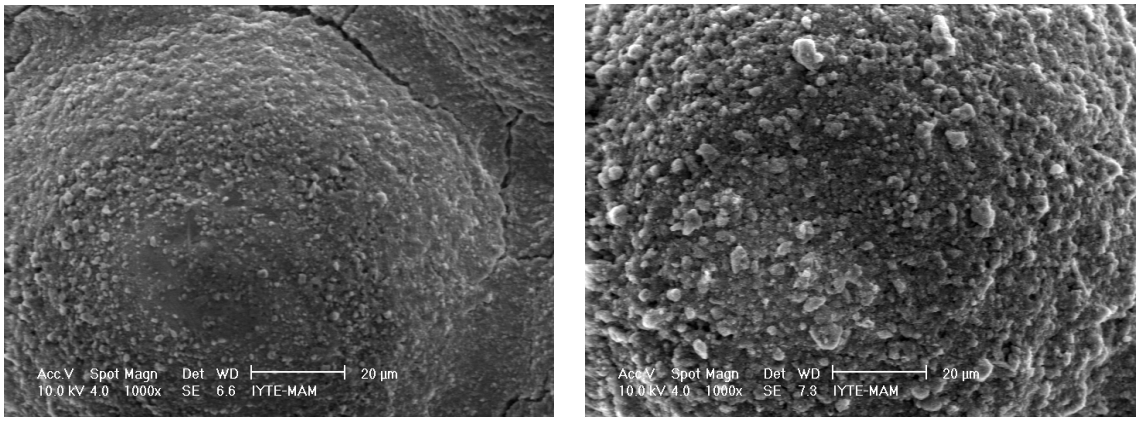

(a) (b)

Figure 6.18. SEM micrographs showing HA coated single Ti6Al4V particle surfaces using (a) milled and (b) unmilled powders after 5-minute soaking time.

XRD results of unmilled and milled powder coated compact samples (5-minute soaking) are shown in Figure 6.19. The higher intensities of Ti6Al4V substrate in the compacts coated with milled powder may be proving the formation of a thinner HA coating layer. FTIR analyses of unmilled and milled powder sample are shown in Figure 6.20. Phosphate peaks can be seen at 1080 cm^{-1}. The phosphate peaks at 1080 are due to phosphate stretching. The strong peak at 1420 represented CO_3^{2-}. The broad peak at 3500 cm^{-1} corresponds to the absorbed water. Carbonate bands are observed at 870 cm^{-1} and 1420 cm^{-1}. HA FTIR spectra given here are also very similar to those obtained previously (Gross et al. 1998, Gerber et al. 2000)

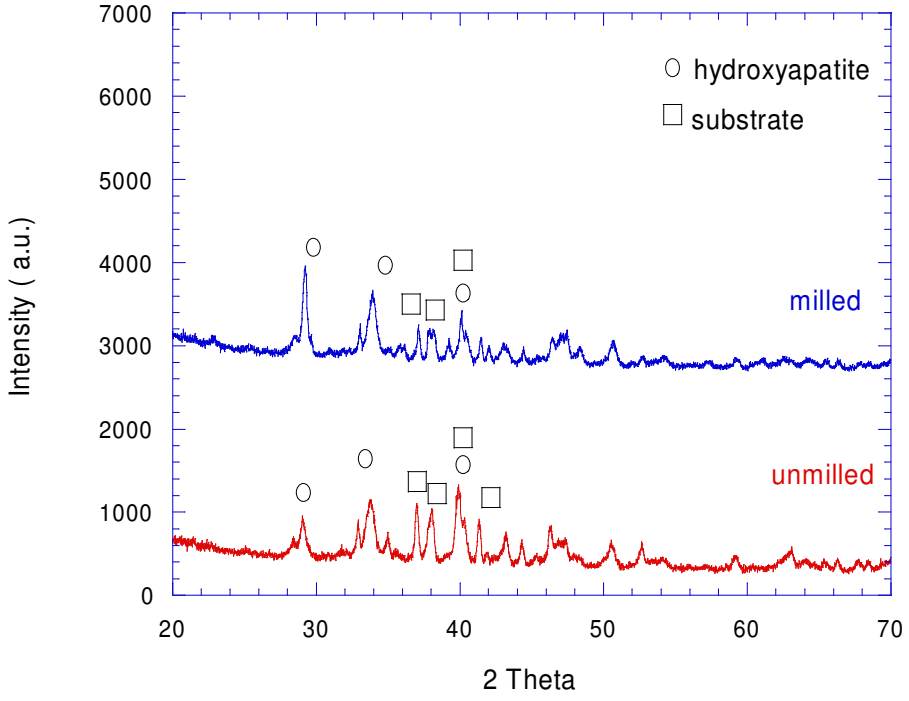

Figure 6.19. XRD patterns of unmilled and milled powder coated compact samples (5-minute soaking).

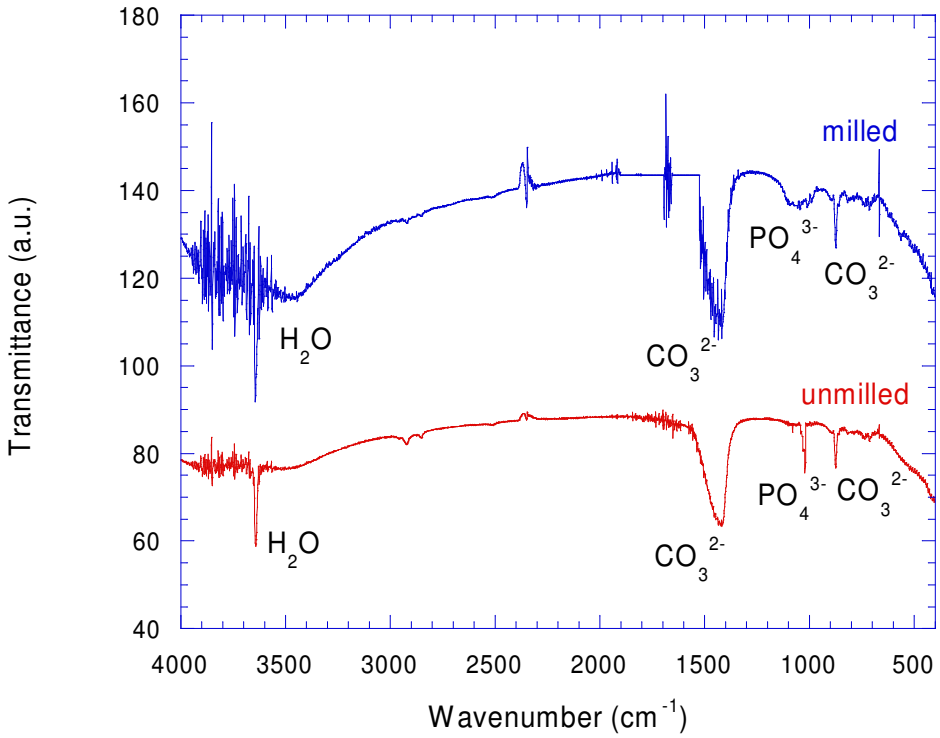

Figure 6.20. FTIR spectra of unmilled and milled powder coated compact samples (5-minute soaking).

6.2. Coating Using Sol-Derived HA Powder

The synthesized HA precursor powder used in this study for dip-coating solution yielded stable (against sedimentation) dip-coating solution. This was also noted in a previous study (Gan et al. 2004). Drying at 90°C results in an HA powder which is not totally amorphous as shown in Figure 6.21. However, heating at higher temperatures in an air atmosphere for 6 h improves the crystallinity of the HA powder (Figure 6.21). The powder is a single-phase HA even at relatively high temperatures, 1200°C, as seen in Figure 6.21.

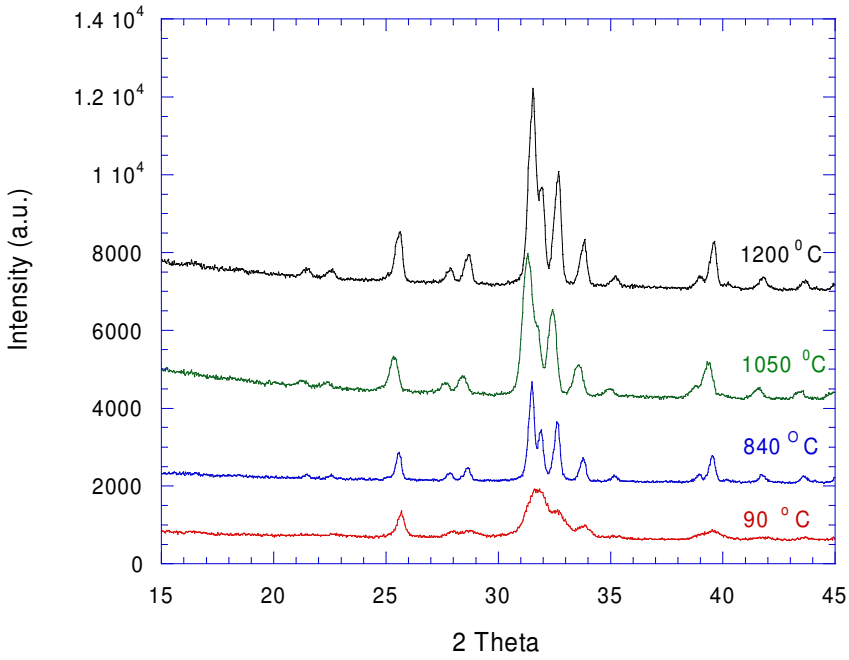

Figure 6.21. XRD pattern of the precipitated HA powder as function of heat treatment temperature.

The coating of powder compacts with sol-derived powder starts as early as 1-minute soaking of the compact into the dip-coating solution as shown in Figure 6.22. Similar to the commercial HA powder coating, the coating starts to form at particles sintering necks as seen in Figure 6.22. It is also noted in the same micrograph that few particles are not coated completely with HA. Cracks are seen in the coating at particles sintering necks. As the soaking is increased to 2-minute, Figure 6.23., more particles are coated and the extent of cracking of the coating layer at the sintering necks decreases. Note that the surfaces of Ti6Al4V particles are not still completely coated after 2- minute soaking, as seen darker regions on the particles surfaces in Figure 6.23. After 3-minute soaking, the surfaces of the particles are coated completely, expect small regions on the particles on the top of the particles in Figure 6.24. It is also seen in Figures 6.22., 6.23. and 6.24. that the original open pores are retained after 3-minute soaking. Figure 6.25. and accompanying extensive microscopic observations of the sintering necks have revealed that the coating thickness differences between the coating at the particle sintering necks and particle surfaces decreased and the extent of coating cracks at the sintering necks decreased as the soaking time increased to 3 minutes. Although macroscopically the coating layer was found to be homogeneous at 3-minute

soaking, powder agglomerations were observed on the particle surfaces. Such powder agglomerations are clearly seen in Figure 6.26. Note that HA coating in Figure 6.26. is porous as opposed to HA coating found in the compacts coated with unmilled HA powder.

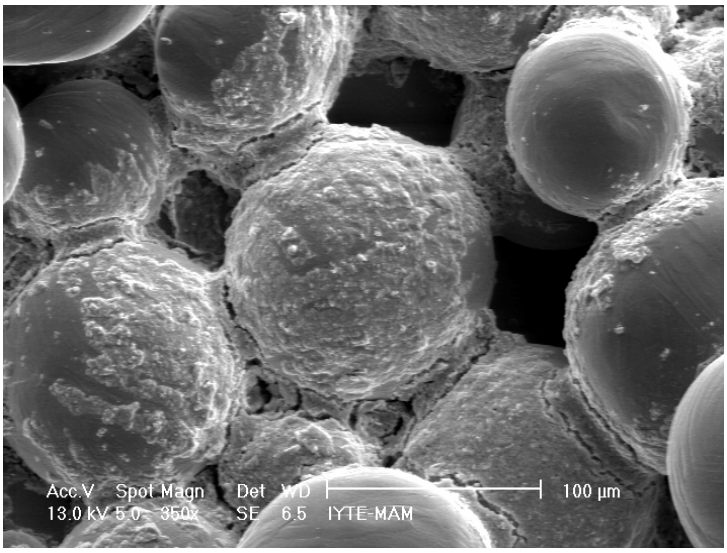

Figure 6.22. The surface SEM micrograph of sol-derived HA powder coated compact sample after 1-minute soaking.

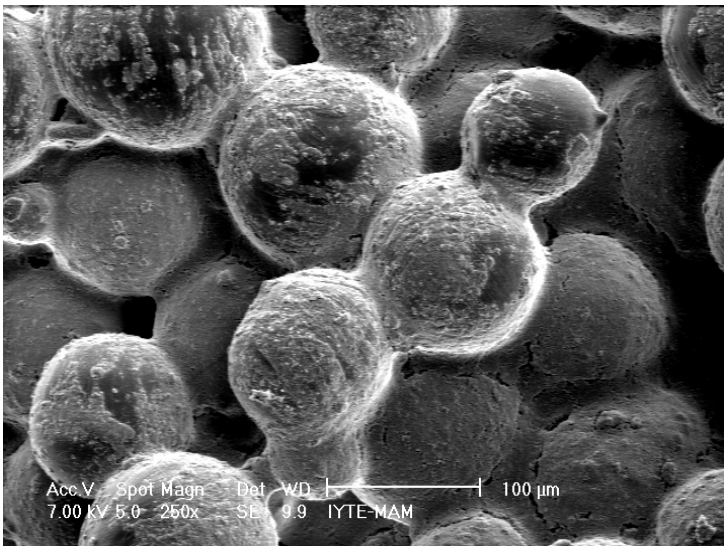

Figure 6.23. The surface SEM micrograph of sol-derived HA powder coated compact sample after 2-minute soaking.

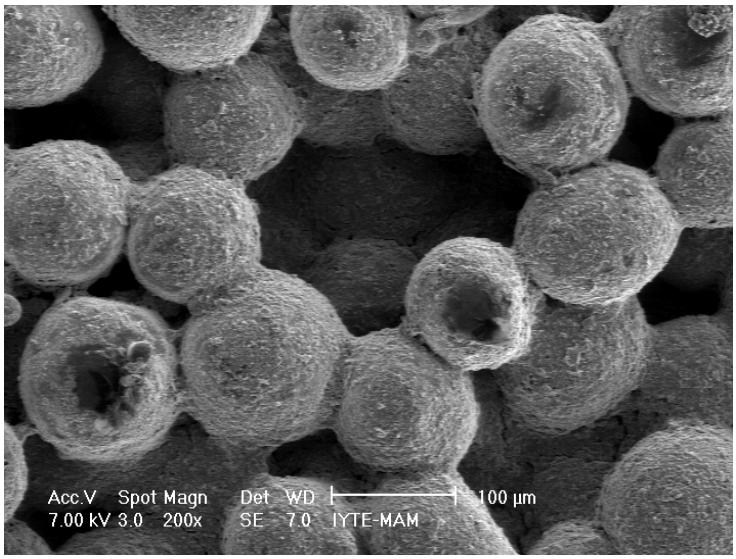

Figure 6.24. The surface SEM micrograph of sol-derived HA powder coated compact sample after 3-minute soaking.

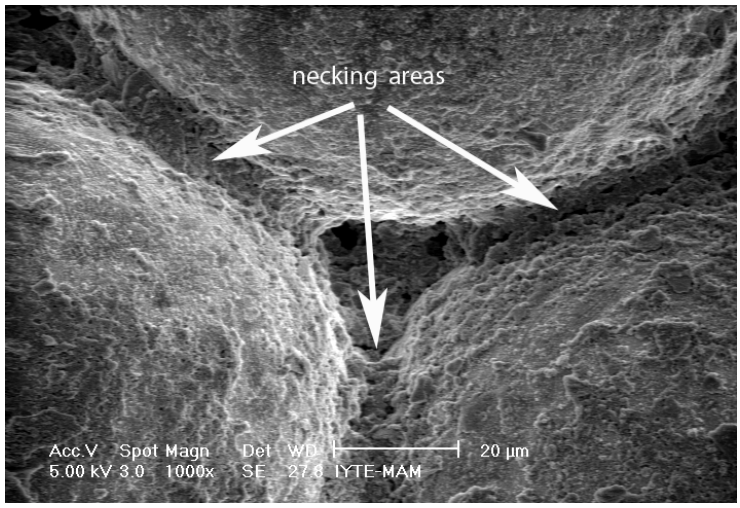

Figure 6.25. SEM micrograph of sol-derived HA powder coated compact sample showing HA coating at particle sintering necks after 3-minute soaking.

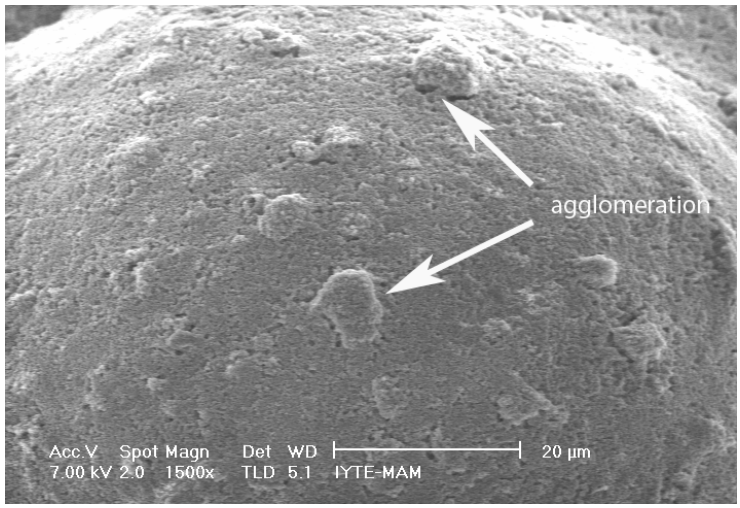

Figure 6.26. The surface SEM micrograph of coated Ti6Al4V (3-minute soaking) showing HA powder agglomerates.

At 4-minute soaking the coating thicknesses of Ti6Al4V particles increase further, originally open pores start to be filled with HA and the porous coating layer becomes more pronounced as seen in Figure 6.27. The pores are completely closed when the soaking time increases to 5-minute as depicted in Figure 6.28. Few large cracks are also seen in the coating located near the sintering necks (Figure 6.28.). It is also noted in Figure 6.28. and 6.29. the coating layer turns into a relatively dense layer at 5-minutte soaking. Finally, the coated compacts are distinguished from uncoated compacts in that the color of the coated compact becomes whiter after 5-minute soaking (Figure 6.30.).

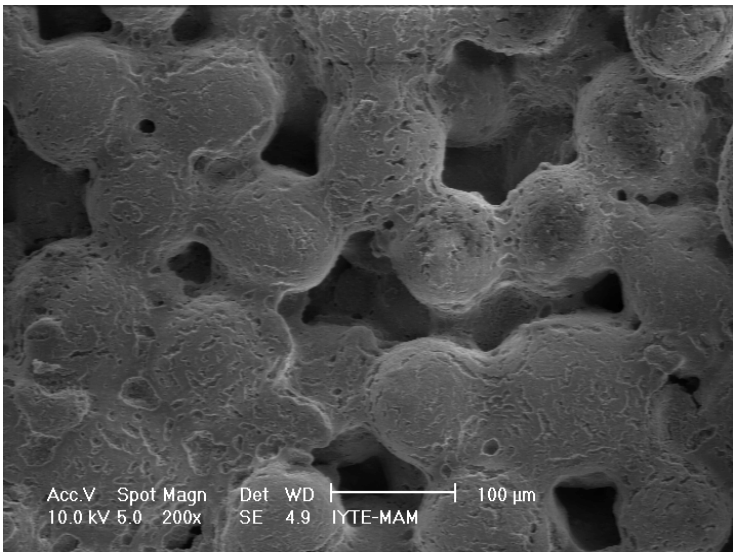

Figure 6.27. The surface SEM micrograph of sol-derived HA powder coated compact sample after 4-minute soaking.

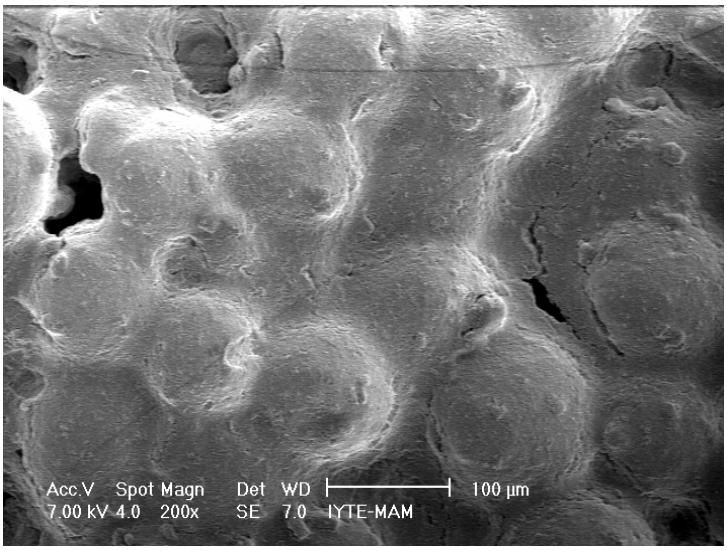

Figure 6.28. The surface SEM micrograph of sol-derived HA powder coated compact sample after 5-minute soaking.

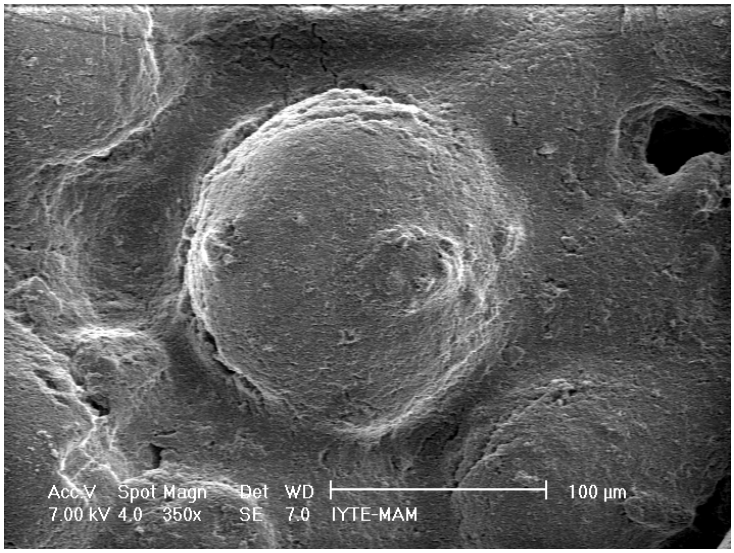

Figure 6.29. The surface SEM micrograph of sol-derived HA powder coated compact sample after 5-minute soaking showing coating cracking at particles sintering necks.

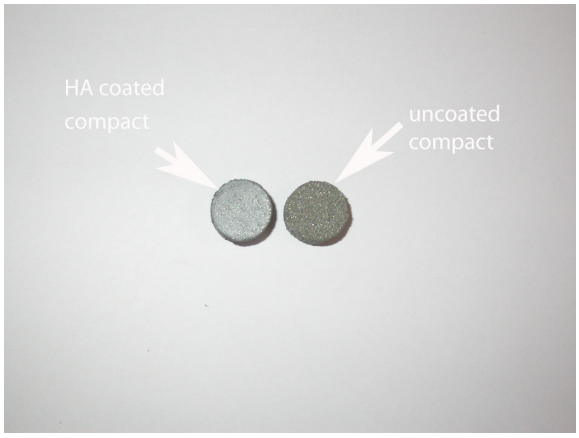

Figure 6.30. Sol-derived HA powder coated and uncoated Ti6Al4V sintered power compacts

In order to determine the optimum soaking time that would give relatively homogenous HA coating and not close the initial open porosities extensively. BSE images of the compact sample coated at 1, 2, 3, 4 and 5 minutes soaking times were taken and corresponding images are shown sequentially in Figures 6.31.(a) through (e). In BSE images, the coated and uncoated regions of a particle are seen grey and white, respectively and the open pores are seen dark. Through the color change in these figures, one can find that the pores are open until 3-minute soaking, while at 4 and 5-

minute soakings the pores are mostly closed. Since the pore closing is extensive after 3-minute soaking and fewer number of particles are coated at soaking times less than 3 minutes, the optimum soaking time is determined to be 3 minutes.

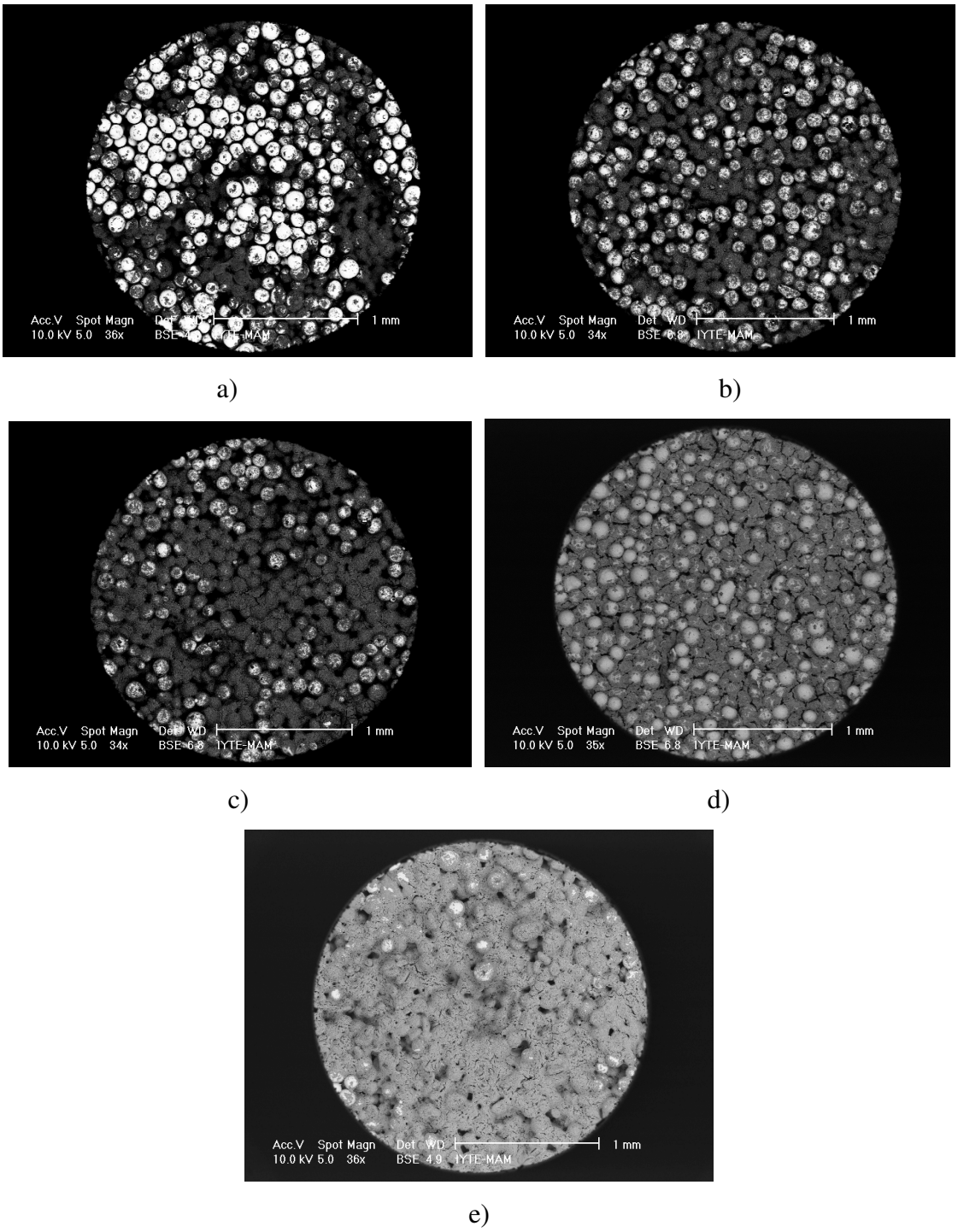

Figure 6.31. BSE images of the compact samples surfaces after different soaking times; a) 1, b) 2, c) 3, d) 4 and e) 5 minutes.

The thickness of the coatings as a function of the soaking time was determined through SEM observations of the coating layer which accommodated cracks. SEM micrographs seen in Figures 6.32.(a-e) show sequentially the measurements of the thicknesses of the coating layer at soaking times of 1, 2, 3, 4 and 5 minutes. At least 5 measurements were taken for each soaking time and the measurements were reported as the average thickness values. The variation of the thicknesses of the coating layer as a function of the soaking time are shown in Figure 6.33. The coating thickness increases with increasing soaking time, from 0.94µm at 1-minute soaking to 7.01µm at 5-minute soaking. Note that at the optimum soaking time of 3-minute the average thickness of the coating is 2.2 micrometers and after this optimum soaking time the thickness of the coating layer increases rapidly. The XRD spectra of a coated compact sample with 5-minute soaking shown in Figure 6.34. prove that the coating layer is HA. FTIR analyses of sol derived powder are shown in Figure 6.35. Carbonate peaks can be seen at 552and 1758cm^{-1}. The phosphate peak observed at 1018. The strong peak at 552 represented CO_3^{2-}. The broad peak at 3500 cm^{-1} corresponds to the absorbed water.(Liu et al. 2002, Hsieh et al. 2002) EDX analysis of the coating layer gives a Ca/P molar ratio of 1.67 as shown in Figure 6.36.

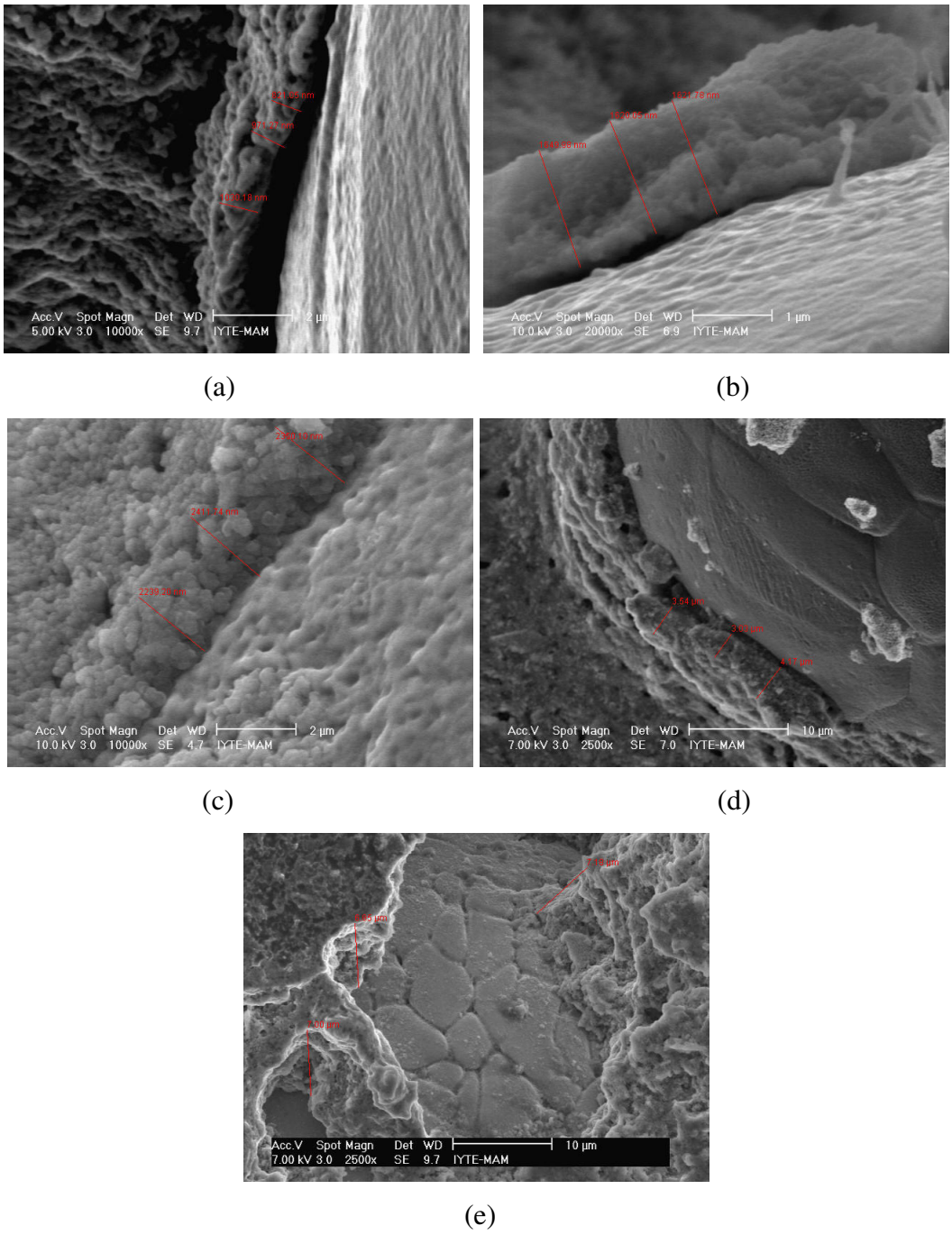

Figure 6.32. The thickness measurements of the coating; soaking time a) 1, b) 2, c) 3, d) 4 and e) 5 minutes.

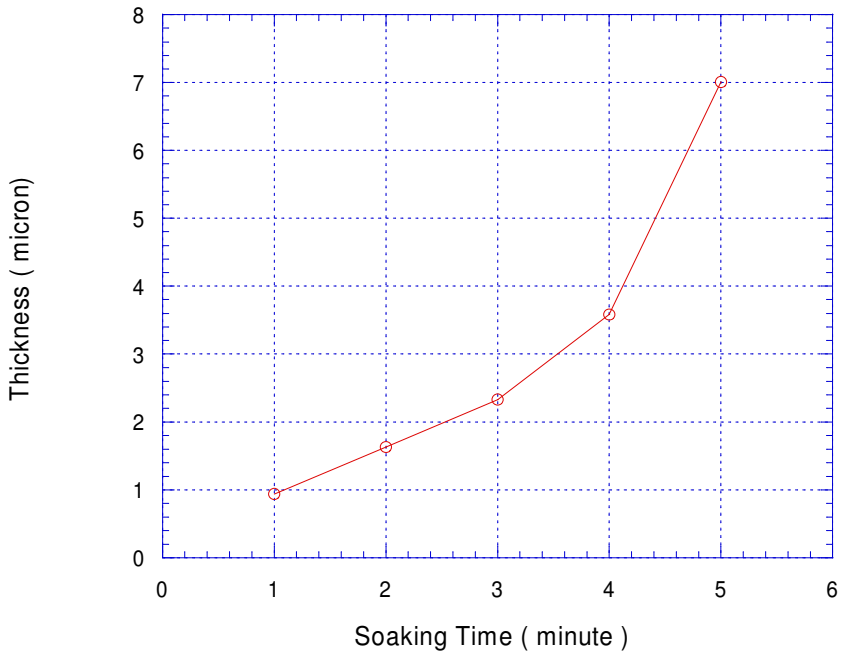

Figure 6.33. The thickness of the coating layer as a function of soaking time.

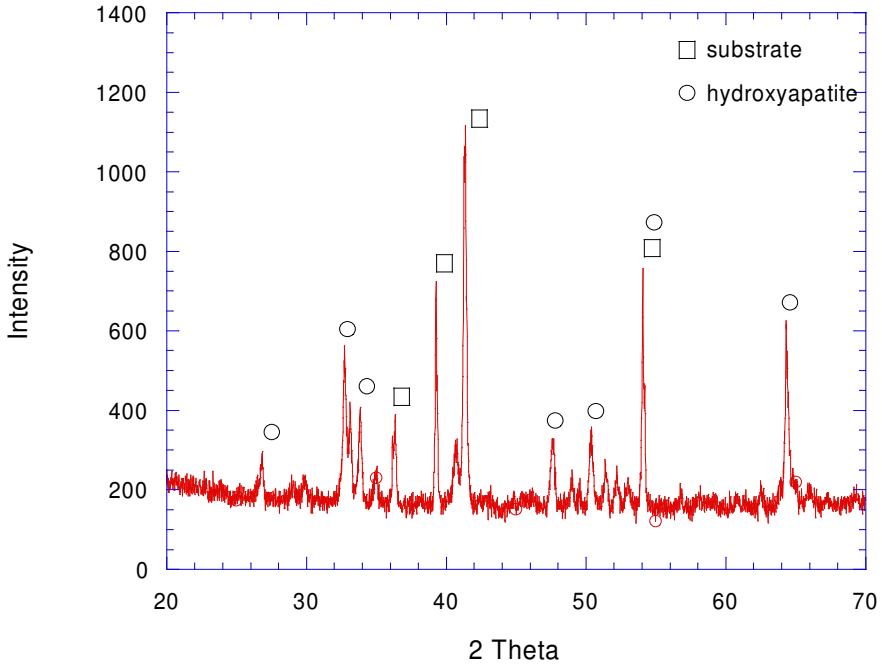

Figure 6.34. XRD pattern of sol-derived HA coated compact sample (5-minute soaking).

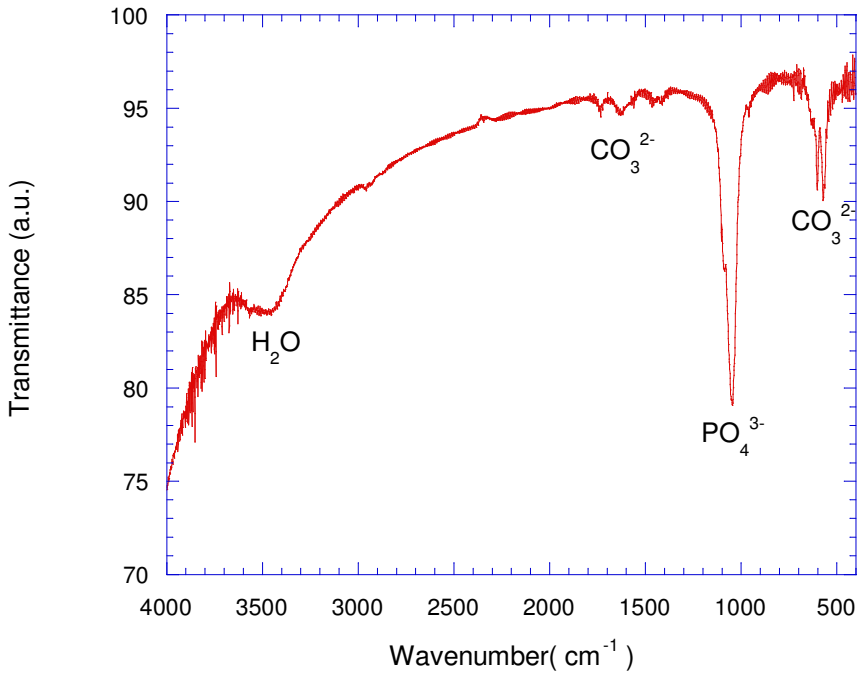

Figure 6.35. FTIR analyses of sol derived powder

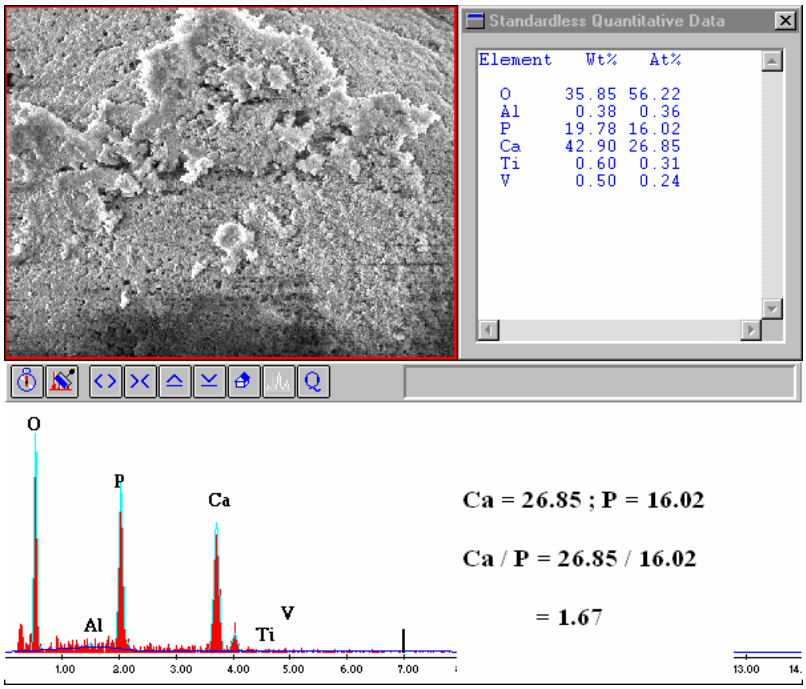

Figure 6.36. EDX analysis of sol-derived HA coated compact sample (5-minute soaking).

6.3. CaP Coating in SBF Solution

6.3.1. 1xSBF

Although no precipitation is observed in untreated compact samples, CaP precipitation is detected in NaOH-treated compact samples after 7-day soaking in SBF as shown in Figure 6.37. CaP precipitation in untreated compact sample is observed after 10-day soaking (Figure 6.38.). After 10-day soaking, the surfaces of the particles of NaOH-treated compact sample are however partially covered with a CaP layer as shown in Figure 6.39. In both samples, untreated and treat, spherical CaP precipitates first forms and later these spherical particles turn into a continuous coating layer as the precipitation progresses further. After 14-day soaking the surfaces of the particles of treated compact sample are completely coated with CaP layer as seen in Figure 6.40. At this soaking time, the surfaces of particles of untreated compact samples particles are only partially coated (Figure 6.41.). The thickness of the coating layer in NaOH-treated compact sample is about 3.14 micrometers after 14-day soaking (Figure 6.42.). The coating in untreated compact sample is complete after 21 days of soaking (Figure 6.43.). The thickness of the coating layer in untreated compact sample after 21-day soaking is clearly seen in Figure 6.44. and measured 6.15-11.06 micrometers.

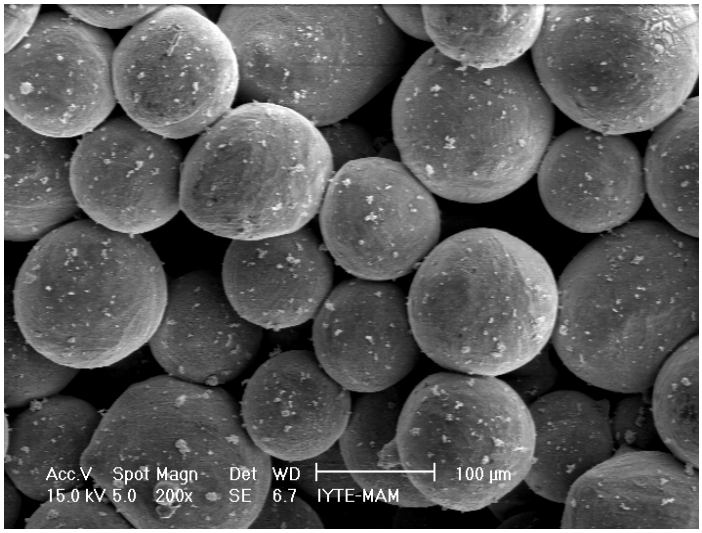

Figure 6.37. SEM micrograph of NaOH-treated compact sample after 7-day soaking in 1xSBF.

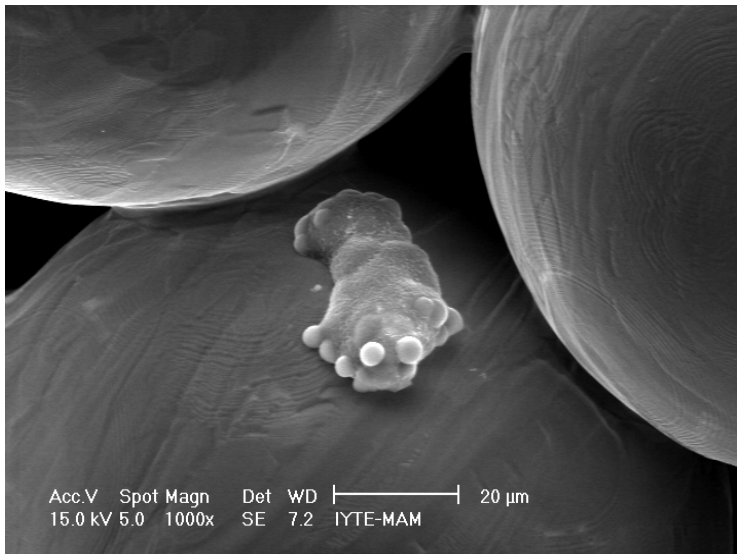

Figure 6.38. SEM micrograph of untreated compact sample after 10-day soaking in 1xSBF

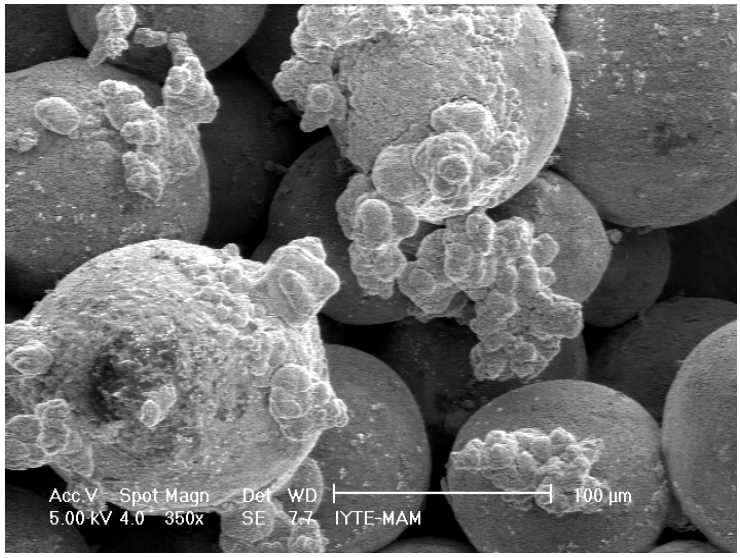

Figure 6.39. SEM micrograph of NaOH-treated compact sample after 10-day soaking in 1xSBF.

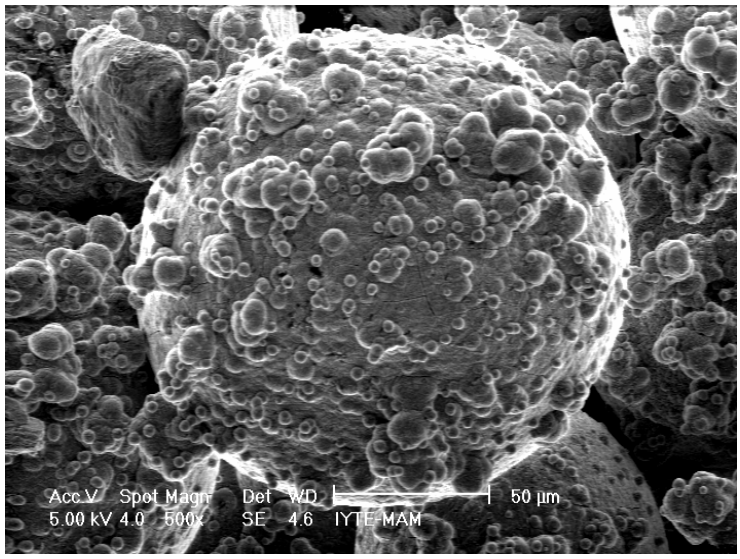

Figure 6.40. SEM micrographs of NaOH-treated compact sample after 14-day soaking in 1xSBF.

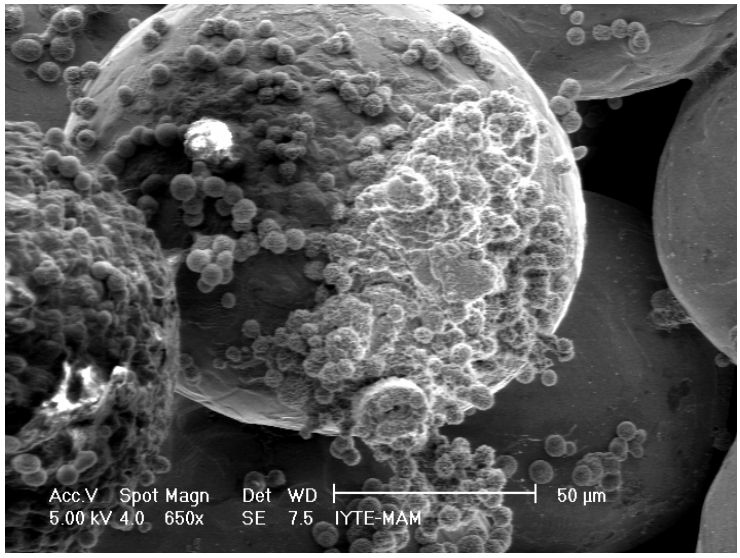

Figure 6.41 SEM micrograph of untreated compact sample after 14-day soaking in 1x SBF.

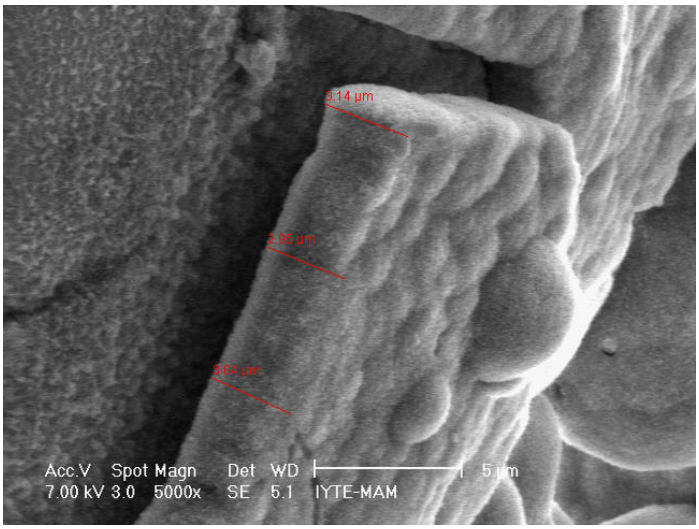

Figure 6.42. The thickness of CaP coating layer of NaOH-treated sample after 14-days soaking in 1xSBF.

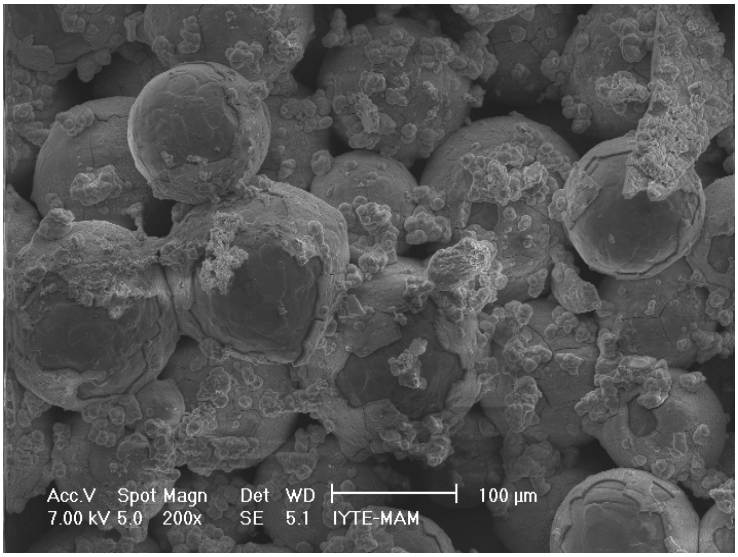

Figure 6.43. SEM micrograph of untreated compact sample after 21-day soaking in 1xSBF.

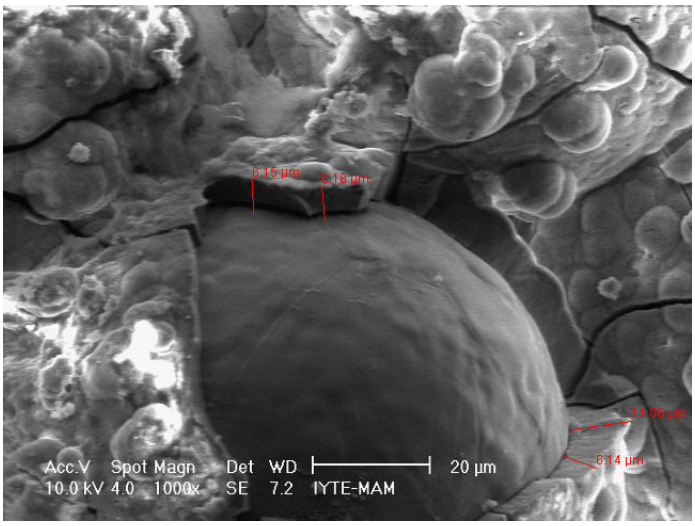

Figure 6.44. The SEM micrograph of untreated compact sample after 21-day soaking in 1xSBF showing the thickness of the coating.

The microstructure of the coating layer in both samples, treated and untreated compacts is composed of needle-like precipitates as seen in Figures 6.45.(a) and (b). BSE views of untreated and treated sample surfaces after 14-day soaking are shown in Figure 6.46.(a) and (b) respectively. It is clearly seen in these figures that NaOH-treated compact sample surface is completely coated with a CaP layer (Figure 6.46.(b)), while the whiter particles seen in Figure 6.46.(a) are uncoated or partially coated particles in untreated sample after 14-day soaking. This has confirmed that the coating in NaOH-treated samples is faster than that of the untreated samples. After 14 days, it was also observed that the pores less than 100 micrometers were closed with a CaP layer in treated sample. EDX analysis of the coating layer gives a Ca/P molar ratio of 1.72 as shown in Figure 6.47. XRD analysis has shown that the coating layer in both compact samples is HA (Figure 6.48.).

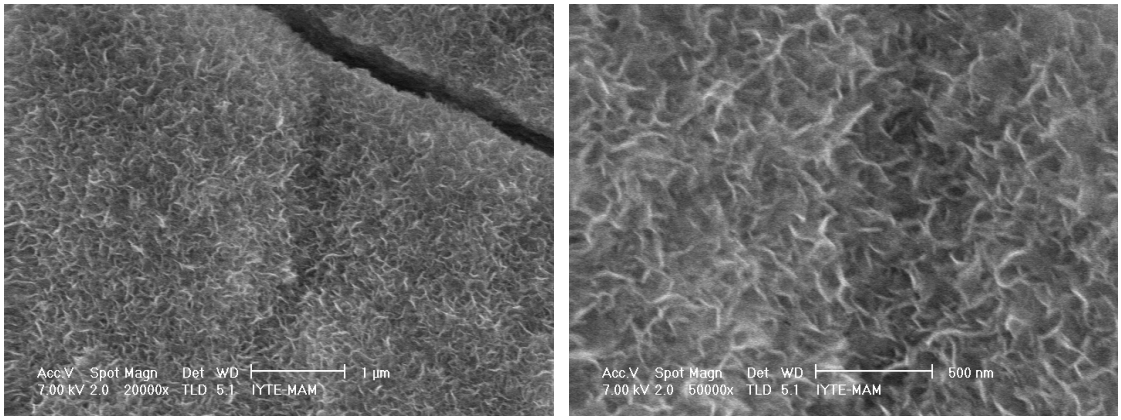

(a) (b)

Figure 6.45. The SEM micrographs of CaP layer in 1XSBF showing needle-like precipitates: a) 5000x and b) 20000x.

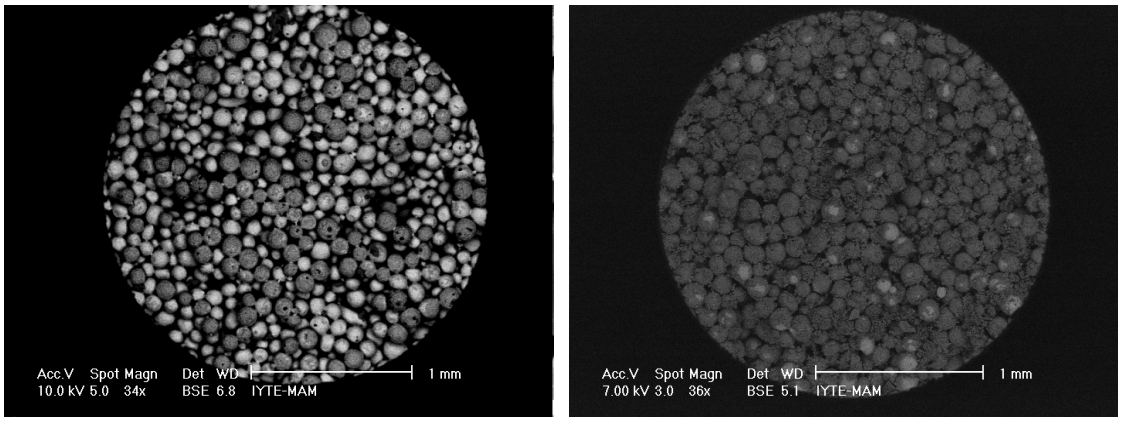

(a) (b)

Figure 6.46. BSE images of the coated compacts after 14-day soaking in 1xSBF (a) untreated and (b) NaOH-treated.

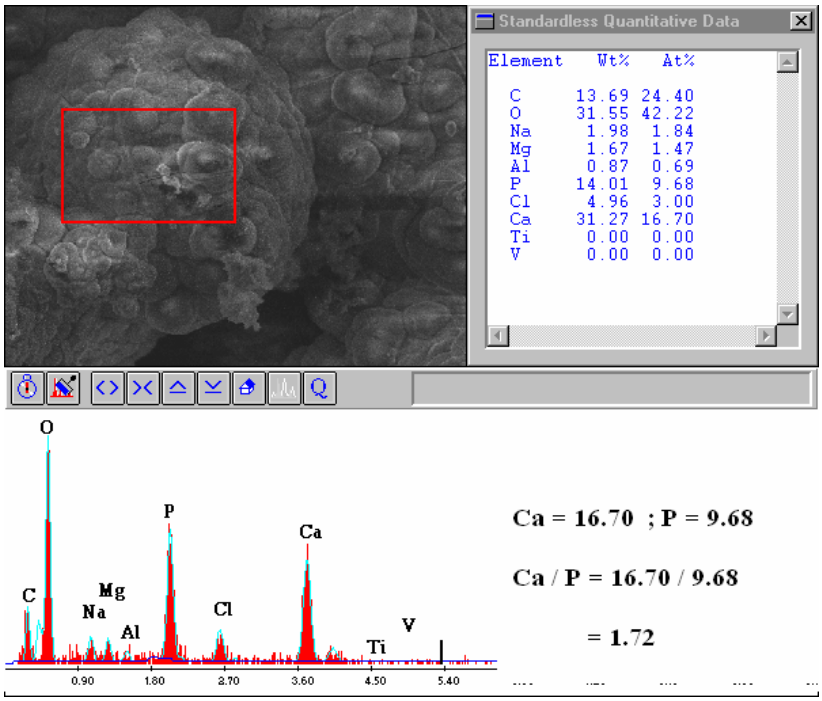

Figure 6.47. EDX analysis of powder coated compact sample (21-day soaking in 1xSBF).

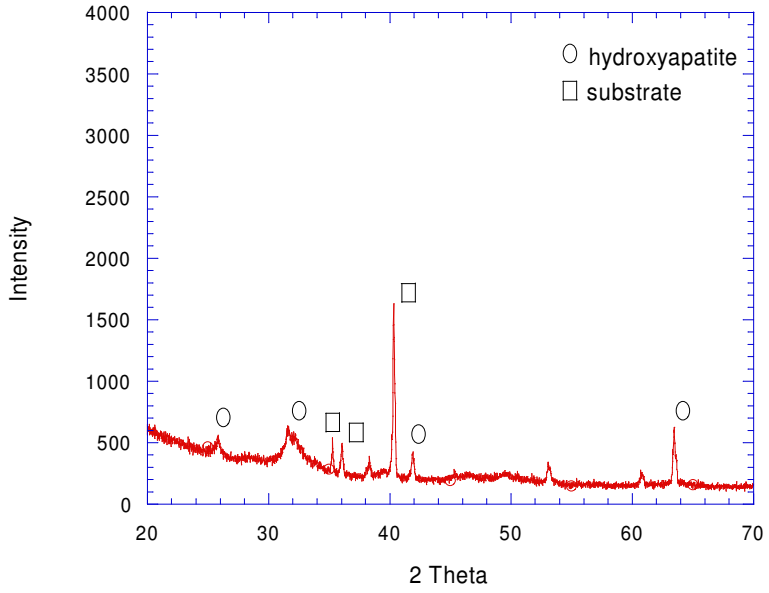

Figure 6.48. XRD spectra of the untreated compact samples after 21-day soaking in 1XSBF

6.3.2. 5xSBF

CaP precipitates are observed in small areas on the surfaces of the Ti6Al4V particles in NaOH-treated compact samples after 7-hour soaking as seen in Figure 6.49. After 12-hour soaking, CaP precipitates start to turn into a continuous coating layer in NaOH-treated compact samples (Figure 6.50.). The precipitation proceeds as the spherical CaP precipitates forming on the previous precipitates. No CaP precipitation is detected in untreated compact samples until 16-hour soaking in 5xSBF. After 16-hour soaking the first CaP precipitates are observed to start to form at sintering necks of the particles (Figure 6.51.). After 18-hour soaking, much of the particles of the NaOH-treated compacts are almost completely coated with CaP (Figure 6.52.), while the particles in untreated compacts are only partially coated (Figure 6.53.). After 24-hour soaking, the surfaces of the particles in NaOH-treated compact sample are completely coated (Figure 6.54.). Hence, the coating process is presumably completed in 24 hours. The final thickness of the coating is measured 4 micrometers after 24-hour soaking in NaOH-treated compact sample as shown Figure 6.55. In untreated compact sample, the particle surfaces are not completely coated after 24-hour soaking (Figure 6.56.). After 26-hour soaking a thin continuous layer of CaP coating was however observed to form. The coating process is observed to be progressive after 30 and 34-hour soaking as shown in Figures 6.57. and 6.58., respectively. After 36-hour soaking the surfaces of the particles of untreated compact sample are completely coated with a continuous CaP layer (Figure 6.59.).

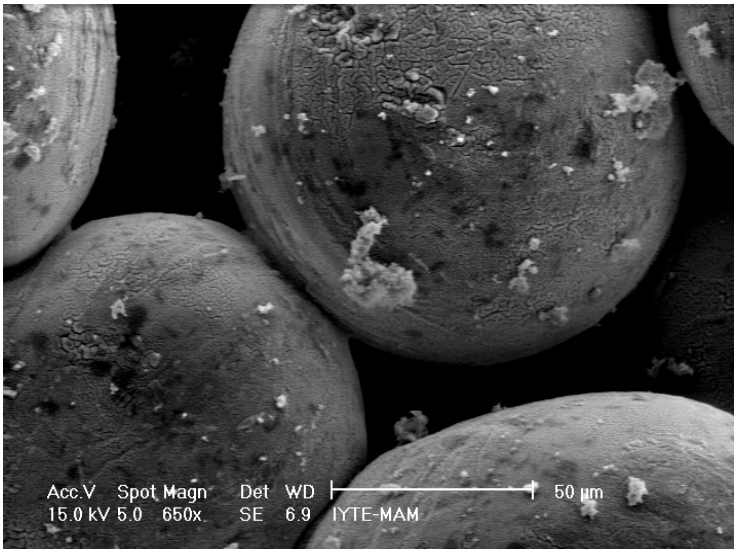

Figure 6.49. SEM micrograph of NaOH-treated compact sample after 7-hour soaking in 5xSBF.

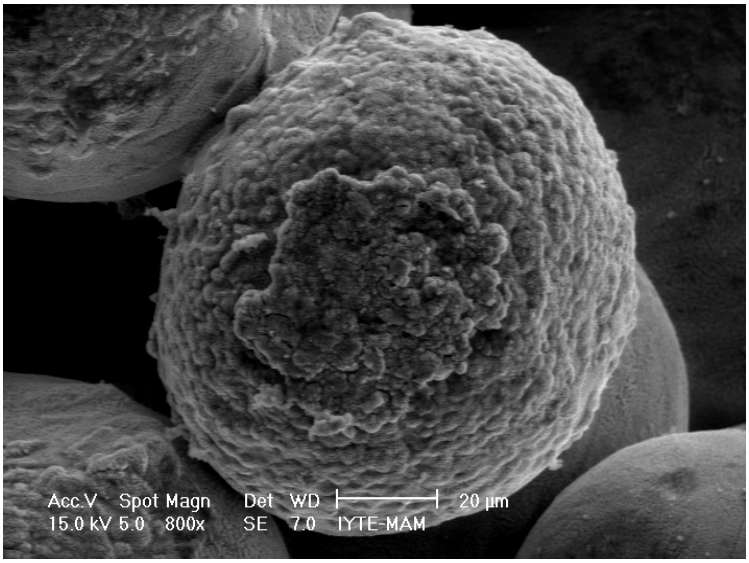

Figure 6.50. SEM micrograph of NaOH-treated compact sample after 12-hour soaking in 5xSBF.

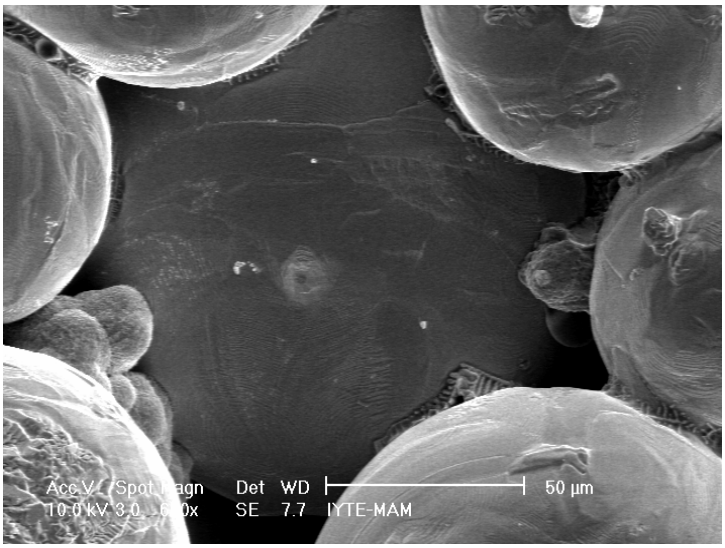

Figure 6.51. SEM micrographs of untreated compact sample after 16-hour soaking in 5xSBF.

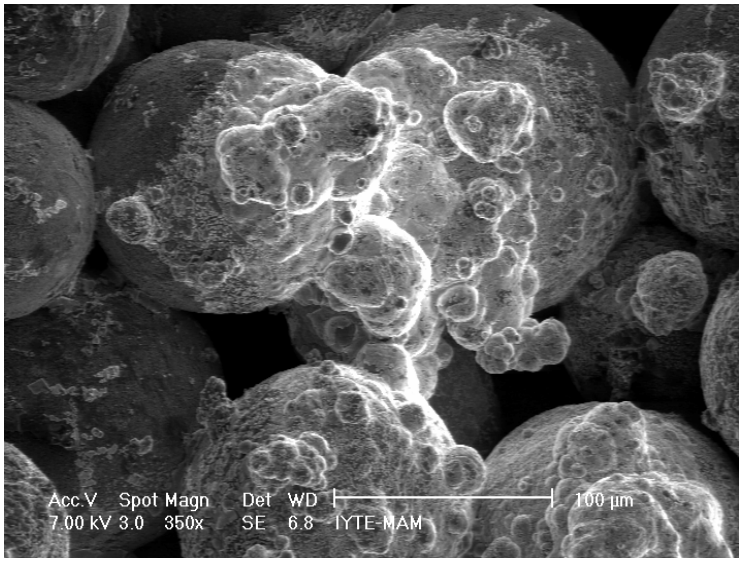

Figure 6.52. SEM micrograph of NaOH-treated compact sample after 18-hour soaking in 5xSBF.

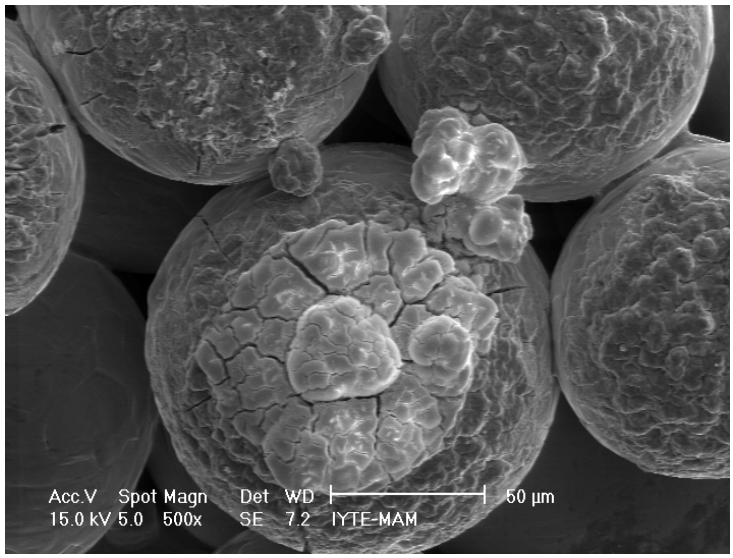

Figure 6.53. SEM micrographs of untreated compact sample after 18-hour soaking in 5xSBF.

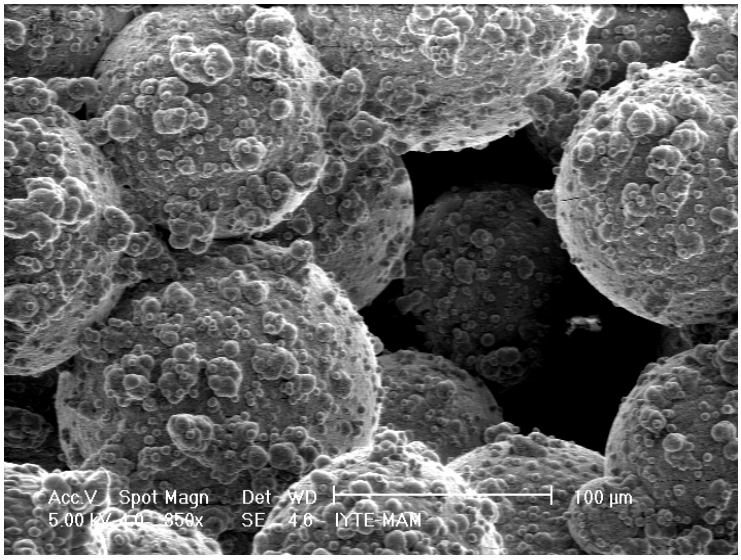

Figure 6.54. SEM micrograph of NaOH-treated compact sample after 24-hour soaking in 5xSBF.

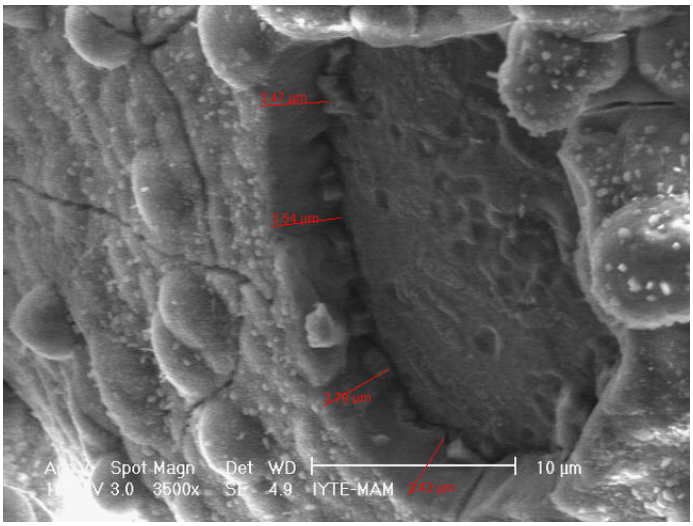

Figure 6.55. SEM micrograph of NaOH-treated compact sample after 24-hour soaking in 5xSBF showing a coating thickness of nearly 4 micrometers.

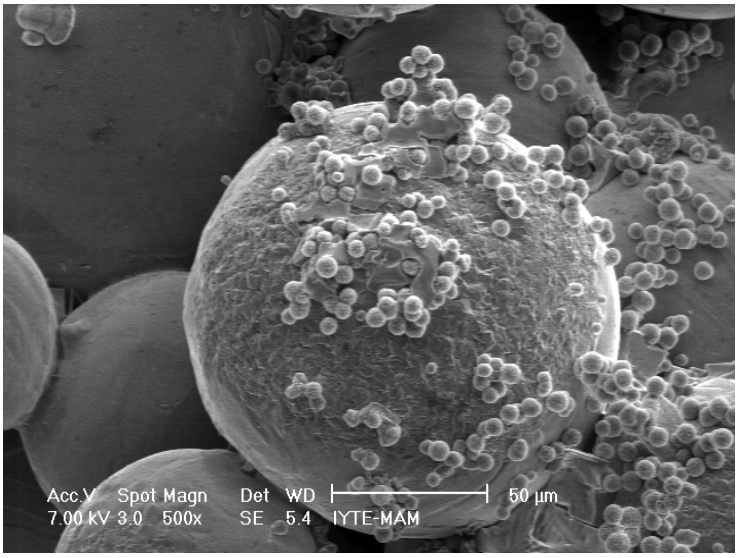

Figure 6.56. SEM micrograph of untreated compact sample after 24-hour soaking in 5xSBF.

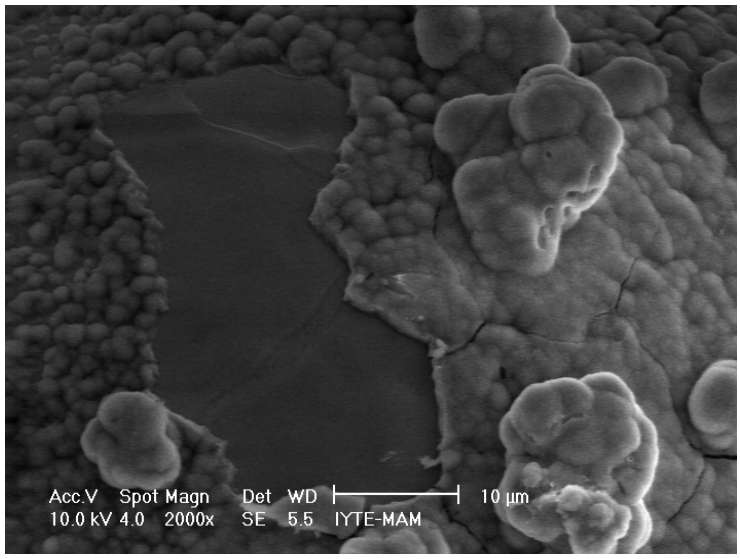

Figure 6.57. SEM micrograph of untreated compact sample after 30-hour soaking in 5xSBF.

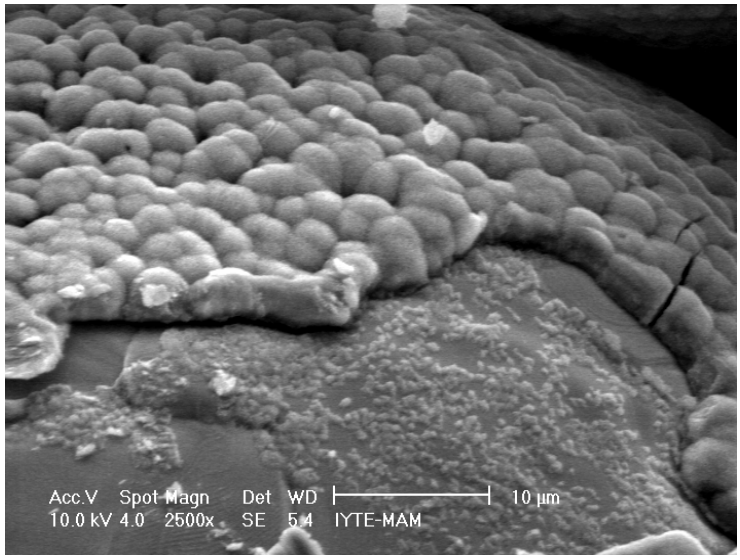

Figure 6.58. SEM micrograph of untreated compact sample after 34-hour soaking in 5xSBF.

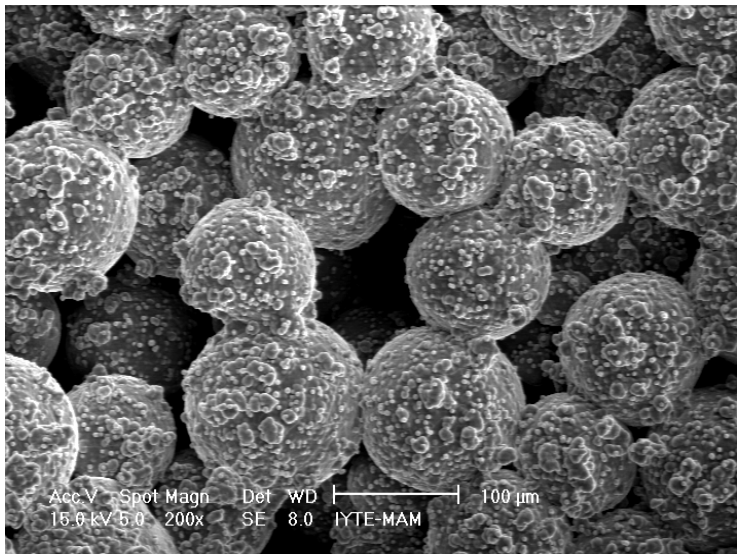

Figure 6.59. SEM micrograph of untreated compact samples after 36-hour soaking in 5xSBF.

In a regular experiment the coated compact sample was dried at room temperature for 2 days before they were taken to SEM observation. The coated untreated compact samples (36-hour soaking) were also dried in a furnace at 110 ^{0}C for 4 and 8 hours before SEM analysis in order to see the effects of drying temperature on the morphology and thickness of the coating layer. Drying at elevated temperature results in smoothing the coating layer surface as seen in Figure 6.60. Drying at elevated temperature is however observed to form cracks on the coating layer (Figure 6.60.). Increasing the drying duration from 4 to 8 hours induces more cracks on the coating layer (Figure 6.61.). It is noted that the cracks formed during drying are transgranular (Figure 6.63.), proving brittleness of the CaP coating layer formed in SBF. Another effect of drying at elevated temperature is the reduction of the coating layer thickness. In room-temperature dried samples the thickness of the coating layer is approximately 3.5 micrometers (Figure 6.65.), while drying at 110 C for 8 hours reduces the coating thickness to 2.5 micrometers. (Figure 6.62.)

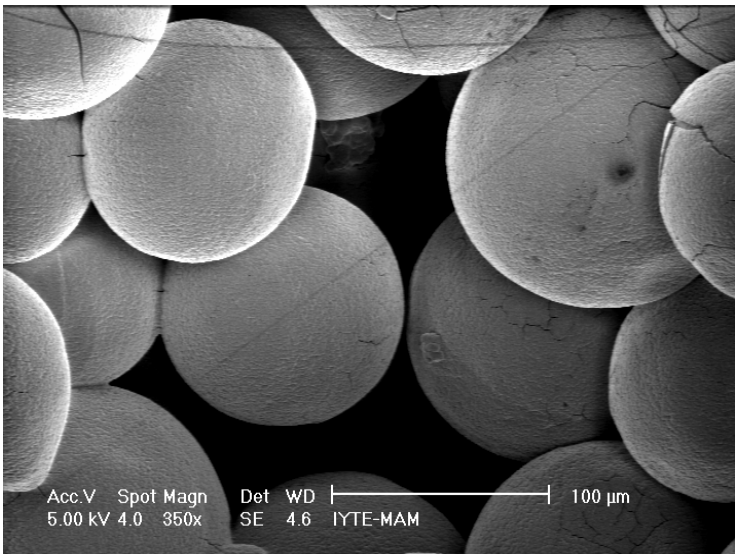

Figure 6.60. SEM micrograph of untreated compact sample after drying at 110°C for 4 hours.

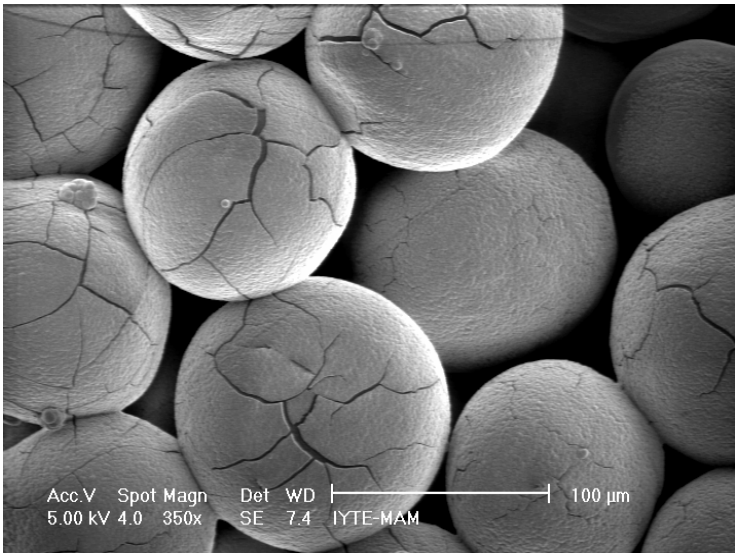

Figure 6.61. The SEM micrograph of untreated compact sample after drying at 110°C for 8 hours.

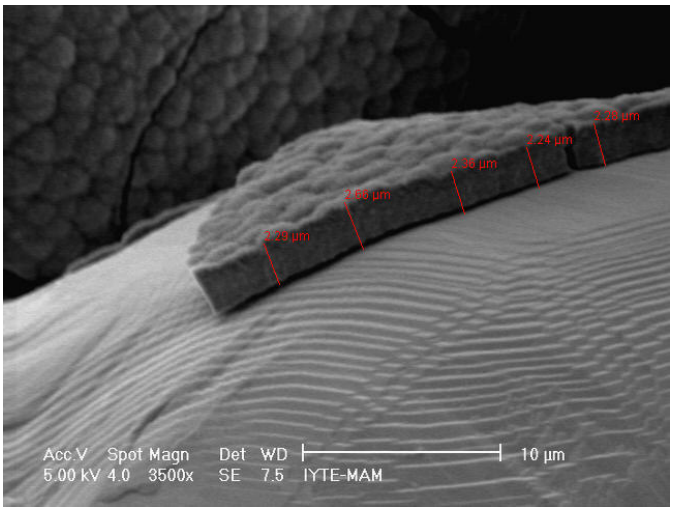

Figure 6.62. The SEM micrograph of untreated compact sample after drying at 110ºC for 8 hours showing the thickness of the coating.

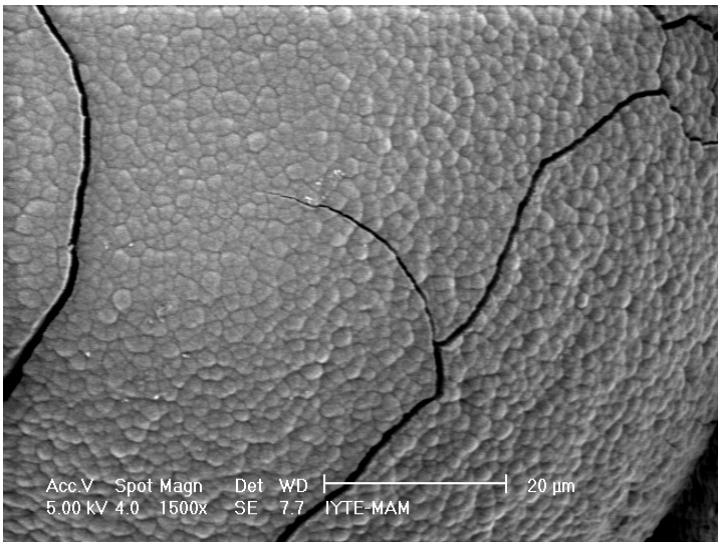

Figure 6.63. SEM micrograph of untreated compact sample after drying at 110ºC for 8 hours showing transgranular cracks.

Figures 6.64.(a), (b) and (c) explain the progressive coating process in untreated compact samples. The precipitation starts with the nucleation of the spherical particles. As the nucleation and growth of the particles continue a continuous layer of CaP layer forms on the surface of the Ti6Al4V particles. Further nucleation proceeds on the continuous CaP layer as seen in Figure 6.64.(a). The precipitation is also seen to proceed to the normal to surface of the coating layer (Figures 6.64.(b) and (c)). The above observations are also found to be valid for the coating of NaOH-treated compacts.

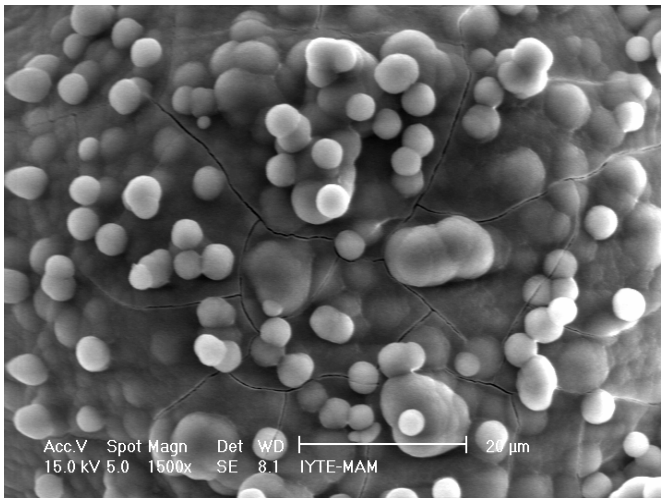

a)

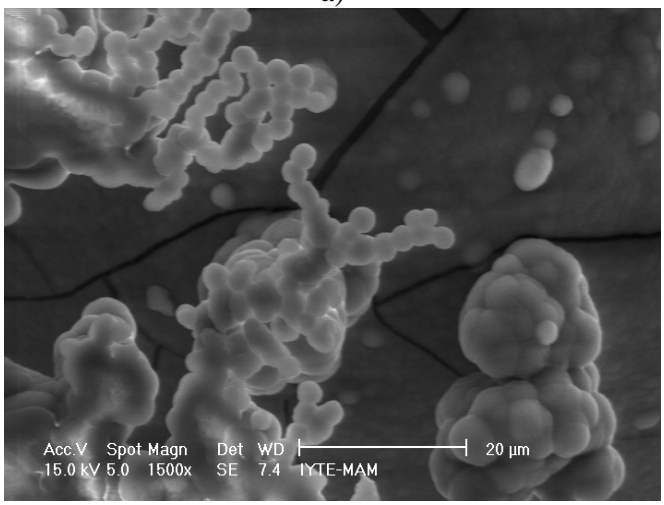

b)

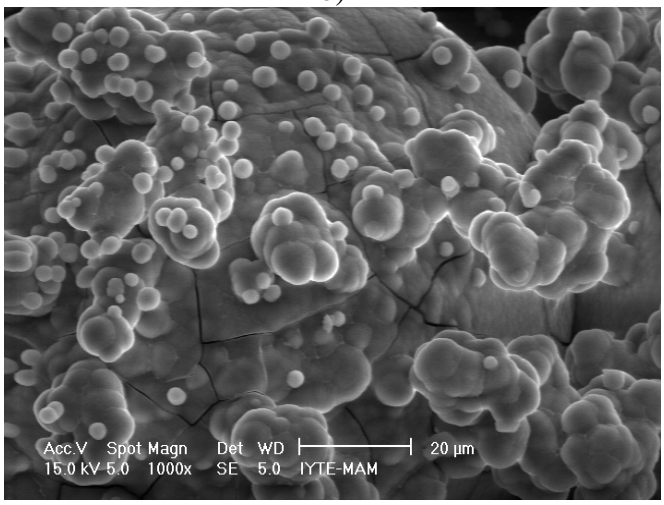

c)

Figure 6.64. The SEM micrographs showing CaP coating process in an untreated compact samples (a) spherical precipitates and (b) and (c) precipitates normal to the particle surface.

SEM micrographs of the coating thickness measurements in untreated samples are shown in Figures 6.65.(a-e) for various soaking times after 26 days. In Figures 6.65., the variation of thicknesses of the coating layer as a function of soaking time is shown. As the soaking time increases from 26-hour to 36-hour, the thickness of the coating layer increases from 1.7 to 3.2 micrometers as seen in Figure 6.66. Note that the coating layer thickness almost shows a linear dependence to the soaking time. A close inspection of the spherical particles seen on the coating surface also reveals that the microstructure is composed of needle-like surface morphology (Figure 6.67.), similar to the compacts sample surfaces soaked in 1xSBF. The needle-like morphology is observed in both untreated and treated compact samples.

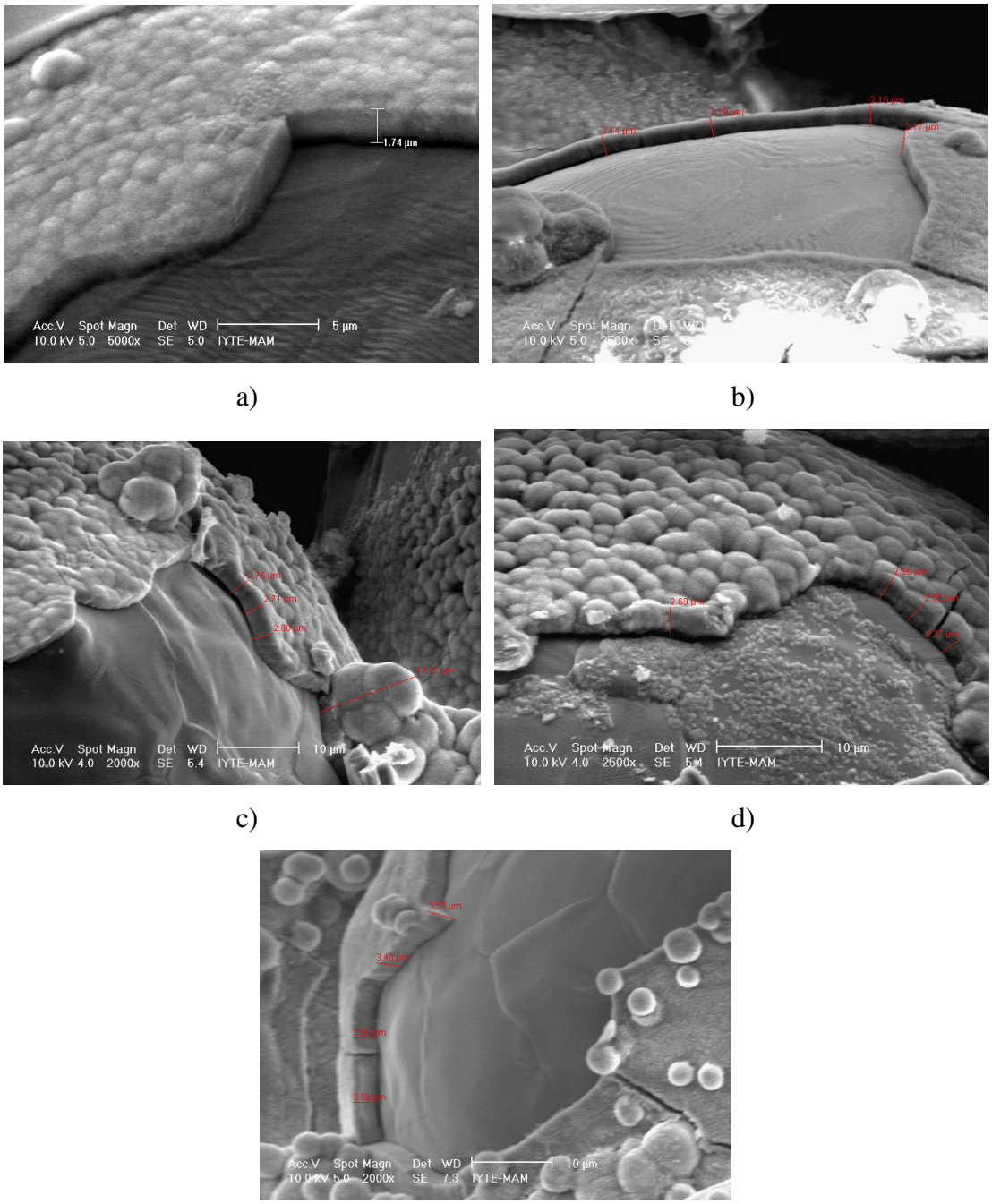

Figure 6.65. SEM micrographs of coating thickness measurements; soaking times (a) 26, (b) 28, (c) 30, (d) 32, (e) 36-hour

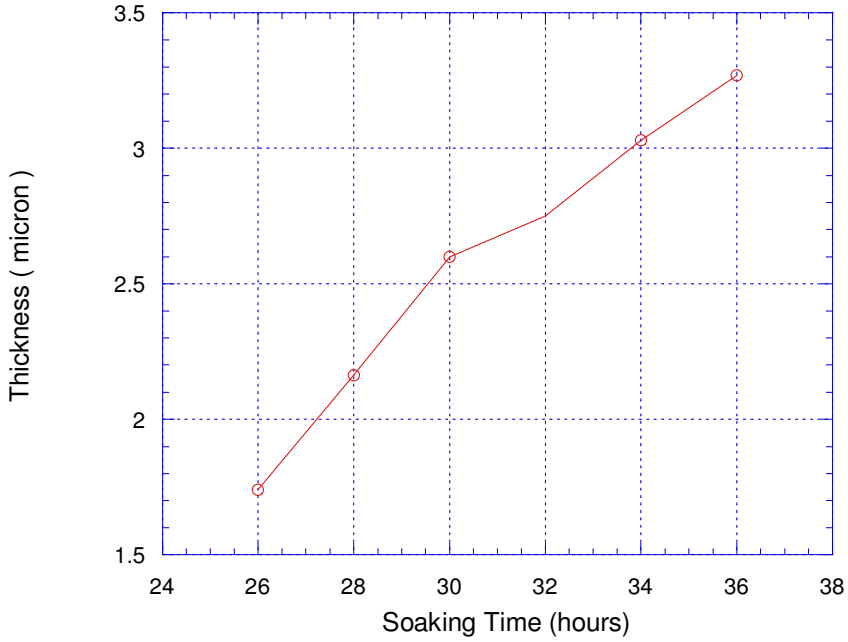

Figure 6.66. The variation of thicknesses of the coating layer as a function of the soaking time.

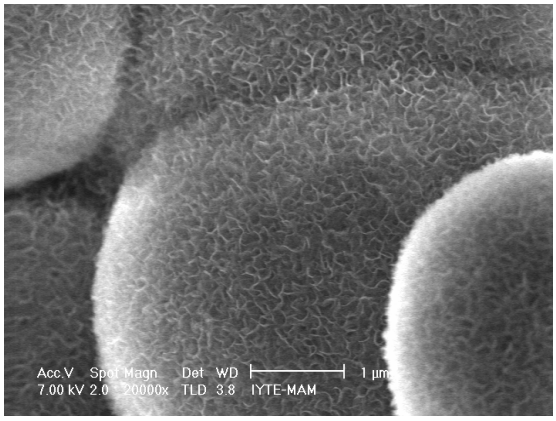

Figure 6.67. The SEM micrograph of CaP layer in untreated compact sample showing needle-like precipitates.

BSE analysis of the coated compact samples of untreated (36-hour soaking) and treated compact (24-hour soaking) samples shown in Figure 6.68.(a) and (b), respectively, also confirm that the coating is complete after 36 hours in untreated sample and after 24 hours in NaOH-treated sample. Further increase in soaking time is expected to close the open pores of the coated compacts. The XRD analysis of the completely coated samples has shown the formation of HA on the surface (Figure 6.69.). The EDX analysis of the completely coated sample gives a Ca/P ratio of 1.63, which is very close to that of human bone (Figure 6.70.).

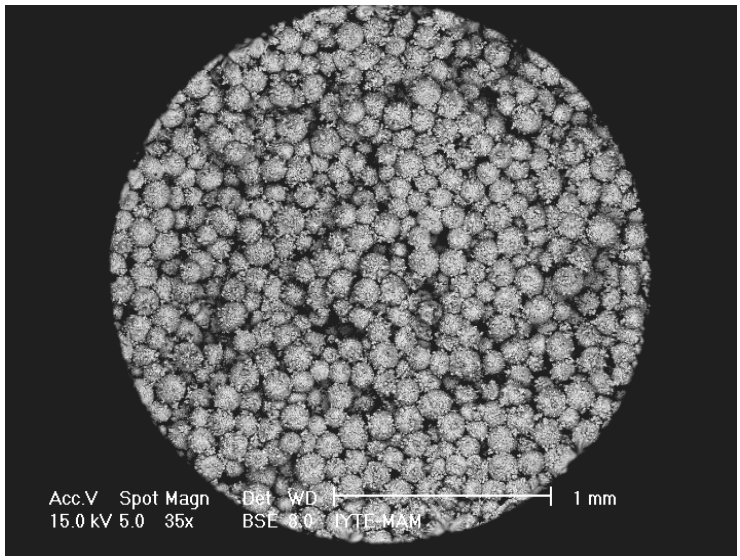

(a)

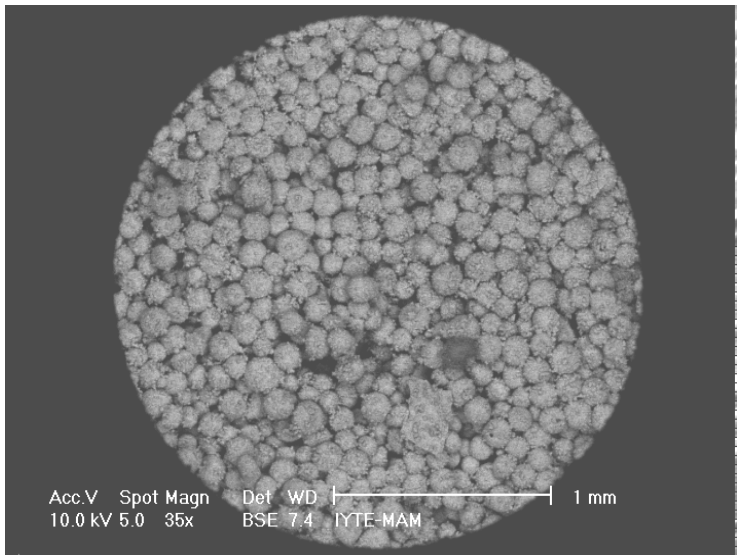

(b)

Figure 6.68 . BSE micrographs of (a) untreated compact sample after 36-hour soaking and (b) treated compact sample after 24-hour soaking in 5xSBF

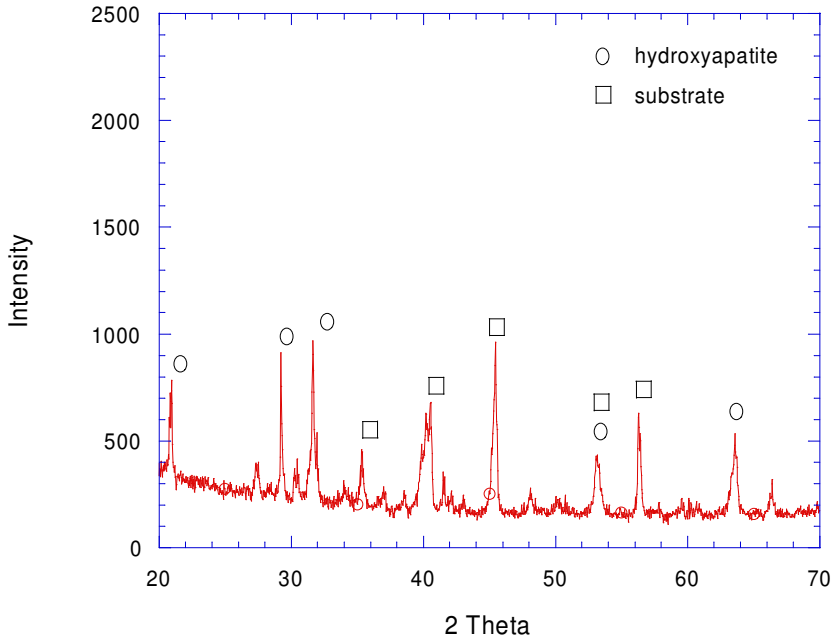

Figure 6.69. XRD spectra of the untreated compact sample after 36-hour soaking in 5xSBF.

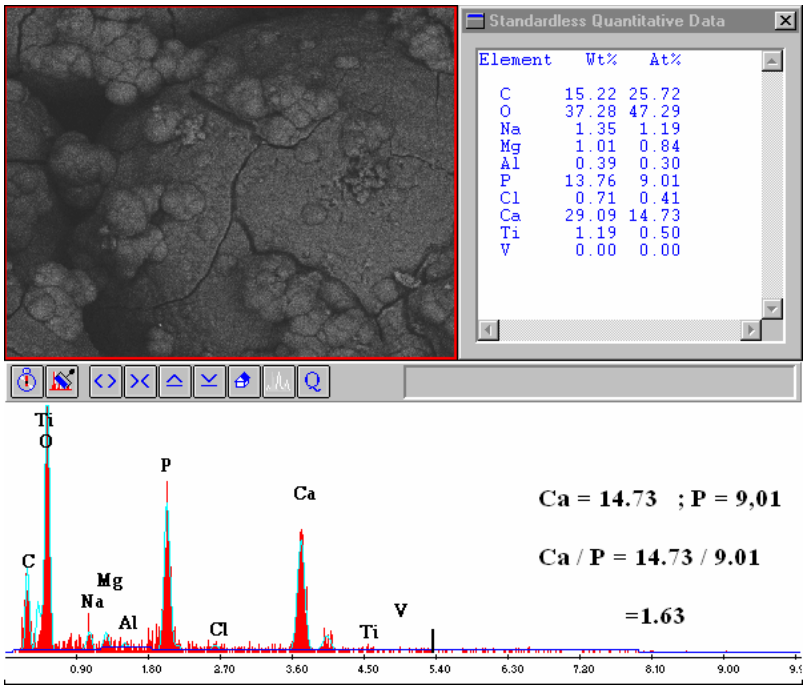

Figure 6.70. EDX analysis of the untreated compact sample after 36-hour soaking in 5xSBF.

6.3.3. 10xSBF

Both treated and untreated compact samples show CaP precipitation after 2-hour soaking in 10xSBF solution as shown in Figures 6.71.(a) and (b), respectively. It is noted in Figures 6.71.(a) and (b) that the morphology of precipitation formed in 10xSBF solution is different from that formed in 1 and 5xSBF solutions. In 10xSBF, CaP precipitation is in the form of rosette and plate-like, both forming on the surfaces of the particles.

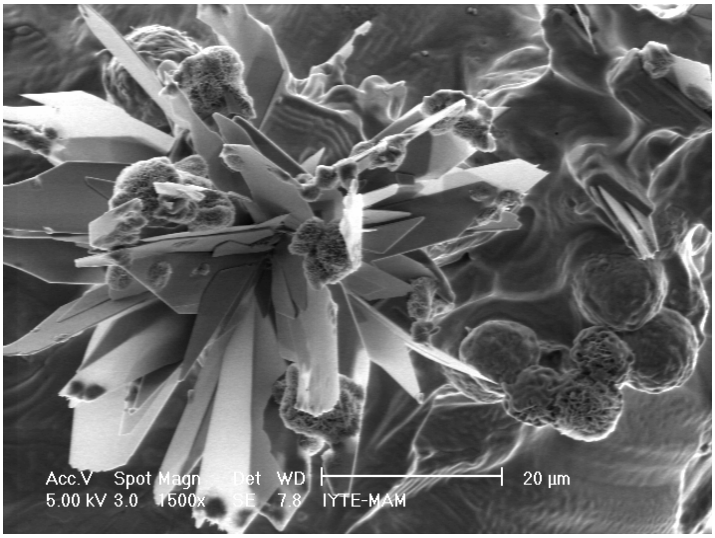

(a)

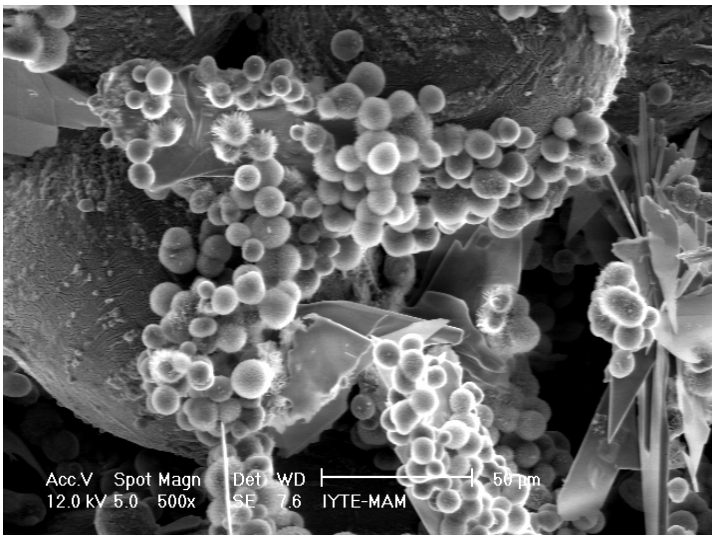

(b)

Figures 6.71. CaP precipitation in (a) treated and (b) untreated compact samples after 2-hour soaking in 10xSBF.

As with 1 and 5xSBF solutions, CaP precipitation is faster in NaOH-treated compact sample, again proving the increased rate of the precipitation in treated compact samples. It is also observed that most of the rosette precipitates formed on the surface of the plate-like precipitates and few are also observed on the surfaces of Ti6Al4V particles. This may prove that initial precipitation is in the form of plate-like precipitates.

When the soaking time increases to 4 hours, more CaP precipitates form on the surfaces of the particles in treated and untreated samples as seen in Figure 6.72.(a) and (b) respectively. Most of the particle surfaces are coated with CaP after 4-hour soaking (Figure 6.72.(a)), but the coating is not complete. In untreated samples in much of coated regions rosette type precipitates appear on the surfaces of the plate-like precipitates.

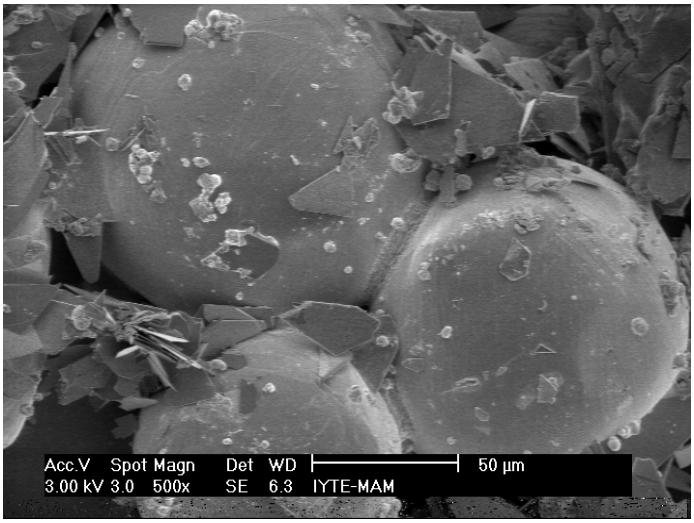

(a)

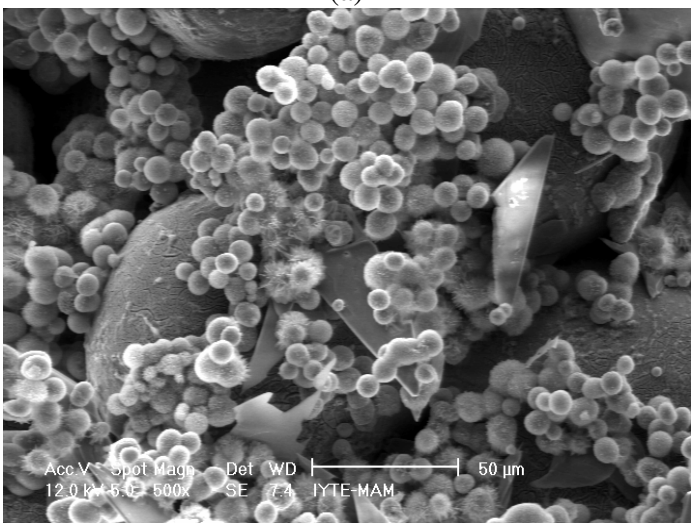

(b)

Figure 6.72. CaP precipitations in (a) treated and (b) untreated compact samples after 4-hour soaking in 10xSBF.

After 6-hour soaking, all surface of the particles of the treated compact sample are coated with a CaP layer (Figure 6.73.(a)) and the thickness of the coating was found 10.7 micrometers. In addition, the plate-like precipitates are found to start to close the initially open pores after 6-hour soaking. As the soaking increases to 6 hours, much plate-like precipitates forms and rosette type precipitates are collected on the surfaces of the plate-like precipitates as shown in Figure 6.73.(b) for an untreated compact sample.

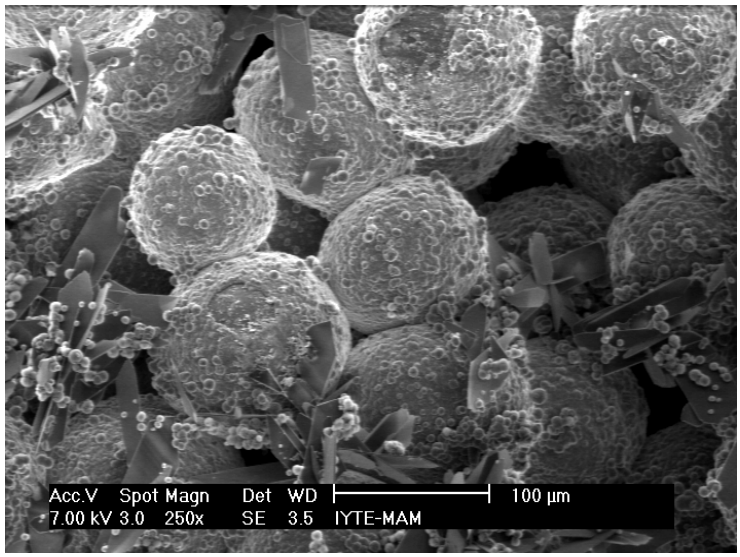

(a)

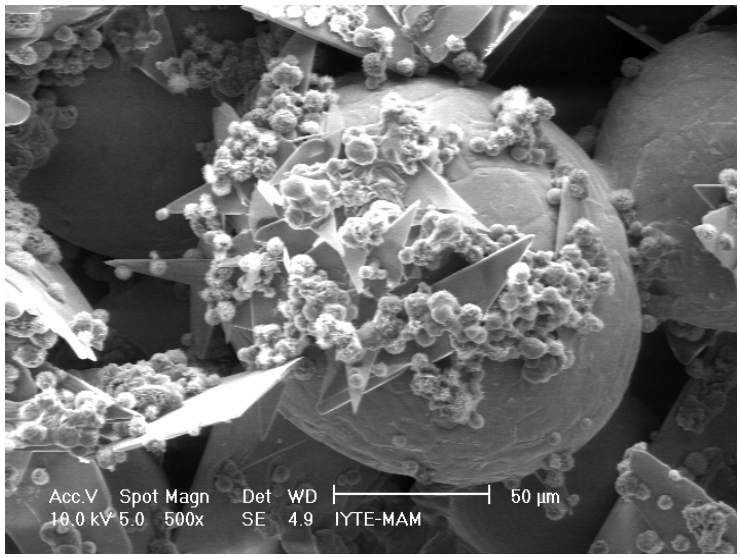

(b)

Figure 6.73. CaP precipitation in (a) treated and (b) untreated compact samples after 6-hour soaking in 10xSBF.

BSE micrographs of the treated and untreated compact samples after 6-hour soaking are shown sequentially in Figure 6.74.(a) and (b). The whiter regions in Figure 6.74.(b) show the uncoated particles in untreated compact sample, while treated samples particles are seen to be completely coated in Figure 6.74.(a). While some particles in untreated compact sample are not coated completely, the plate–like precipitates start to close the initially open pores. It is also noted that, plate-like precipitates are mostly seen in between the particles, on the initial open pores, while rosette type precipitates are found on the surfaces of the particles. Magnified SEM micrograph taken from the spherical precipitates and shown in Figure 6.75. also proves a rosette type surface morphology of the precipitates in 10xSBF solution. This is in contrast to the observed needle-like surface morphology in the samples coated in 1 and 5xSBF solutions.

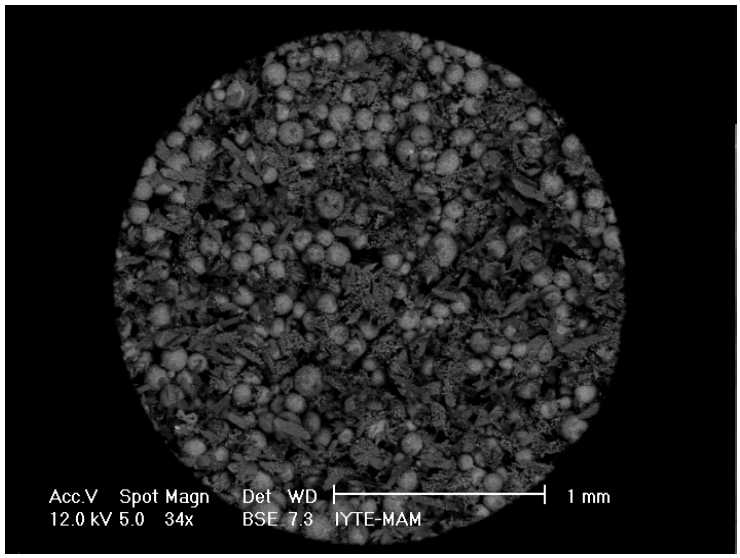

(a)

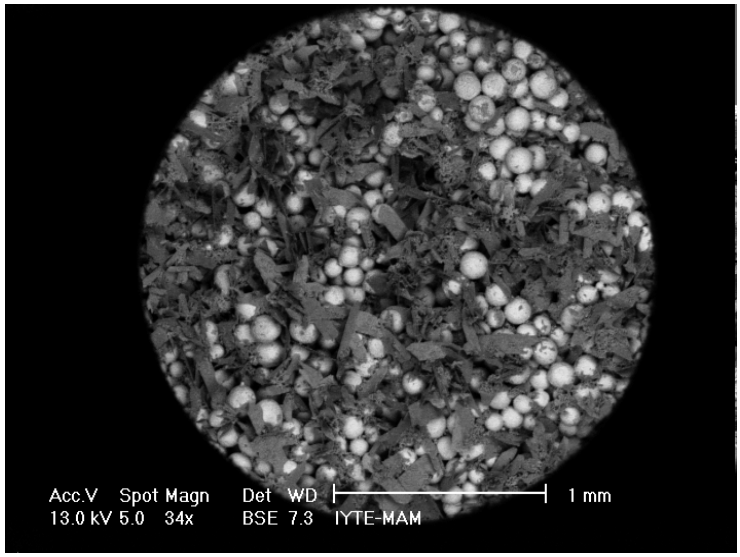

(b)

Figure 6.74. BSE micrographs of CaP precipitation in (a) treated and (b) untreated compact samples after 6-hour soaking in 10xSBF.

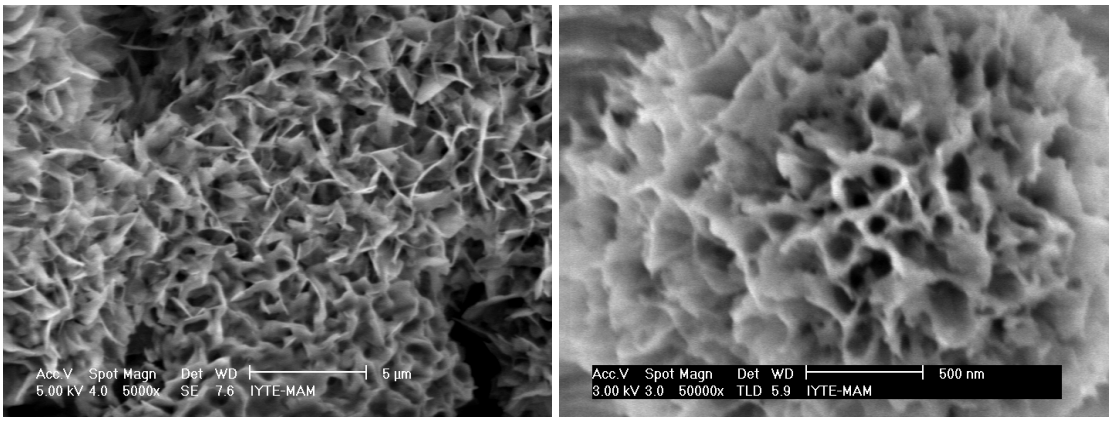

(a) (b)

Figure 6.75. The SEM micrograph of CaP layer in untreated compact sample showing rosette type precipitates in 10xSBF.

The XRD results of the coating layer in untreated samples as a function of soaking time is shown in Figure 6.76. As the soaking time increases the peaks become narrower, proving increased crystallinity of the coating layer with the increasing soaking time. EDX analysis have shown that Ca/P ratio in rosette type precipitates is 1.46 (Figure 6.77.(a)), while it 1.12 in plate-like precipitates (Figure 6.77.(b)).

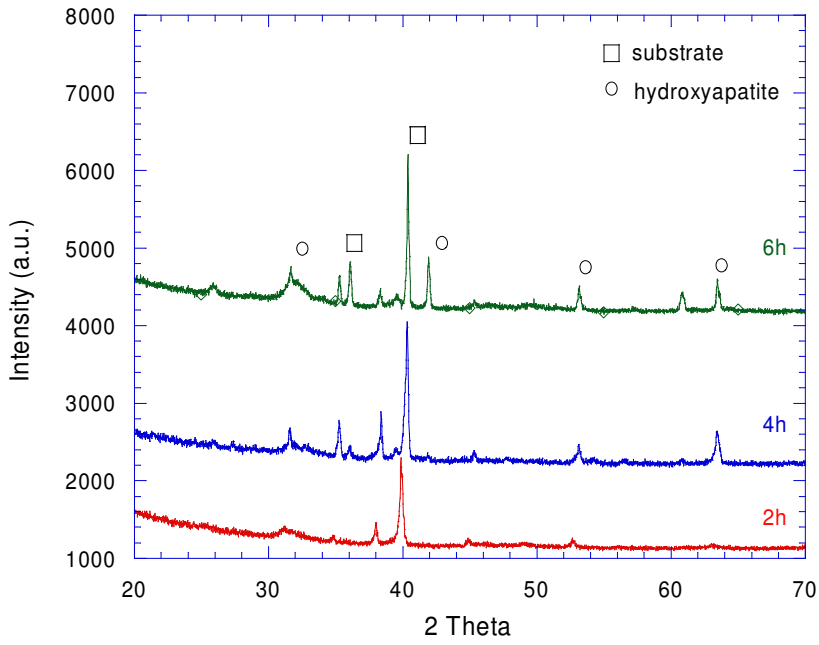

Figure 6.76. XRD spectra of the untreated compact sample after 6-hour soaking in 10xSBF.

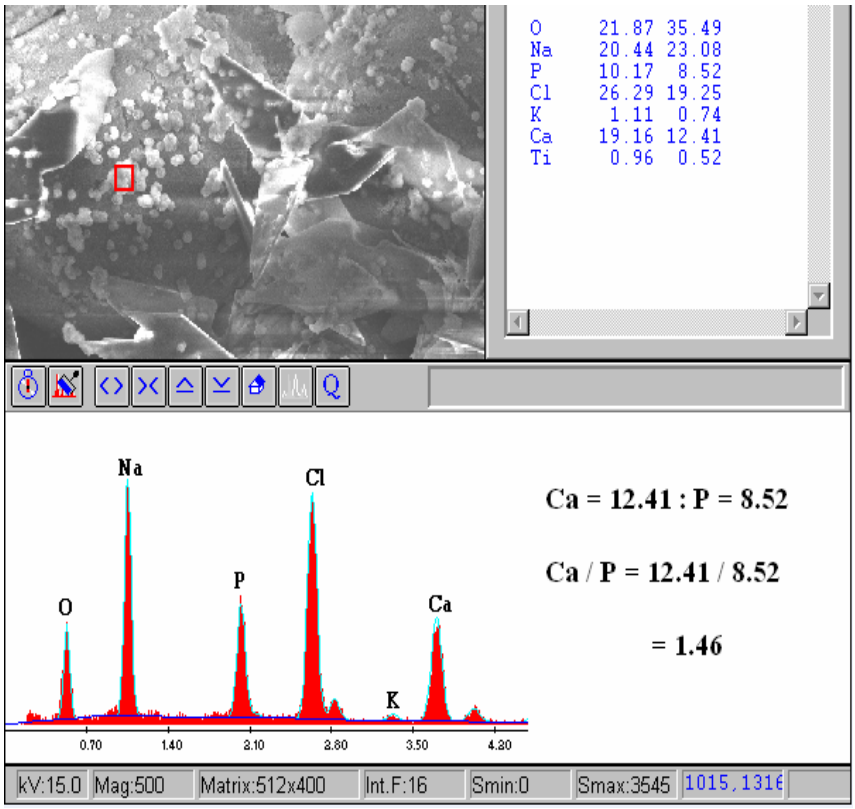

(a)

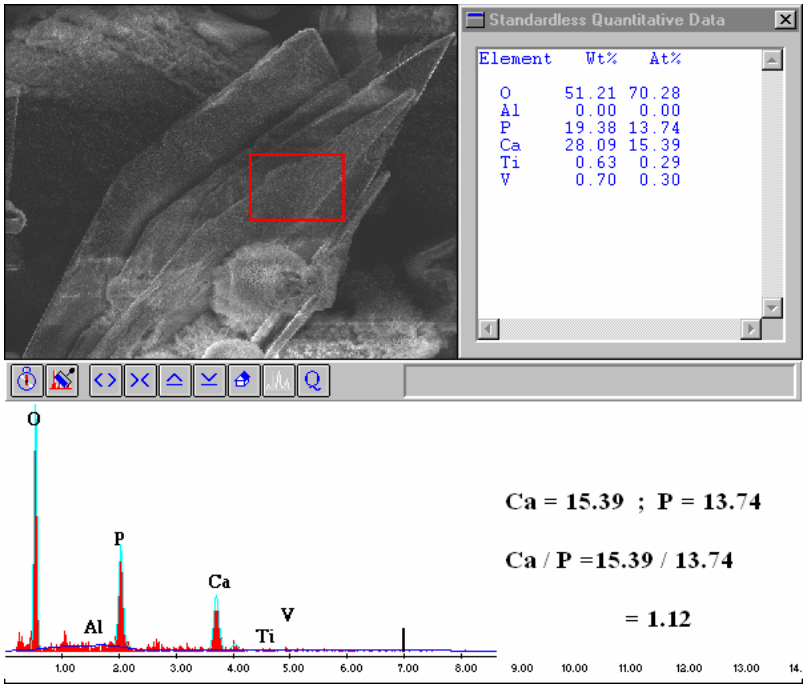

(b)

Figure 6.77. EDX analysis of an untreated compact after 6-hours soaking in 10xSBF (a) rosette type and (b) plate–like.

CHAPTER 7

DISCUSSION

7.1. Dip Coating Using HA Powders

Coatings prepared by the sol–gel can be either amorphous or crystalline, but they are stoichiometric and homogeneous. The synthesized sol-derived HA powder used in this study were found to be partially crystalline after drying at 90°C and were single-phase and crystalline until about 1200°C. Thermal treatment temperature following the coating should; however, be selected at a minimum level that still assures sufficient quality of HA film, in terms of crystallinity, film integrity, and adhesion to the substrate. Furthermore, the lower sintering temperatures also avoid α+β phase transition occurring at 883 and 960 °C in titanium and titanium alloy, respectively. This ensures the retention of the starting material microstructure; hence, allow controlling the microstructure. Based on the above facts, the sintering of compacts coated with sol-derived and commercial HA powders were performed at 840 °C (below α+β phase transition temperature) (Mavis and Tas 2000, Garrett et al. 2005).

SEM examinations of the sol-derived and unmilled and milled HA powder coated compact samples showed relatively uniform films over the entire surface of the sintered Ti6Al4V particles with a characteristic 'orange peel' texture (Figure 7.1 a)). The surfaces of Ti6Al4V particles soaked in sol-derived powder solution were found to be coated partially after 2-minute soaking; small regions on the particle surfaces remained to be uncoated and after 4-minute soaking the coating thicknesses of Ti6Al4V particles increased and originally open pores started to be filled with HA. It was also noted that the coating layer was porous. Although complete coating was achieved at 3-minute coating using sol-derived powder, the coating was complete after 1-minute soaking using commercial HA powder. The rate of coating difference between two powders may partly arise from the differences in powder concentration and particle size and size distribution between two powders. In sol-derived powder solution, the HA content was only half of that of commercial HA solution. The size of the commercial HA powder was also bigger than that of sol-derived powder. These may pronounce the possible effects of powder weight percentage and powder size in dip-coating on the

final coating layer deposition rate. It was also found that milling of commercial powder was influential in the thickness and homogeneity of the coating layer. Compared to the compacts coated with unmilled powder, the compacts coated with the milled HA powder solution showed a thinner coating layer at the sintering necks. The use of the milled powder resulted in smother coating surface, relatively thin coating layer and more homogenous HA coating particularly at particle sintering necks. In addition, less powder agglomeration was observed in the compacts coated with milled powder. This may pronounce the effect of particle size and size distribution effect on the quality of coating in dip-coating. However, further experimentations are needed to clarify precisely the effects of powder size and powder size distribution on the morphology and thicknesses of the coating layer.

In all dip-coated compacts, the coating started from the sintering necks and proceeded to the uncoated regions of the Ti6Al4V particles on the surface of the compact. Therefore, the coating was thicker at the particle sintering necks. In a previous study by Lu Gan et al. 2004 similar thicker coating layer at the particle sintering necks were observed in Ti particles coated on a surface of a Ti bulk implant (Figures 7.1.). The sinter necks have a concave geometry with the radius of curvature of the concavity being small. The thicker deposit in this region is believed to be due to capillary effects drawing the coating solution into this concave region. Cracks on the coating layer particularly at the sintering necks were observed in all dip-coated compact samples. The cracks on the coating layer in sol-derived powder was however more extensive than those of commercial HA powder coated samples. Since the optimum soaking time was 1-minute in commercial HA coated samples, the crack formation diminished as compared with compacts coated with sol-derived particle where the optimum soaking time was 3-minute and hence the coating layer is thicker. The coating layer cracking was believed to be a result of the greater residual stresses that developed within these thicker film regions. Future studies are therefore required to optimize the soaking-time as function of crack formation on the coating layer sol-derived powder coated samples.

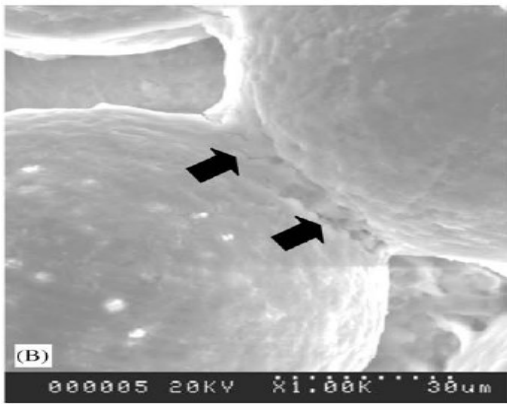

(a)

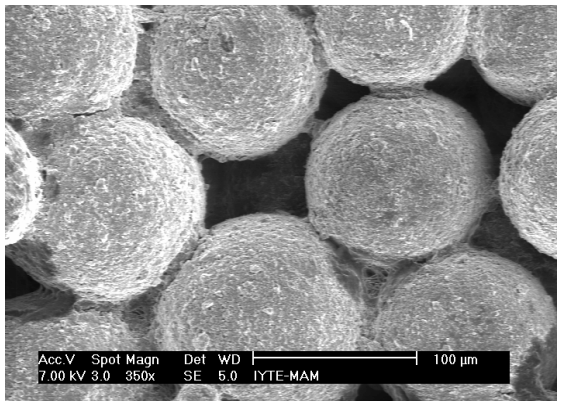

(a)

Figure 7.1. Scanning electron micrographs showing thicker coating layer at particle sintering necks (a) CaP coated Ti powder layer on the Ti implant coating (Source: Gan et al. 2003) and (b) HA coated Ti powder compacts (this study)

Nguyen et al. 2004 investigated in vivo behavior of a Ti implant with Ti powder layer on it. It was shown in the same study that the bone ingrowth occurred between the delaminated calcium phosphate layer and substrate (Figure 7.2.). The extent of bone ingrowth or fill within the sintering necks was increased by the presence of the calcium phosphate film. Therefore, the cracks and delaminations formed at the sintering necks do not prevent the bone ingrowth.

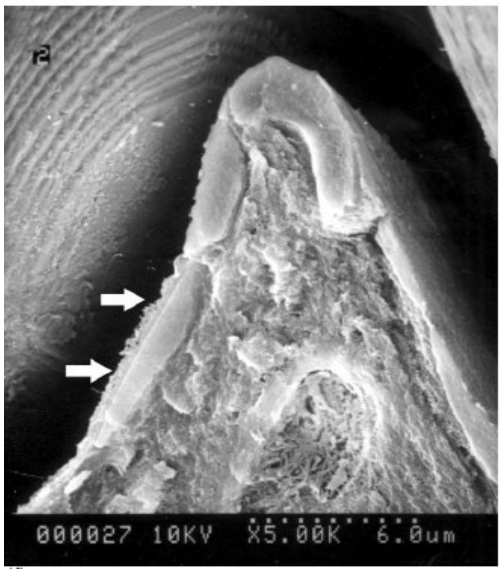

Figure 7.2. The bone formation at the sintering necks between delaminated CaP layer and Ti particle. (Source: Nguyen et al. 2004)

7.2. Biomimetic Coating

The biomimetic approach is one of the most promising techniques for producing calcium phosphate coatings. It utilizes supersaturated aqueous solutions with ionic composition similar to that of human plasma and allows coating complex-shaped materials (Xie et al. 2005, Kokubo 2005). NaOH heat treatment converts the sodium titanate hydrogel to amorphous sodium titanate which is stable and reduces the releasing rate of Na^+ ions from surface. It was also shown previously that alkali- and heat treated porous titanium formed more uniform apatite nucleation (Liang et al. 2003, Lenka et al.2004). When alkali and heat-treated samples were soaked in 1xSBF and in 5xSBF a dense and uniform layer of the bonelike apatite layer formed faster than untreated samples. This is because the sodium ion in the surface layer replaced the H_3O^+ ion in SBF, to produce Ti-OH groups on the surface of the metal, and the ionic activity product of the apatite in SBF. The Ti-OH group induced the apatite nucleation and the increased activity product accelerated the apatite nucleation. The apatite nuclei grew spontaneously by consuming the calcium and phosphate ions from SBF. The bond between the metal and calcium phosphate is of a chemical nature, which means that the adhesion is relatively good (Vanzillotta et al. 2005, Feng et al. 2000, Andrade et al. 1998). Alkaline and heat-treatment accelerated nucleation of CaP also increased the density of layer of the bonelike apatite in 10xSBF. But, the morphology of the CaP precipitates formed was found quite different in 10xSBF.

The CaP nucleation periods for alkali-heat treated and untreated samples in 1xSBF, 5xSBF and 1OxSBF solutions are tabulated Table7.1. Both SBF concentration and NaOH and heat treatment reduce the CaP nucleation time in the compacts. The concentration of SBF solution is however more effective than NaOH-treatment in reducing the nucleation time. The complete coating of the compacts using 1xSBF was 14 and 21 days for treated and untreated sample, respectively. While the complete coating was reduced to 24 and 36 hours in 5xSBF solution for treated and untreated compact samples respectively. The nucleation time was further reduced in 10xSBF: 6 hours soaking was enough to provide complete coating layer on the sample. These results also showed that complete coating occurred approximately at time 2 times of the nucleation time, which can be used as a guide in coating of porous implants.

Table 7.1. Effect of alkali-heat treatment on first nucleation time of 10xSBF solutions

	1xSBF	**5xSBF**	**10xSBF**
First nucleation time for untreated sample	10 days	16 hours	4 hours
First nucleation time for alkali-heat treated sample	7 days	7 hours	2 hours

The stable stock solution of pH values of 1xSBF, 5xSBF and 10 xs SBF were 7.4, 6.0 and 5.8 respectively. Ca/P ratio of the 1x SBF is more approximate to that of HA. Values of Ca/P ratio decrease with increasing concentration and decreasing pH of the soaking solution of solution. CaP formations in SBF were analyzed by Xiong Lu and Yang Leng based on the crystallization theories of thermodynamics and kinetics. They showed that HA precipitation exhibited a higher thermodynamic driving force than does octacalcium phosphate (OCP) and dicalcium phosphate dhiydrate (DCPD) in 1XSBF. Figures 7.3 (a) and (b) show free energy and change (ΔG) and nucleation rates (J) of Ca-P precipitation in SBF solution as function of pH, respectively. Figure 7.4(a) shows that OCP precipitation is thermodynamically favorable in 1XSBF solution after pH of 6. Note that there is no driving force for DCPD precipitation in 1XSBF because ΔG of DCPD is always greater than zero (Figure 7.3(a)). The HA and OCP nucleation rates are significantly affected by the pH values as seen in Figure 7.3 (b). Higher pH environment increases HA and OCD nucleation rates. Although DCPD is commonly believed to be a precursor to HA formation in aqueous solutions, DCPD precipitation has not been previously reported in 1XSBF. DCPD precipitation becomes possible when the concentrations of calcium and phosphate ions increase to a higher than normal level in SBF. In addition to, it is known that an amorphous calcium phosphate (ACP) precursor is always present during the precipitation of apatitic calcium from the highly supersaturated solutions, such as 10xSBF.

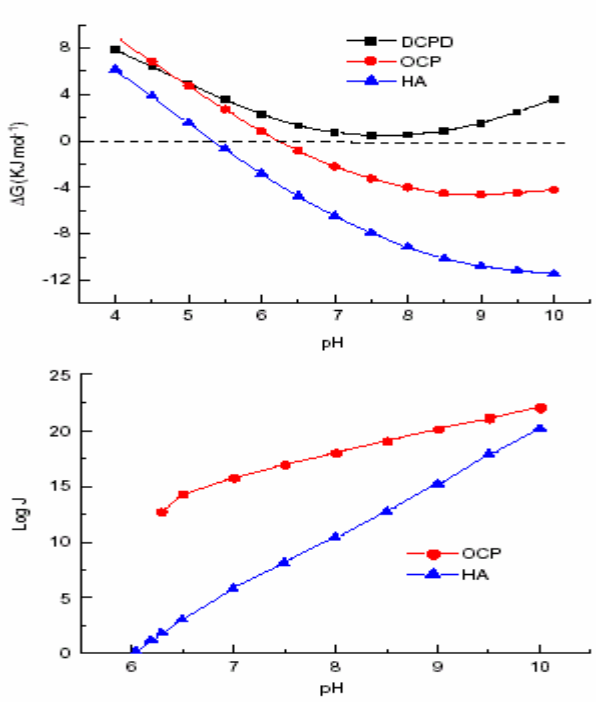

Figure 7.3. (a) Free energy change (ΔG) of Ca-P precipitation in SBF as a function of pH value and (b) nucleation rates (J) of HA and OCP precipitation in SBF. (Source: Lu and Leng 2004)

After 6 hours soaking in 10xSBF, rosette type and plate like precipitates were observed on the surfaces of the coated powder compacts. These plate-like precipitates is believed to be DCPD precipitates, resulting from the higher concentrations of Ca and P in SBF solution. EDX measurements on the precipitates have shown the Ca/P ratios of 1.12 and 1.46 for plate like and rosette type precipitates. Ca/P ratio of the plate like precipitates are slightly greater than the theoretical value for DCPD (Ca/P = 1.0). This may be due to the due to small HA precipitate associated with DCPD precipitates. (Rigoa et al. 2004)

It was also found that drying of the coated powders compacts at an elevated temperature formed smooth coating surfaces. However, extensive cracking was observed in these samples, partly because of the removal of water and partly because of the differences between the thermal expansion coefficients of CaP coating and Ti substrate. Nevertheless, the gradual drying at elevated temperature may be used to form uniform coating layer in coated compact samples. Future studies will therefore concentrate on the gradual drying of the coated samples in order to tailor the coating layer through a low temperature heat treatment drying procedure.

7.3. The Effect of Coating on The Porous Ti Implants

A period of non-functional loading for three to four months normally is recommended for patients receiving porous-coated joint replacement implants. Similarly, assuming good patient health and well-being recommended post-implantation patient rehabilitation with porous-surfaced dental implants an 8-week period or so prior to normal functional loading (Pilliar 1991). The minimum relative movement between the implant and host bone during healing is a necessary requirement for successful osseointegration. Not only orthopedic implants but also dental implants, because of acting of muscle forces at the implantation site and accidental unintended loading ,total avoidance of loading is not possible. When loading by reason of relative movements greater than a critical level of 50 μm or so (Karachalios et al. 2004), will prevent bone formation and ingrowth. Because of these reasons, the use of porous implant structures become very important in hard tissue replacements. Gan et al. 2005 have shown that CaP films formed over sintered porous-surfaced Ti6Al4V implants significantly increased the rate of bone ingrowth and implant fixation at early post-implantation periods (at 6 and 9 days) compared with non-CaP-coated, porous-surfaced Ti6Al4V implants. Bone growth into such small cusp-like regions appeared to be inhibited, at least at 2 weeks after implant placement, so that a very small region devoid of bone often resulted.

CHAPTER 8

CONCLUSIONS

In this study, two methods of CaP coating, dip coating and biomimetic, on porous Ti6Al4V powder compacts were experimentally investigated. The powder compacts produced by sintering of compacted green powders contained 37% open porosity with an average pore size of 63 micrometers. Three different dip coating solutions were used in dip-coating experiments: using sol derived and unmilled and milled commercial HA powder solutions. The compacts were also coated by inserting into 1xSBF, 5xSBF and 10xSBF solutions. The effects of alkali and heat treatment on the coating rate and thickness were also determined. The following are concluded :

1. The porous Ti6Al4V powder compacts were sucessfully coated using HA dip coating solutions. The optimum soaking times were 3 and 1-minute for sol-derived and commercial HA powders of milled and unmilled, respectively. Increasing soaking times further filled originally open pores. The rate of coating difference between two powders may partly arise from the differences in powder concentration and particle size and size distribution between two powders.

2. The coating in dip-coated compact samples started from the particle sintering necks. The thicker deposit in this region is believed to be due to capillary effects drawing the coating solution into this concave region.

3. Cracks on the coating layer particularly at the sintering necks were observed in all dip-coated compact samples. The cracks on the coating layer in sol-derived powder was however more extensive than those of commercial HA powder coated samples. The coating layer cracking was believed to be a result of the greater residual stresses that developed within these thicker film regions.

4. Milling of HA powder induced more homogenous coating layer on the Ti6Al4V particles.

5. Increasing Ca and P concentrations in SBF increased the rate of CaP nucleation. Alkaline and heat-treatment further accelerated CaP formation.

6. The complete coating of treated and untreated compacts was 14 and 21 days using 1xSBF, 24 and 36 hours using 5xSBF and 4 and 6 hours using 10xSBF, respectively.

7. Although needle-like precipitates formed in the compacts soaked in 1 and 5xSBF, rosette type and plate like precipitates were observed on the surfaces of the powder compacts soaked in 10xSBF. This has been explained by the increased concentrations of Ca and P in 10xSBF resulting in the formation of DCPD precipitates.

REFERENCES

Andrade M.C.,. Filgueiras M.R.T., Ogasawara1T.,1999. "Nucleation and growth of hydroxyapatite on titanium pretreated in NaOH solution: Experiments and thermodynamic explanation" John Willey Vol.46, pp. 441-446.

Barrerea F., Blitterswijka C.A., Groota K., Layrolle P., 2002. "Influence of ionic strength and carbonate on the Ca-P coating formation from SBFX5 solution" Biomaterials Vol.23, pp. 1921–1930.

Barrerea F., Snelc M.M.E., Blitterswijka C. A., Groota K., Layrollea P., 2004. " Nano-scale study of the nucleation and growth of calcium phosphate coating on titanium implants" Biomaterials Vol.25, pp. 2901–2910.

Bharati S., Sınka M. K., Basu D., 2005. "Hydroxyapatite coating by biomimetic method on titanium alloy using concentrated SBF" Bull. Mater. Sci., Vol. 28, pp. 617–621.

Bigi A., Boanini E., Bracci B., FacchiniA., PanzavoltaS., Segatti F., Sturba L., 2005. "Technical note: Nanocrystalline hydroxyapatite coatings on titanium:a new fast biomimetic method" Biomaterials Vol. 26, pp. 4085–4089.

Bigi A., Boanini E., Rubini K., 2004. "Hydroxyapatite gels and nanocrystals prepared through a sol–gel process" Journal of Solid State Chemistry Vol.177, pp. 3092–3098.

Brinker C.J., Hurd A.J.,1994. Fundamentals of sol-gel dip coating" J. Phys.France Vol.4, pp.1231-1242.

Chou Y., Chiou W., Xu Y., Dunn J.C.Y. , Wu B. M., 2004. "The effect of pH on the structural evolution of accelerated biomimetic apatite" Biomaterials Vol. 25, pp. 5323–5331.

David H.,1998. "Metals in medical applications" KohnCurrent Opinion in Solid State & Materials Science Vol.3, pp. 309-316.

Feng Q.L., Cui F.Z., Wang H., Kim T.N. , Kim J.O.,2000. "Influence of solution conditions on deposition of calcium phosphate on titanium by NaOH-treatment" Journal of Crystal Growth Vol.210, pp. 735-740.

Gan L., Pilliar R., 2004. "Calcium phosphate sol–gel-derived thin films on porous-surfaced implants for enhanced osteoconductivity. Part I: Synthesis and characterization" Biomaterials Vol.25, pp. 5303–5312.

Gan L., , Wanga J., Pilliar R.M.,2005. "Evaluating interface strength of calcium phosphate sol–gel-derived thin films to Ti6Al4V substrate" Biomaterials Vol.26, pp. 189–196.

Garrett R., A. Pandit, D.P. Apatsidis, 2006 “Review:Fabrication methods of porous metals for use in orthopaedic applications” Biomaterials Vol. 27, pp. 2651–2670.

Gerber T.H., Holzhuter G., Knoblich B.,2000.“Development of Bioactive Sol-Gel Material Template for In Vitro and In Vivo Synthesis of Bone Material” Journal of Sol-Gel Science and Technology Vol.19, pp. 441–445.

Gross K. A., Chai C. S. , Kannangara G. S. K., Nissan B.,1998. “Thin hydroxyapatite coatings via sol-gel synthesis” Materials in Medicine Vol. 9, pp. 839-843.

Guden M.,T, Celik E., Akar E., Cetiner S., 2005. “Compression testing of a sintered Ti6Al4V powder compact for biomedical applications” Materials Characterization Vol.54, pp. 399– 408.

Habibovic P., Lia J., Valk C.M., Meijerc G., Layrolled P.,Blitterswijk C.A., Groot K., 2005. “Biological performance of uncoated and octacalcium phosphate-coated Ti6Al4V” Biomaterials Vol.26, pp.23–36.

Haddow D.B., James P.F., 1998. “Sol-Gel Derived Calcium Phosphate Coatings for Biomedical Applications” Journal of Sol-Gel Science and Techn. Vol. 13, pp. 261–265.

Hsieh M., Perng L.H., Chin T.S.,2002. Hydroxyapatite coating on Ti6Al4V alloy using a sol–gel derived precursor” Materials Chemistry and Physics Vol.74, pp. 245–250.

Hijón N., Cabanas M. V., Barba I. I., García M. A.,Regí M. V.,2001. “ Nanocrystalline bioactive apatite coatings” The Journal of Arthroplasty Vol. 19, pp.458-469

Hukovic M. M., Tkalcec E., Kwokal A., Piljaca J., 2003. “An in vitro study of Ti and Ti-alloys coated with sol–gel derived hydroxyapatite coatings” Surface and Coatings Technology Vol.165, pp. 40–50.

Jillavenkatesa A., Condrate R. A.,1998. “Sol-gel processing of hydroxyapatite” Journal of Materials Science Vol.33, pp. 4111-4119.

Jones F.H., 2001“ Teeth and bones: applications of surface science to dental materials and related biomaterials” The Eastman Dental Institute for Oral Health Care Science.

Karageorgiou V., Kaplan D., 2005. “Review: Porosity of 3D biomaterial scaffolds and osteogenesis” Biomaterials Vol.26, pp. 5474–5491.

Kim H., Koh Y., Li L., Lee S., Kim H., 2004. “Hydroxyapatite coating on titanium substrate with titania buffer layer processed by sol–gel method”, Biomaterials intro Vol.25, pp. 2533–2538.

Karachalios T., Tsatsaronis C., Efraimis G., Papadelis P., Lyritis G., Diakoumopoulos G., 2004. "The Long-Term Clinical Relevance of Calcar Atrophy Caused by Stress Shielding in Total Hip Arthroplasty A 10-Year, Prospective, Randomized Study"

Kokubo T.,2005. "Design of bioactive bone substitutes based on biomineralization process" Materials Science and Engineering Vol. 25, pp. 97– 104.

Kokubo T., Takadama H., 2006. "Leading Opinion: How useful is SBF in predicting in vivo bone bioactivity?"Biomaterials Vol.27, pp. 2907–2915.

Lenka J., Mullera F. A., Helebrantb A., Strnadc J., Greila P., 2004. "Biomimetic apatite formation on chemically treated titanium" Biomaterials Vol.25, pp. 1187–1194.

Liang F., Zhou L. , Wang K.,2003. "Apatite formation on porous titanium by alkali and heat-treatment" Surface and Coatings Technology Vol.165, pp. 133–139.

Liu D.M., Troczynski T.,Hakimi D., 2002. "Effect of hydrolysis on the phase evolution of water-based sol-gel hydroxyapatite and its application to bioactive coatings" Materials in Medicine Vol.13, pp. 657-665

Lopatin C.M., Pizziconi V.B., Alford T.L., 2001. "Crystallization kinetics of sol-gel derived hydroxyapatite thin films" Materials in Medicine Vol.12, pp.767-773.

Lu X., Leng Y., 2004. "TEM study of calcium phosphate precipitation on bioactive titanium surfaces" Biomaterials Vol.25, pp.1779–1786.

Lu X., Leng Y.,2005. "Theoretical analysis of calcium phosphate precipitation in simulated body fluid" Biomaterials Vol. 26, pp. 1097–1108.

Mavis B., Tas A.C., 2000. "Dip coating of calcium hydroxyapatite on Ti6Al4V substrates" J. Am. Ceram. Soc. Vol.83, pp.989-991.

Murugan R., Ramakrishna S.,2005. "Review:Development of nanocomposites for bone grafting" Composites Science and Technology Vol.65, pp. 2385–2406.

Nguyen H.Q., Deporter D.A., Pilliar R.M., Valiquette N., Yakubovich R.,2004. "The effect of sol–gel-formed calcium phosphate coatings on bone ingrowth and osteoconductivity of porous-surfaced Ti alloy implants" Biomaterials Vol. 25, pp. 865–876.

Ratner, B. D.,2004. " Biomaterials science :an introduction to materials in medicine" Elsevier Academic Press pp.8-158.

Rho J.Y., Spearing L. K., Zioupos P., 1998. "Mechanical properties and the hierarchical structure of bone" Medical Engineering & Physics Vol.20, pp. 92–102.

Rigoa E.C.S., Boschia A.O., Yoshimotob M., Allegrini S., Konig B., Carbonaric M.J.,2004 "Evaluation in vitro and in vivo of biomimetic hydroxyapatite coated on titanium dental implants" Materials Science and Engineering Vol. 24, pp. 647–651.

Schreurs B.W., Huiskes R.,Buma P.,Slooff T.J.J.H., 1996. "Biomechanical and histological evaluation of a hydroxyapatite-coated titanium femoral stem fixed with an intramedullary morsellized bone grafting technique: an animal experiment on goats" Biomaterials Vol.17, pp.1177-1186.

Suchanek W., Yoshimura M., 2002. "Processing and properties of hydroxyapatite-based biomaterials for use as hard tissue replacement implants" J. Mater. Res., Vol. 13, pp.751-762.

Tas A.C., Korkusuz F., Timuçin M., Akkaş N., 1997. "An investigation of the chemical synthesis and high-temperature sintering behaviour of calcium hydroxyapatite (HA) and tricalcium phosphate (TCP) bioceramics" Materials in Medicine Vol. 8, pp. 91-96.

Tas A.C., Bhaduri S. B., 2004. "Rapid coating of Ti6Al4V at room temperature with a calcium phosphate solution similar to 10× simulated body fluid" J. Mater. Res., Vol. 19, pp.2742-2749.

Vanzillotta P. S., Sader M. S., Bastos I. N., Soares G.A., 2005. "Improvement of in vitro titanium bioactivity by three different surface treatments" Dental Materials Vol.14, pp. 1-8.

Wei M., Kim H. M., Kokubo T., Evans J.H., 2002. "Optimising the bioactivity of alkaline-treated titanium alloy" Materials Science and Engineering Vol.20, pp. 125–134.

Weng W., Baptista J.L., 1997. "A new synthesis of hydroxyapatite" Journal of the European Ceramic Society Vol. 17, pp. 1151-1156.

Weng W., 1998. "Sol-gel derived porous hydroxyapatite coatings" Materials in Medicine Vol.9, pp. 159-163.

Williams D. F., 2003. "Biomaterials and tissue engineering in reconstructive surgery" Sadhana Vol. 28, pp. 563–574.

Xiao X. F.,b, Liu R. F., , Zheng Y. Z., 2005. "Hydoxyapatite/titanium composite coating prepared by hydrothermal–electrochemical technique" Materials Letters Vol.59, pp. 1660–1664.

Xie Y., Liu X., Chu P.K. , Ding C.,2005. "Nucleation and growth of calcium–phosphate on Ca-implanted titanium surface" Surface Science Vol.14, pp.1-6.